

Univ.Prof. Dr. Friedrich Aumayr



TECHNISCHE
UNIVERSITÄT
WIEN

DIPLOMARBEIT

Nanostructuring of surfaces by swift heavy ion impacts under grazing incidence

ausgeführt am
Institut für Angewandte Physik
der Technischen Universität Wien
Wiedner Hauptstraße 8-10 / 134
1040 Wien

unter Anleitung von
Univ.Prof. Dr. Friedrich Aumayr

und

Dipl.-Ing. Elisabeth Gruber

durch

Lorenz Bergen BSc.
Matrikelnummer 1027623
Lobmeyrgasse 7/27
1160 Wien

Wien, 10. Mai 2016

Lorenz Bergen

Abstract

The irradiation of solid targets with swift heavy ions can induce a permanent modification of the surface and bulk structure in the nanoscale range. At sufficiently high impact energy each single ion produces a straight track in the bulk of some μm with hillocks or nanosized craters at the impact point.

In contrast to many other studies where targets have been irradiated under normal incidence, our samples were irradiated under glancing angles between 0.2° and 2° with respect to the surface plane. The irradiations have been performed at the IRRSUD beamline at GANIL (Caen, France) with lead and xenon ions at kinetic energies between 23 MeV and 100 MeV.

High resolution atomic force microscopy in topographic tapping mode has been used for a comparative study of track formation on various surfaces (SrTiO_3 , TiO_2 , CaF_2 and mica). Images of the different targets show a strong material dependent nanostructure creation. While on SrTiO_3 and TiO_2 the previously reported chains of hillocks are identified, CaF_2 and mica surprisingly show a different type of surface modification, namely the creation of a double track, consisting of single hillocks, which later joins to a single track. In between of the two chains a groove like structure is observable.

The focus of this work was to investigate the behaviour of the track structure, especially of the double tracks in dependence of irradiation parameters. Therefore systematic studies at different incidence angles have been performed. Further the dependence on the target temperature has been evaluated by heating CaF_2 and mica targets to 400°C during irradiation. To investigate the link between energy loss and the induced nanostructure formation mica samples have been irradiated with ions at five different kinetic energies between 23 MeV and 100 MeV to find a threshold for nanostructure creation under grazing incidence.

Kurzfassung

Die Bestrahlung von Festkörpern mit schnellen Ionen kann zu einer dauerhaften Modifizierung der Oberflächen und der darunterliegenden Schichten im nanoskaligen Bereich führen. Bei genügend hoher kinetischer Energie erzeugt jedes einzelne Ion eine gerade, bis zu einige μm lange Spur im Volumen des Targetmaterials mit Erhebungen oder Vertiefungen von einigen Nanometern an der Aufprallstelle.

Im Gegensatz zu vielen anderen Studien in denen die Bestrahlung normal auf die Probenoberfläche durchgeführt wurde, wurden unsere Proben unter streifenden Einfall zwischen $0,2^\circ$ und 2° relativ zur Oberflächenebene bestrahlt. Die Bestrahlungen fanden an der IRRSUD Anlage in GANIL (Caen, Frankreich) mit Blei- und Xenon-Ionen bei kinetischen Energien zwischen 23 MeV und 100 MeV statt.

Hochauflösende Rasterkraftmikroskopie wurde im Tapping-Mode betrieben, um die Topographie der Nanostrukturbildung auf verschiedenen Oberflächen (SrTiO_3 , TiO_2 , CaF_2 und Mica/Glimmer) zu vergleichen. Aufnahmen mit dem Mikroskop der verschiedenen Proben zeigen dabei eine starke Materialabhängigkeit. Während auf SrTiO_3 und TiO_2 die bereits früher beobachteten Hillock-Ketten identifiziert wurden, zeigen CaF_2 und Glimmer überraschenderweise eine andere Art der Oberflächenmodifizierung, nämlich die Ausbildung einer Doppelspur bestehend aus einzelnen Hügelchen die schließlich in eine einzelne Spur übergeht. Zwischen den beiden Ketten ist eine grabenartige Vertiefung ausgebildet.

Das Hauptaugenmerk dieser Arbeit war es, den Einfluss der Bestrahlungsparameter auf die Nanostrukturierungen, insbesondere auf die Doppelspuren, zu untersuchen. Dabei wurden systematische Messungen bei verschiedenen Einfallswinkeln vorgenommen. Weiters konnte die Abhängigkeit von der Oberflächentemperatur untersucht werden, indem CaF_2 und Glimmerproben während der Bestrahlung auf 400°C geheizt wurden. Um den Einfluss des Energieverlusts auf die Ionen-induzierten Nanostrukturen zu untersuchen, wurden Glimmerproben mit Ionen fünf unterschiedlicher kinetischer Energien zwischen 23 MeV und 100 MeV bestrahlt, um einen Schwellwert für die Nanostrukturierung unter streifendem Einfall zu finden.

Contents

List of abbreviations	vii
Physical constants	vii
1 Introduction	1
1.1 Motivation	1
1.2 Ion beams	3
1.3 Track creation models for swift heavy ion irradiation	3
1.3.1 Coulomb explosion model	3
1.3.2 Thermal spike model	5
1.4 Energy loss of ions in solids	6
1.4.1 Nuclear stopping	7
1.4.2 Electronic stopping	8
1.4.3 Radiative stopping	9
1.4.4 Channelling	10
1.4.5 Total energy loss	11
1.5 Nanostructuring of surfaces - state of the art	12
1.5.1 SrTiO ₃	12
1.5.2 TiO ₂	13
1.5.3 CaF ₂	14
1.5.4 Mica	15
2 Materials and methods	17
2.1 Irradiations at the IRRSUD beam line	17
2.2 Atomic force microscopy	18
2.2.1 Working principle	19
2.2.2 Imaging modes	20
2.3 Investigated materials	21
2.3.1 Strontium titanate SrTiO ₃	21
2.3.2 Titanium oxide TiO ₂	22
2.3.3 Calcium fluoride CaF ₂	23
2.3.4 Mica	25
2.4 Energy loss calculations	26

3	Experimental results and discussion	29
3.1	Experimental results I - SrTiO ₃ and TiO ₂	29
3.1.1	SrTiO ₃	29
3.1.2	SrTiO ₃ - Topography	29
3.1.3	SrTiO ₃ - Analysis of the nanostructure	30
3.1.4	TiO ₂	36
3.1.5	TiO ₂ - Topography	36
3.1.6	TiO ₂ - Analysis of the nanostructure	37
3.1.7	Discussion	40
3.2	Experimental results II - CaF ₂ and mica	41
3.2.1	CaF ₂	41
3.2.2	CaF ₂ - Topography	41
3.2.3	CaF ₂ - Analysis of the nanostructure	42
3.2.4	Mica	46
3.2.5	Mica - Topography	47
3.2.6	Mica - Analysis of the nanostructure	49
3.2.7	Discussion	70
4	Summary and outlook	73
4.1	Summary	73
4.2	Outlook	74
	A Irradiation Data	77
	List of Figures	82
	List of Tables	83
	Bibliography	85
	Danksagung	97

List of abbreviations

AFM	atomic force microscope
CaF₂	Calcium fluoride
DC	direct current
HCI	highly charged ion
HOPG	highly ordered pyrolytic graphite
IAP	Institute of Applied Physics
mica-OH	mica with a sum formula $KAl_2[AlSi_3O_{10}(OH)_2]$
mica-F	mica with a sum formula $KMg_3[AlSi_3O_{10}]F_2$
RMS	root mean square
SiC	Silicon carbide
SHI	swift heavy ion
SrTiO₃	Strontium titanate
TiO₂	Titanium oxide

Physical constants

$k_B = 1.3806504 \cdot 10^{-23} \text{ J/K}$	Boltzmann constant
$c = 299792458 \text{ m/s}$	vacuum velocity of light
$e = 1.60217687 \cdot 10^{-19} \text{ C}$	elementary charge
$\alpha_f = 7.2973525376$	fine structure constant
$m_e = 9.10938215 \cdot 10^{-31} \text{ kg}$	electron mass

1 Introduction

1.1 Motivation

The interaction of ions with solid targets has become an attractive field of research in the last decades, especially because of the high technological relevance behind the fundamental mechanisms [1–5]. A large number of analytical techniques has been developed out of these investigations e.g. secondary ion mass spectroscopy (SIMS), low-energy ion scattering spectroscopy (LEIS) and Rutherford backscattering spectroscopy (RBS) [6–12]. Different methods require ions at various energies inducing different physical effects.

In addition ion beams are an effective tool for surface lithography [13–19]. Swift heavy ions (SHI), characterised by deposition of high kinetic energy, and highly charged ions (HCI), characterised by deposition of high potential energy, are used. Due to their high kinetic energy SHI irradiation can lead to a permanent modification of the surface and in the bulk of a solid target. Hereby a latent track of structural modified material is formed by each single ion [1, 13]. Earlier studies have been performed with SHI. Since the development of sources for HCI, this kind of ions has been used for nanostructuring as well [13, 20, 21]. Surprisingly both projectiles induce similar types of surface nanostructures despite the different underlying physical mechanism [13].

One research field of the Atomic and Plasma Physics Group at IAP is the investigation of nanostructure formation on surfaces due to ion irradiation. In the past years the work main focussed on studies with highly charged ions (HCI), see e.g. [16, 22–24]. In the framework of the "SIISU" project, an FWF collaboration between Austria and France, nanostructures induced by highly charged ions (HCI) should be compared with the ones induced by swift heavy ions (SHI). In this thesis studies with swift heavy ions are presented.

The SHI irradiations have been performed at GANIL under grazing incidence. Under this particular geometry the track is formed close to the surface and partially visible as a surface modification e.g. as a groove or as a chain of nanodots, and comparable to the shallow damage of HCI.

The presented work gives a comparison between the SHI irradiation of different ma-

terials, ranging from well investigated oxides like SrTiO_3 and TiO_2 to materials like CaF_2 and mica where systematic studies under grazing angle incidence are still missing.

In the first part part of this thesis ([Chapter 1.2 – 1.5](#)) the theoretical background of ion - solid interaction with the focus on swift heavy ions is given.

[Chapter 2](#) gives an overview on the irradiation of the samples ([Chapter 2.1](#)) and a brief introduction into the used microscopy techniques ([Chapter 2.2](#)). The investigated materials and their preparation are described in [Chapter 2.3](#). Finally energy loss calculations are performed in [Chapter 2.4](#).

[Chapter 3](#) presents the results of atomic force microscopy imaging of samples irradiated by SHI, i.e. the main results of this thesis and their discussion.

Finally a summary of the work is given in [Chapter 4.1](#).

Major parts of this thesis have already been presented in poster contributions at international conferences:

1. 9th International Symposium of Swift Heavy Ions in Matter (SHIM 2015), Darmstadtium, Darmstadt/Germany; 18.05.2015.
2. 29th International Conference on Photonic, Electronic and Atomic Collisions (XXIX ICPEAC), Toledo/Spain; 23.07.2015.

A corresponding first manuscript is currently being prepared for publication:

3. Elisabeth Gruber, Pierre Salou, **Lorenz Bergen**, Mourad El Kharrazi, Elie Lattouf, Clara Grygiel, Yuyu Wang, Abdenacer Benyagoub, Delphine Levavasseur, Jimmy Rangama, Henning Lebius, Brigitte Ban-d'Etat, Marika Schlegelberger, Friedrich Aumayr

A complex form of ion-tracks observed on CaF_2 after grazing incident swift heavy ion irradiation

submitted to *New Journal of Physics*

1.2 Ion beams

For the first time ion beams have been investigated by Goldstein in 1886 [25] after discovering the so called anode rays. Wien [26] analysed in 1897 the value of the charge/mass ratio of these beams and showed that anode rays consist of positively charged particles of the filly gas inside the discharge tube.

From a historical point of view ionising tracks were first shown by Wilson [27, 28] in the early 1910s. The experiments have been performed in a cloud chamber, where injected α -particles lead to ionisation processes along their path thus forming a track of water droplets is visible in light due to Mie scattering.

It took decades until 1958 Young [29] was able to investigate tracks from fission fragments in a solid target material (radiation damaged lithium fluoride) after etching with a mixture of hydrofluoric and glacial acetic acid. He could show that each single fission fragment creates a track of defects in the bulk [29]. Only one year later Silk and Barnes observed individual tracks in mica with a diameter of less than 30 nm and up to 4 μm long, again induced by fission particles [30].

In the last decades systematic studies of nanostructuring have been performed with swift heavy ions (SHI) and (slow) highly charged ions (HCI). The second ones are characterised by a high potential energy that is calculated as the sum of all missing electrons binding energies (up to hundreds of keV) [31] and a low kinetic energy corresponding with a low velocity (slow means less than $2.18 \cdot 10^6$ m/s). The energy composition of swift heavy ions is dominated by the kinetic part. SHIs are created at accelerator facilities like GSI and GANIL, typical up to energies in the MeV and GeV range. Due to stripping processes used in their production their charge state usually depends on their velocity [32]. The magnitude of SHI induced nanostructures depends on the projectiles electronic loss [13].

1.3 Track creation models for swift heavy ion irradiation

A couple of models have been developed to describe the basic concepts of swift heavy ion track formation. Two of them are introduced in the next pages.

1.3.1 Coulomb explosion model

The coulomb explosion model has been proposed by Fleischer *et al.* [1] in 1965 as the "ion explosion spike mechanism". A charged particle is passing through the bulk

of the target material and the lattice atoms are ionised along the projectile path. The excited electrons gain enough energy to leave the excitation region [33], thus a cylinder filled with positively charged ions is formed [1]. The mutual repulsive forces between the ions eject them from their original place in the surrounding lattice, so that its periodic structure is damaged [33]. The motion of ions stops quickly after electric neutrality is restored [33], which happens in a time of 10^{-13} s - 10^{-14} s [34].

Four criteria must be fulfilled for track creation [1]:

- The local electronic stress σ_e must be larger than the local mechanical strength σ_m , this means that repulsive Coulomb forces in the ionised region of the target material must overcome the lattice binding force. The Coulomb force between two ions in a material with an average interatomic distance a_0 and dielectric constant ε with an average of n ionised electrons is given by

$$F_C = \frac{n^2 \cdot e^2}{\varepsilon \cdot a_0^2}. \quad (1.1)$$

The force by unit area is the electronic stress and can be calculated by

$$\sigma_e = \frac{F_C}{a_0^2} = \frac{n^2 \cdot e^2}{\varepsilon \cdot a_0^4}. \quad (1.2)$$

The mechanical tensile strength of a material with a Young's modulus E is given by

$$\sigma_m = \frac{1}{10} E, \quad (1.3)$$

so that out of $\sigma_e > \sigma_m$ follows that

$$\frac{n^2 e^2}{\varepsilon a_0^4} > \frac{1}{10} E \quad (1.4)$$

and further

$$n^2 > E \cdot \frac{\varepsilon a_0^4}{10 e^2}. \quad (1.5)$$

So track creation is more like in materials with a low mechanic strength and dielectric constant or a small interatomic distance.

- At least one ionisation is necessary per atom plane crossed by the projectile ion.
- The electron mobility near the ion's path must be so small that electrons, emitted in the ionisation events, cannot be replaced within a short time.

- The mobility of holes has to be low, otherwise permanent track creation is also suppressed. Thus, metals and some semiconductors should not show tracks.

Nanostructures have been observed in insulating materials, that were attributed to Coulomb explosion [35]. No attempt has been made to describe the observed tracks in metals by Coulomb explosion, because the large electron mobility in metals would be in strong contrast to the requirements listed above [36].

Although attempts to calculate the repulsive forces and the moving time of the ions have been performed for various materials e.g. metallic glass [37], actually no Coulomb explosion model is developed in a way to describe the experimental observations correctly [13].

1.3.2 Thermal spike model

Another concept to explain ion track formation is the thermal spike model, based on a two temperature model [34, 38–40] elaborated to describe the damage in all kind of materials, metals and insulators. The electronic system is rapidly heated by the electronic energy loss of the projectile ions to a temperature T_e in the range of the Fermi temperature [38]. This energy is then transferred via electron-phonon coupling to the lattice system from where the energy dissipate into the surrounding cold matrix. If the thermal spike reaches the melting temperature and the following cooling happens rapidly enough, tracks are created. The various processes take place on the following time scales [40]:

- 10^{-16} s: energy deposition
- 10^{-15} s: energy shared between the electrons
- 10^{-13} s: lattice thermalised.

Electronic excitation and motion of lattice atoms take place at sufficiently different time scales so that the two differential equations for energy diffusion in both sub-systems (electrons and phonons) are only coupled by the electron-phonon coupling constant g . Usually cylindrical symmetry can be assumed, so that the diffusion equations at time t and distance r can be written as [39]:

$$C_e(T_e) \frac{\partial T_e}{\partial t} = \nabla(K_e(T_e) \nabla T_e) - g \cdot (T_e - T_l) + A(r, t) \quad (1.6)$$

$$C_l(T_l) \frac{\partial T_l}{\partial t} = \nabla(K_l(T_l) \nabla T_l) + g \cdot (T_e - T_l) \quad (1.7)$$

where the subscript e connects a certain property with the electronic subsystem and l with the lattice subsystem:

∇	nabla operator in cylindrical coordinates
$C(T)$	specific heat
T	temperature
$K(T)$	thermal conductivity
$A(r, t)$	initial energy density supplied to the electrons
g	electron-phonon coupling

$$g = \frac{\pi^4 (k_B z n v_s)^2}{18 K_e (T_e)} \quad (1.8)$$

with material dependent parameters: v_s sound velocity, n atomic density and z the number of thermal spike electrons

The initial energy density is approximated by the Gaussian function

$$A(r, t) = b S_{elec}(E) \cdot \exp \left[- \frac{(t - t_0)^2}{2 t_0^2} \right] \cdot F(r), \quad (1.9)$$

with $t_0 = 10^{-15}$ s, $S_{elec}(E)$ the electronic stopping power of the projectile in that material at kinetic energy E , $F(r)$ the spatial distribution of delta energy deposition in the target material (described in [41]) and b the normalisation parameter, so that [39]

$$\int_{t=0}^{\infty} \int_{r=0}^{r_{max}} 2\pi r \cdot A(r, t) dt dr = S_{elec}(E). \quad (1.10)$$

For further discussion and influences of the parameters see e.g. [34, 39].

The thermal spike concept has been developed in the last years leading to various modifications of the diffusion equations (1.6) and (1.7) above, e.g. by introducing nuclear energy loss in addition [40] or taking the specific mass of the lattice ρ_l into account [42]. In the inelastic thermal spike model electrons are treated as a quasi free gas [40].

Nowadays the thermal spike model is the most accurate mechanism to describe SHI induced track creation with many applications e.g. calculation of track radii [42–45] and thresholds for track creation [14, 46].

1.4 Energy loss of ions in solids

The energy loss dE/dx of ions in matter can be divided into the nuclear, the electronic and the radiative energy loss. Depending on the projectiles energy different effects

are dominating. The stopping power $S(E)$ (actually a stopping force by dimension) of a target material for a certain kind of ions is defined by the negative energy loss

$$S(E) = -\frac{dE}{dx}. \quad (1.11)$$

The range of the ions in solid matter can be estimated by [47]

$$R = \int_0^{E_I} \left(\frac{dE}{dx}\right)^{-1} dE, \quad (1.12)$$

with E_I as the kinetic energy of the projectile ion.

1.4.1 Nuclear stopping

Nuclear stopping refers to elastic collisions between the projectile ions and the atoms of the targets material (these are the nuclei of the target therefore the term nuclear stopping), leading to a direct energy transfer to the target lattice. The energy transferred from an ion with the kinetic energy E_I to a resting atom is given by the following formula [48]

$$\Delta E_{nucl}(E_I, \theta) = E'_N = \frac{m_N \cdot v_N'^2}{2} = E_I - E'_I = \frac{4 \cdot m_I \cdot m_N}{(m_I + m_N)^2} \cdot E_I \cdot \sin^2\left(\frac{\theta}{2}\right) \quad (1.13)$$

where E'_N is the energy of the target atom and E'_I of the ion after collision. The ion mass is represented by m_I and the nuclei mass by m_N . θ represents the scattering angle in the center of mass system. The maximal energy amount is transferred for $\theta = \pi$ (central collision), given by

$$\Delta E_{nucl,max} = \frac{4 \cdot m_I \cdot m_N}{(m_I + m_N)^2} \cdot E_I. \quad (1.14)$$

The scattering angle θ is given by

$$\theta = \pi - 2b \int_{r_{min}}^{\infty} \frac{dr}{r^2 \left[1 - \frac{b^2}{r^2} - \frac{V(r)}{E_0}\right]^{1/2}} \quad (1.15)$$

with $E_0 = \frac{\mu \cdot v^2}{2}$, reduced mass μ , relative velocity v , ion-nucleus distance r with its minimum¹ r_{min} , collision parameter b and the interaction potential $V(r)$. $V(r)$ is the Coulomb potential multiplied with a screening function $\xi(r/a)$, which takes the reduced nucleus charge due to screening of the surrounding electrons into account. First approaches for the screening distance a have been performed by Bohr [32], later calculations e.g. by Firsov [50]. An often used screening function is the universal repulsive ZBL-potential, estimated by Ziegler, Biersack and Littmark from collections of experimental data [48]. Thus, $V(r)$ can be written as

$$V(r) = \frac{Z_I Z_N e^2}{4\pi\epsilon_0 r} \cdot \xi_{ZBL}(r/a) \quad (1.17)$$

with the screening parameter

$$a = \frac{0.8854 \cdot a_0}{Z_I^{0.23} + Z_N^{0.23}}, \quad (1.18)$$

the Bohr radius a_0 , the ion nuclear charge number Z_I , the nucleus charge of the target material Z_N and

$$\xi_{ZBL}(r/a) = 0.1818e^{-3.2r/a} + 0.5099e^{-0.9423r/a} + 0.2802e^{-0.4029r/a} + 0.0282e^{-0.2016r/a}. \quad (1.19)$$

Finally the nuclear stopping power can be determined by integration over different impact parameters b

$$S(E)_{nucl} = 2n\pi \int_0^\infty \Delta E_{nucl}(E_I, \theta) \cdot b \cdot db, \quad (1.20)$$

where n is the atomic density of the target material.

1.4.2 Electronic stopping

The electronic energy loss is induced by inelastic collisions of the projectile ion with the electrons in the target material and can be well described for quantum mechanic

¹ r_{min} can be calculated by setting the denominator of [equation \(1.15\)](#) equal 0, so that [49]

$$1 - \frac{b^2}{r_{min}^2} - \frac{V(r_{min})}{E_0} = 0 \quad (1.16)$$

relativistic particles by the Bethe-Bloch formula [47]:

$$-\left(\frac{dE}{dx}\right)_{elec} = \frac{Z_I^2 e^4 n_e}{4\pi\epsilon_0^2 \cdot v^2 m_e} \cdot \left[\ln \frac{2m_e v^2}{I \cdot (1 - \beta^2)} - \beta^2 \right] \quad (1.21)$$

with

Z_I	charge of the ion
e	elementary charge
n_e	electron density of the target
m_e	resting mass of the electron
v	velocity of the ion
β	v/c
c	velocity of light
I	average ionisation energy of the targets electron [51]: $I \approx (10 \text{ eV}) \cdot Z_T$ with Z_T the nuclear charge number of the target material.

Electronic energy loss causes effects like electronic excitations and ionisation of target atoms leading to electronic defects (like excitations) and the emission of electrons. Further corrections of the Bethe-Bloch formula include density effects [52] and shell corrections [53, 54]. The ion track induced due to electronic stopping can be estimated as a straight line, because of negligible relative momentum transfer from the much heavier ion to a single electron due to its high kinetic energy.

In [Figure 1.1](#) the electronic stopping power of ^{129}Xe ions in TiO_2 is plotted over the penetration depth, for an initial projectile energy of 100 GeV and 10 GeV. The highest energy loss occurs in a very small region before the ion is completely stopped, the so called Bragg-peak. The projected ion range is 30.44 mm @ 100 GeV, 0.807 mm @ 10 GeV and in the investigated energy range in that thesis (53 MeV) 5.85 μm . The SRIM code [55] has been used for these calculations.

1.4.3 Radiative stopping

This effect increases at still higher projectile kinetic energy (only a significant contribution in the relativistic energy regime) containing e.g. Cherenkov radiation [56] (velocity of projectile ion is larger than the speed of light in the target material) and bremsstrahlung [52] (emission of photons due to passing the coulomb field of a nucleus) with the following energy loss:

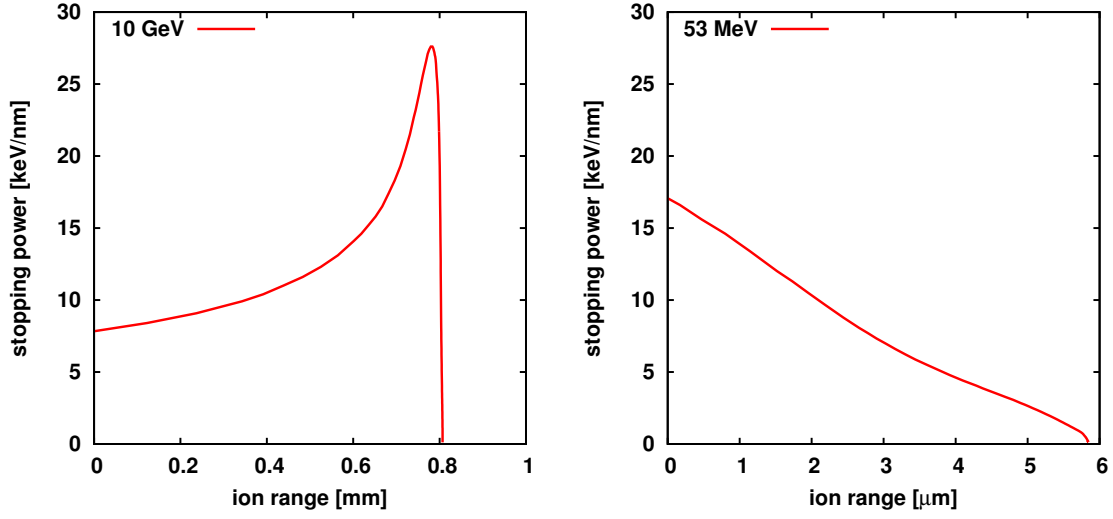


Figure 1.1: SRIM calculated energy loss curves of electronic stopping in dependence on the penetration depth, left for ^{129}Xe ions @ 10 GeV, right @ 53 MeV. Target material is TiO_2 .

- Cherenkov radiation [57]:

$$-\left(\frac{dE}{dx}\right)_{\text{cherenkov}} = \frac{(q_I e)^2}{c^2} \int_{\epsilon(\omega) > (1/\beta^2)} \omega \left(1 - \frac{1}{\beta^2 \epsilon(\omega)}\right) d\omega \quad (1.22)$$

with q_I charge state of the projectile, $\beta = v/c$ and a target dielectric constant $\epsilon(\omega)$.

- bremsstrahlung [52]:

$$-\left(\frac{dE}{dx}\right)_{\text{brems}} \propto Z_I^4 \cdot \gamma \quad (1.23)$$

with $\gamma = \sqrt{\frac{1}{1-v^2/c^2}}$, where v is again the ion velocity.

1.4.4 Channelling

One effect so far not discussed is channelling. Depending on the crystal orientation certain ion directions are possible, so that the projectile is guided between two planes of target atoms, interacting only with valence or conduction electrons [58]. Here repulsive forces between the ions and target atoms let the positively charged particle impose to stay between that two layers, in a channel of target atoms. In such a channel the stopping of ions is different (in general reduced), thus, the stopping power depends on the crystal orientation. Necessary conditions are small incidence

angles with respect to the crystal orientation as well as energetic ions [59].

Experimental investigations of that effect have been performed for e.g. polycrystalline aluminium, leading to increased ranges for channelled ions [60].

1.4.5 Total energy loss

Energy loss calculations for heavy projectiles using the SRIM code [55] show a maximum of electronic stopping at kinetic energies of typically hundreds of MeV with $S_{elec}(E)$ dominating at kinetic energies higher than 10 MeV (see Figure 1.2 and further calculations of energy loss curves in Chapter 2.4). Swift heavy ions are in the MeV to GeV regime, so that electronic stopping (ionisation processes and electronic excitations) is by far the dominating effect. After slowing down in the target material nuclear stopping takes over. Radiative stopping effects are negligible in the investigated ion energy range, so that

$$\left(\frac{dE}{dx}\right)_{tot} = \left(\frac{dE}{dx}\right)_{nucl} + \left(\frac{dE}{dx}\right)_{elec} \quad (1.24)$$

as well as

$$S(E)_{tot} = S(E)_{nucl} + S(E)_{elec}. \quad (1.25)$$

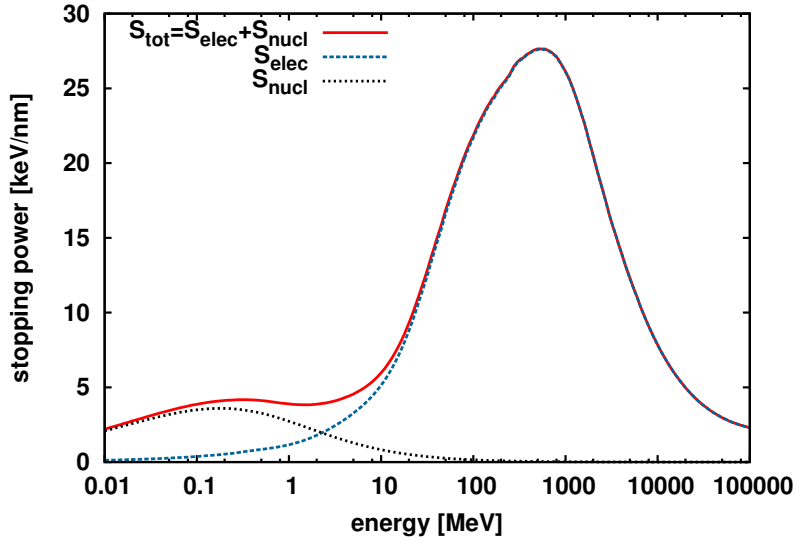


Figure 1.2: SRIM calculated energy loss curves of electronic stopping (red line) and nuclear stopping (blue line) of ^{129}Xe ions in TiO_2 .

Inside the bulk of the target electron capture and loss processes will lead to an equilibrium charge state of the projectile ion. The equilibrium charge state depends on the ion velocity v_I . All electrons with an orbital velocity smaller v_I are stripped

(“Bohr criterion”) and the equilibrium charge state is given by [61]

$$\langle q \rangle = \frac{v_I}{v_0} Z_I^{1/3} \quad (1.26)$$

with Z_I atomic number of the ion and $v_0 = c \cdot \alpha_f$ the Bohr velocity [62].

1.5 Nanostructuring of surfaces - state of the art

In the following an overview of previous studies on nanostructure creation of the irradiated materials is given.

1.5.1 SrTiO₃

In the last decade systematic investigations of SHI irradiation under grazing incidence have been performed. These investigations showed the creation of a chain of almost equidistant hillocks along the track at the surface with a total length of a few micrometers [15] (see Figure 1.3). The length l of the chain follows thereby the relation

$$l = d / \tan(\varphi), \quad (1.27)$$

motivated by geometrical considerations (see Figure 1.3), with the track length l , the irradiation angle φ and the maximum depth d from which the ion induced modification can still be detected. Akçöltekin *et al.* [15] concluded that d is constant and the lengths can be fitted by the function above (equation 1.27, see Figure 1.3). Thus, the length of the chain and the number of hillocks can be controlled by the incident angle.

The found relation between angle, length and depth of the ions tracks seems to have a general validity, as this behaviour has been observed also for other materials e.g. TiO₂ and Al₂O₃ with different values of d ($d_{TiO_2} = 7.3$ nm and $d_{Al_2O_3} = 5.3$ nm [63]). Even a conducting material like HOPG (highly oriented pyrolytic graphite) shows this behaviour, however, with a much shorter d (energy dependent) between 3.1 nm and 3.8 nm [64].

The dependence of the track length on the crystalline structure (respectively surface orientation) has been investigated by the same group [65]. SrTiO₃ (100) and SrTiO₃ (111) samples have been irradiated with 96 MeV Xe ions. Comparing the chain lengths in both cases shows, that at very small angles of less than 0.3° lengths in SrTiO₃ (111) are shorter than SrTiO₃ (100). The distance of two neighboured hillocks depends on the electronic structure of the crystal. So the angle [63] and the projectile

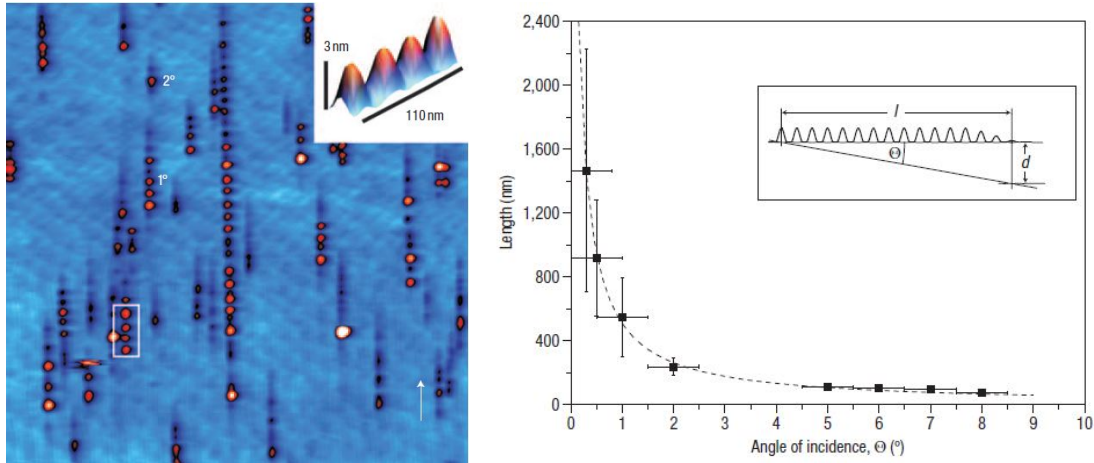


Figure 1.3: left: AFM image of SrTiO₃ after SHI irradiation. right: The length of SrTiO₃ chains is plotted over the angle of incidence compared with the $9.8/\tan(\varphi)$ fit (dashed line). Both images taken from [15].

direction in relation to the crystal orientation influences this property in magnitude and regularity [65]. Typical values are a few tens of nano meter [63].

Under glancing incident angles the height of the tallest nanodots of the chain is ~ 4 nm and the average one $3 \text{ nm} \pm 1 \text{ nm}$ for irradiation with ≈ 100 MeV ions [66]. This is in good agreement with perpendicular irradiation, which show a hillock height of typical $4 \text{ nm} \pm 1 \text{ nm}$ [66]. The height of the nanodots seems to increase with increasing stopping power and a threshold for surface nanostructure creation under grazing incidence could be estimated between 5.3 keV/nm and 7.2 keV/nm [46]. For normal incidence the threshold was found to be 7.3 keV/nm [46].

1.5.2 TiO₂

Besides SrTiO₃ grazing angle irradiation has been performed for the oxide TiO₂. Also for this material a chain of single nanodots is created on the surface [63]. Both, height and length of the single hillocks of TiO₂ have similar values of those created on SrTiO₃ [63]. The length of the chain follow the $l = d/\tan(\varphi)$ relation with a depth $d = 7.3 \text{ nm}$, as mentioned before.

Under normal incidence different structures have been observed using AFM. Earlier studies show (similar to HCI with high charge states [67]) caldera like defects. In crystalline TiO₂ craters with a hillock inside are visible after irradiation with 40 MeV I⁹⁺ ions, whereas 46 MeV I¹⁰⁺ ions induce hillocks [68]. The irradiation of TiO₂ (100) surfaces with 103 MeV Pb ions shows creation of single hillocks, in the height and radius range of SrTiO₃ [63]. The dimensions of the protrusions depend on the used

projectile, e.g. 1 GeV Ta ions create only one nm high dots [68]. Hillocks induced by 150 MeV Au ions disappeared after chemical etching with 20 % hydrofluoric acid [69].

On the surface of thin films of amorphous TiO₂ hillocks (induced by irradiation with 100 MeV Au ions) are only observable after rapid thermal annealing up to 350 °C [70].

Observations with grazing angle X-ray diffraction (GAXRD) and Raman spectroscopy show that the irradiation of amorphous TiO₂ film with SHI can modify the structure of the target material. Around the ion path a nanocrystalline phase is formed out of the amorphous one [71]. By using higher ion beam fluences the anatase² phase of TiO₂ can be transformed to rutile [72].

1.5.3 CaF₂

In 2002 for the first time individual single hillocks after normal incidence with SHI have been observed by Müller *et al.* [73] by using AFM after irradiation of CaF₂ (111) single crystal surfaces. Both, the height and the diameter of the created hillocks depend on the stopping power $S_{elec}(E)$. The hillock heights are increasing linearly up to ≈ 6 nm for $S = 35$ keV/nm. The nanodots have diameters in the range of 15 nm to 35 nm, which can be fitted by the square root of the stopping power. A correlation between the height and diameter has been observed by Khalfouni *et al.* [74]. The heights are linearly increasing with the diameter, the gradient depends on the used ions. In order to investigate the hillock geometry simulations have been performed to reproduce the height-diameter correlation. Good agreement with the measurements was found for elliptical and Gaussian shapes, whereas a hemi-circular approach did not work [74].

The dimensions of the nanodots depend on the imaging conditions, observed with AFM after normal irradiation with 11.1 MeV/u (2.3 GeV) Bi ions [75]. Imaging in contact mode under vacuum leads to higher hillocks. Independent of the used scanning mode and the environmental conditions conical hillocks with a circular base were observed.

The efficiency of hillock formation (defined as the number of created hillocks over the number of incident ions) also depends on the energy loss [74, 76]. At stopping powers above the threshold for nanostructure creation of ≈ 5 keV/nm [74], but below a stopping power of 12 keV/nm the efficiency is increasing approximately linear. Above this value 100% efficiency is reported (see Figure 1.4).

First investigations under glancing angles have been performed by Akcöltekin *et*

²TiO₂ has three phases anatase, rutile and broocite. They differ in their crystalline structure.

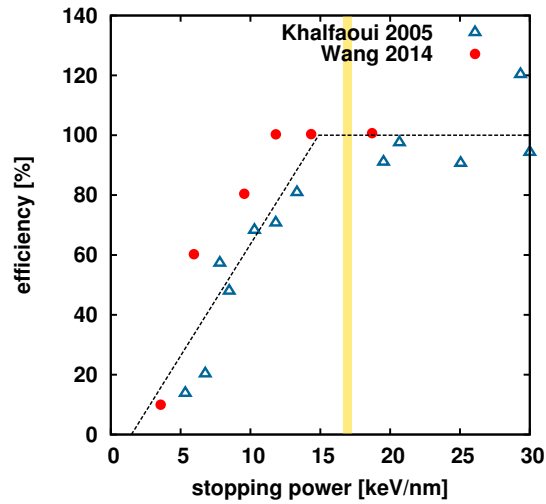


Figure 1.4: Efficiency of nanostructure creation on CaF_2 surfaces in dependence on the stopping power. The plot uses data of Khalfaoui *et al.* [74] and Wang *et al.* [76]. Black dashed lines represents fits and the yellow area the stopping power range investigated in that thesis.

al. [63]. The irradiation leads to the creation of a chain of hillocks similar to SrTiO_3 and TiO_2 . This kind of nanostructure has also been investigated with eddy current microscopy (ECM) [77], a particular mode of an AFM where a magnetic tip is oscillating. A metallisation is observed, indicating that the nanodots are made of Ca, corresponding with an F depletion. This observation is in agreement with previously studies using transmission electron microscopy [78]. After irradiation with cluster ions in the MeV energy regime, an intermittent structure has been observed. These tracks were interpreted as consisting of aligned faceted anion voids, corresponding to Ca inclusions.

Swift heavy ion irradiation of CaF_2 can lead to an additional effect, namely the swelling of the target material, which increases with fluence and electronic stopping power [79, 80]. The effect is observed when measuring the step height between non-irradiated and irradiated areas. The threshold for this volume expansion is consistent with the threshold for track formation (5 keV/nm).

1.5.4 Mica

Muscovite mica is one of the first materials which has been irradiated with HCI and SHI. Under normal incidence first studies reported the creation of hollows with a diameter of 5.5 nm at a stopping power of 10.9 keV/nm [81]. Later hillocks were

observed after irradiation with 78.2 MeV ^{127}I ions [82]. It was mentioned that the dimensions of the nanodots varied with the used AFM mode. In tapping mode hillocks with a height of typically 0.5 nm are found.

Several studies show that the diameter of the ion track is increasing with the stopping power [81, 83, 84]. However also this property seems to depend on the used analysis technique. Tracks observed with AFM show rather large diameters whereas small angle X-ray and neutron scattering studies show smaller values [84]. The threshold for track formation on muscovite mica has been found to be around $< 5 \text{ keV/nm}$ [81].

Besides studies on muscovite mica irradiations has been performed on natural mica (dark mica, phlogopite) with ^{58}Ni ions at kinetic energies between 3.2 MeV and 81.2 MeV by Lang *et al.* [85]. After chemical etching with hydrofluoric acid a change in the shape of the etch pit from triangular to hexagonal geometry at an energy loss between 5.6 keV/nm and 6.6 keV/nm has been reported by observation with scanning electron microscopy. The reason for the formations of different etch shapes is that the track changes from a discontinuous structure to a continuous one.

Irradiations have also been performed under grazing angles. Daya [86] used 20 MeV C_{60}^+ cluster ions (here S_{nucl} dominates) for bombardment under small angles of 12° . Images of the surface show the creation of $\approx 9 \text{ nm}$ high hillock like structures with a split, that is followed by a tail in ion direction. However the cross section of the nanodots is not a circle anymore, the width is 50 nm at a length of 85 nm. The mentioned split is a crater with a depth of less than 1 nm. A comparable irradiation geometry (incidence angle 23°) using monoatomic ions (78.2 MeV ^{127}I) leads to a similar nanostructure, a hillock with a tail along the ion trajectory [87].

2 Materials and methods

2.1 Irradiations at the IRRSUD beam line

The irradiations of the samples with swift heavy ions in an energy range between 23 MeV and 100 MeV took place at the IRRSUD beamline at GANIL (Grand Accélérateur National d'Ions Lourds), Caen, France. The investigated materials were irradiated within five measurement periods between November 2013 and June 2015. An overview of the irradiations is given in [Appendix A](#).

For the irradiations the targets were mounted on a rotatable holder. The angle of incidence, measured with respect to the surface plane, can be varied between 0° and 90° with an accuracy of 0.2° [14]. The adjusted angle can be checked with the relation

$$\varphi_{calc} = \arcsin(N/D) \quad (2.1)$$

where N represents the number of ion tracks per area obtained from AFM images and D the ion dose (for a comparison of nominal and calculated angles see [Appendix A](#)). The uncertainty of the calculated angle is roughly estimated as $\pm 0.2^\circ$. A more detailed description of the angle determination can be found in [88].

In the following for plots and discussion the calculated angle φ_{calc} is used, that is renamed to φ .

To reduce the kinetic energy of the incoming ions an aluminium film in front of the target, a so called degrader, was used. Experiments with lower beam energies have been performed with ^{129}Xe ions at an initially kinetic energy of 92 MeV. The influence of the degrader thickness on the energy is summarised in [Table 2.1](#). In the first irradiation period of mica with a $3\mu\text{m}$ thick degrader ^{136}Xe ions @ 95 MeV were used. The outgoing energy of the ions is 55 MeV. In the following this target is treated as the two 53 MeV samples of that material.

Table 2.1: Kinetic energy of the incoming ions by using a degrader in front of the target as calculated using TRIM [55].

incoming beam energy	degrader thickness	resulting energy
92 MeV	no degrader	92 MeV
92 MeV	1.5 μm	72 MeV
92 MeV	3 μm	53 MeV
92 MeV	6 μm	23 MeV

To provide measurements with target temperatures above room temperature a self constructed heater was used [88]. Irradiations were performed at room temperature, at 200 °C (mica) and at 400 °C (CaF₂, mica). For an overview see [Appendix A](#). All irradiations without temperature specification took place under room temperature conditions.

2.2 Atomic force microscopy

An *Asylum Research Cypher Scanning Probe Microscope* was used to study the nanostructures induced by SHI. The microscope is working under ambient conditions and is positioned on an 15 cm thick marble plate to reduce vibrations. The software *Igor* is controlling the machine. A picture of the AFM-setup is shown in [Figure 2.1](#).

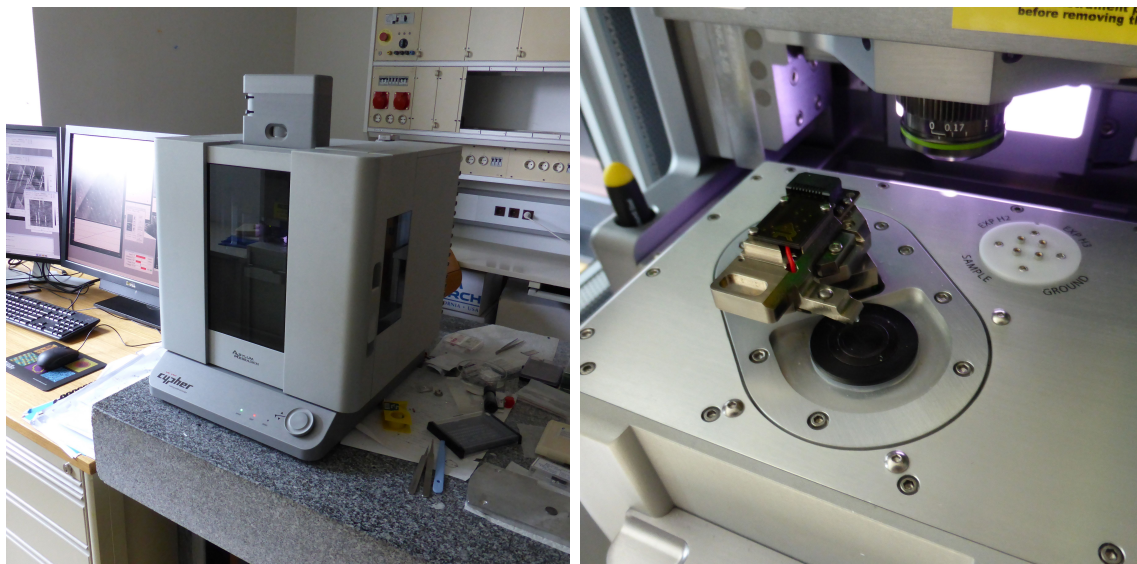


Figure 2.1: Pictures of the *Cypher* AFM, left the complete microscope, right a view on the scanning stage and the tip holder.

The samples are fixed with copper tape on the magnetic sample holder, which is then attached to the scanning stage.

2.2.1 Working principle

Atomic force microscopes (AFM) belong to the class of scanning probe microscopes (SPM) and have been invented by Binnig, Quate and Gerber in 1986 [89], five years after the development of the scanning tunnelling microscope (STM).

The basic concept of scanning probe microscopes is to detect the interaction between a sharp probe and the sample. This signal is recorded by the probe at every imaging point while scanning over the surface to obtain information about the surface topography.

In the case of AFM, a tip is used as probe to detect small forces ($< 1 \text{ nN}$) between the tip and the surface. The forces are monitored while the probe is scanning in contact or in small height over the surface. To detect this interaction the tip is mounted on a cantilever, so that the tip-surface forces influence the cantilever position. A laser is directed on the cantilever so that the beam is reflected in a four-quadrant photo diode. The position of the laser spot in the sensor depends on the cantilever deflection. The raster scan across the sample is due to movement of the sample by piezoelectric crystals. The tip-cantilever arrangement is static. [Figure 2.2](#) shows the working principle of the microscope. The recorded signal is mathematically a convolution of the tip geometry and the surface.

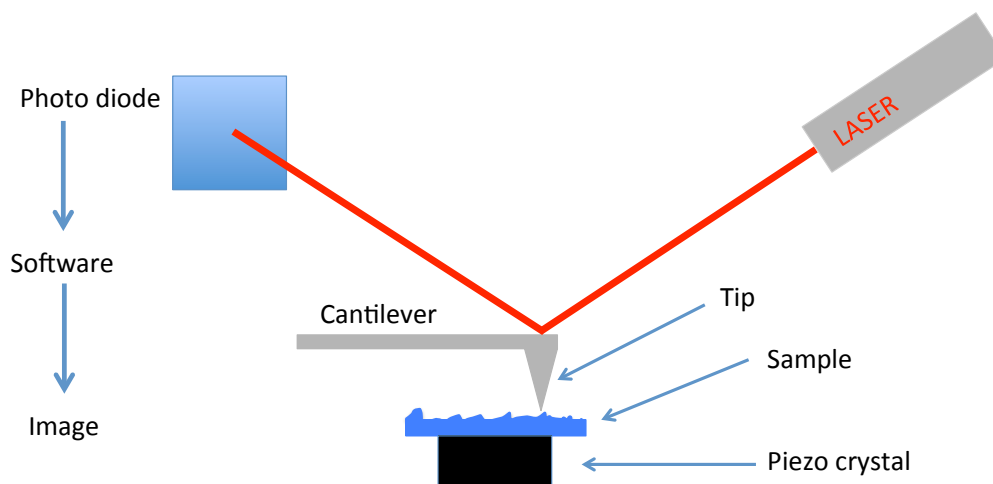


Figure 2.2: The working principle of an atomic force microscope.

2.2.2 Imaging modes

In the following the two topographic imaging modes are introduced which are used in the course of this thesis. All targets have been imaged in topographic tapping mode, except few SrTiO₃ and CaF₂ samples. Here the imaging has been performed with topographic contact mode.

Contact mode

In contact mode a tip with a low cantilever spring constant (0.08 N/m for the tips we used) is scanning in close contact with the surface. Repulsive forces due to electronic orbital overlap of the tip atoms with the surface ones are monitored. The deflection of the laser beam is compared with the setpoint, a set value of deflection. The cantilever is connected with a piezo positioning element. The voltage applied on the piezo crystal is given by a DC feedback amplifier to shift the cantilever height relative to the surface so that the deflection value correlates with the setpoint. The recorded height is depending on the voltage applied to the piezo crystal.

Tapping mode

Tapping mode (also known as intermittent mode) is the ideal imaging technique for samples that are easily damaged. At each lateral position the tip is approached until it taps the surface. Then it is removed to prevent scratching the surface during movement to the next scanning point. During the scanning process the cantilever is oscillating, driven by a piezoelectric crystal near its resonance frequency³. The amplitude is typically in a range of a few tens of nm which is reduced during approaching the surface until the tip is tapping the surface. In contrast to the contact mode, where the deflection is compared with a setpoint, for tapping a feedback loop keeps this amplitude on a constant preset value. Additionally to the amplitude the phase between the driving frequency and the cantilever oscillation is monitored. The phase depends on properties of the surface material like adhesion and friction. [Figure 2.3](#) compares the different imaging signals of the tapping mode.

³In our measurements the driving frequency was assumed 3% under the resonance frequency.

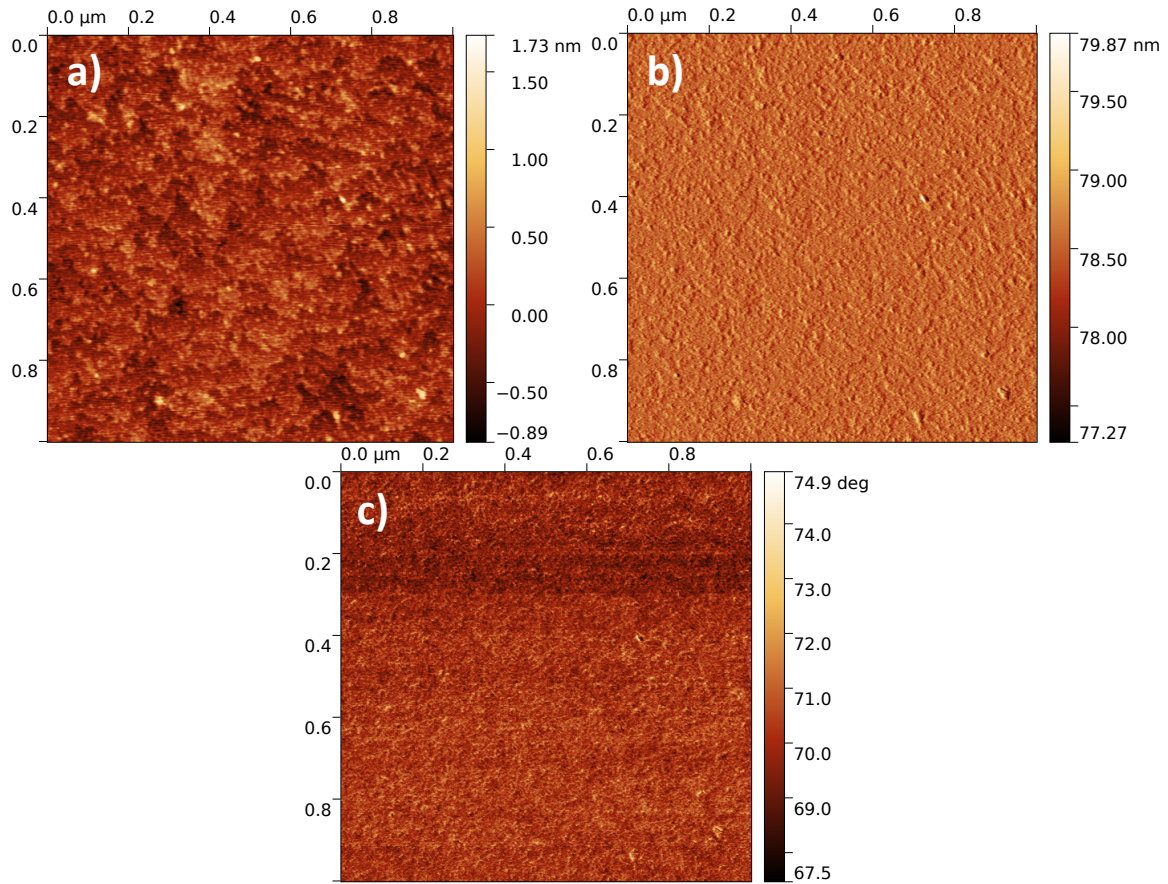


Figure 2.3: AFM images of SrTiO₃ performed in Tapping mode, a) height image, b) amplitude image, c) phase image.

2.3 Investigated materials

In the course of this diploma thesis four materials have been irradiated with swift heavy ions. This section describes their physical properties e.g. the crystalline structure. The software 'Avogadro' [90, 91] has been used to plot the crystalline structure of the different target materials. The AFM images have been evaluated using the software packages *Gwyddion* [92] and *WSxM* [93]. Also an overview of the necessary target preparation procedure is given.

2.3.1 Strontium titanate SrTiO₃

SrTiO₃ is an oxide consisting of Sr²⁺, Ti⁴⁺ and O²⁻ ions. The crystalline structure is cubic (perovskite type). A model is shown in Figure 2.4 (left). An AFM image (see Figure 2.4 right) shows the surface of the non-irradiated crystal. The root mean

square (RMS) roughness of that image is calculated as 195 pm.

Before irradiation the samples were imaged with AFM to check the degree of contamination. No additionally sample preparation is necessary. Our samples are 0.7 cm x 0.7 cm large platelets (SurfaceNet) in (100) orientation with a thickness of 0.5 mm.

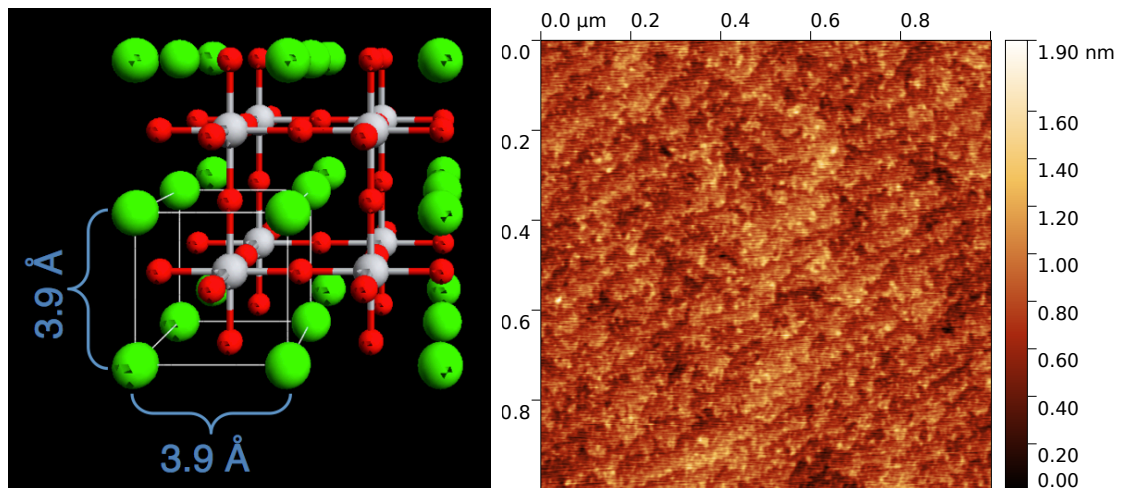


Figure 2.4: left: Crystalline structure of SrTiO₃: green balls are Sr, grey Ti and red O. right: AFM tapping mode image of an unirradiated sample.

2.3.2 Titanium oxide TiO₂

Titanium oxide is an oxide consisting of Ti⁴⁺ and O²⁻ ions. In nature three different crystal modifications (rutile, anatase and brookite) occur. They distinguish in their crystal system and e.g. in their colour. For our irradiations we used rutile platelets (SurfaceNet) of 0.7 cm x 0.7 cm with a thickness of 0.5 mm in (100) orientation. The tetragonal crystal structure is plotted in [Figure 2.5](#) (left). An AFM image of the surface of an unirradiated sample with a RMS of 171 pm is shown in [Figure 2.5](#) (right).

Similar to SrTiO₃ no sample preparation before irradiation is necessary.

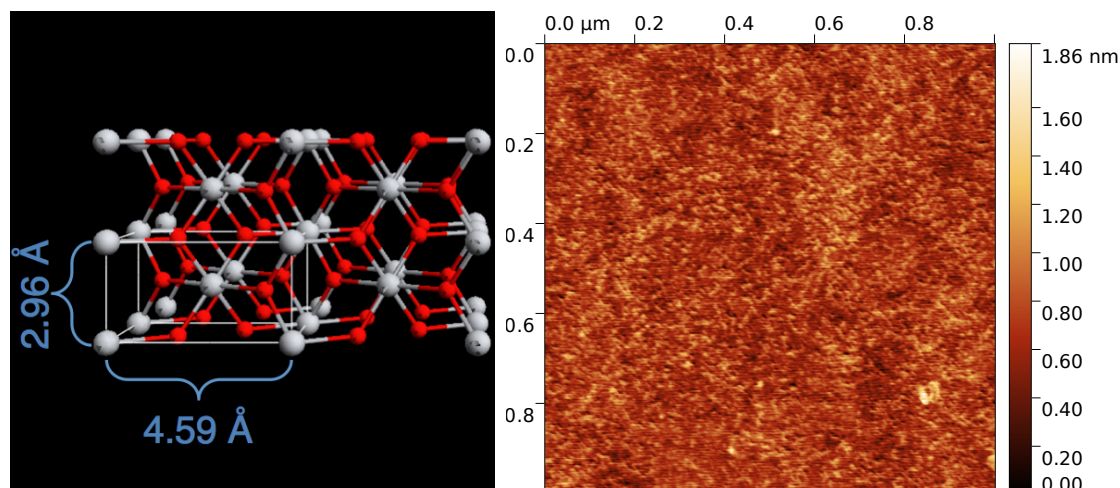


Figure 2.5: left: Crystalline structure of TiO_2 , grey balls are Ti and red ones O. right: AFM tapping mode image of an unirradiated sample.

2.3.3 Calcium fluoride CaF_2

Calcium fluoride (also known as fluorite) is an ionic crystal compounded out of calcium and fluorine ions. The crystals have a cubic lattice with Ca^{2+} ions at the corners and faces. The eight F^- ions are located so that each of them is surrounded by four Ca^{2+} ions (see [Figure 2.6 left](#)).

AFM images of unirradiated samples (crystals (Crystec, Korth), freshly cleaved along the (111) plane (see [Figure 2.6 right](#))) show flat terraces (with a RMS roughness of 55 pm on a terrace) with a step height of less than half a nm.

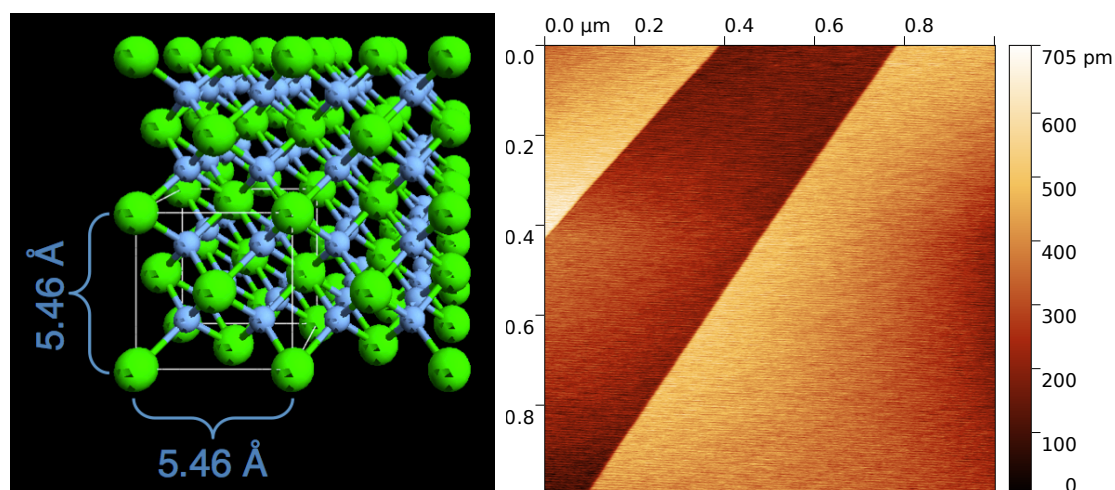


Figure 2.6: left: Crystalline structure of CaF_2 : green balls are Ca, blue ones F. right: AFM tapping mode image of an unirradiated sample.

In the case of CaF_2 the target preparation before irradiation is very important, because after few hours under ambient conditions island structures are growing on the surface (see Figure 2.7b). First the roughness of the target is increasing. Small defects are growing and float together to larger ones. One day after cleaving the height of the island has been increased up to 0.5 nm (see Figure 2.7b). After four days a large part of the surface is covered with the structure, that is now at least 1 nm high (Figure 2.8a).

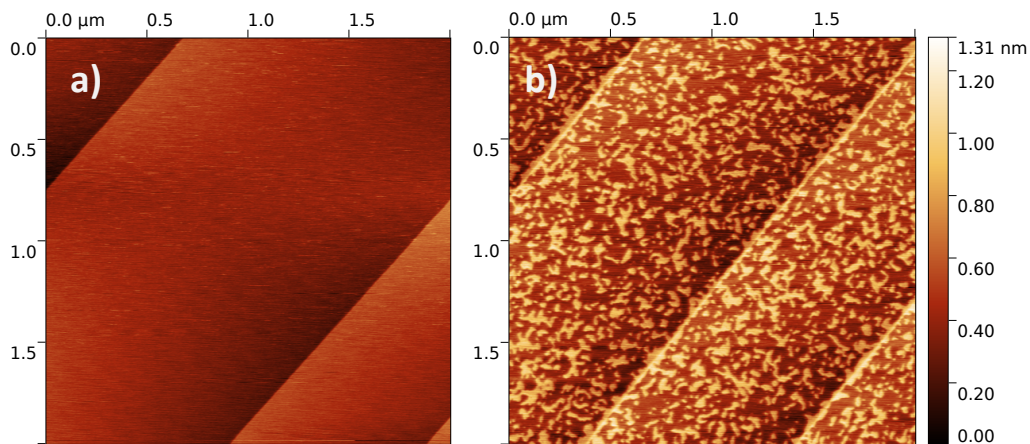


Figure 2.7: AFM images of a CaF_2 surface, a) one hour after cleaving and b) 28 hours after cleaving (same crystal).

Water is a possible adsorbate that creates this pattern [94–96]. Heating the targets to 400°C results in a more stable surface similar to a freshly cleaved one which is shown in Figure 2.6 (right). To investigate the behaviour of the new surface a covered CaF_2 target has been imaged with AFM before and after heating (Figures 2.8a and 2.8b). Two weeks after heating the surface is rougher than freshly after heating, but the typical islands are not visible (Figure 2.8c).

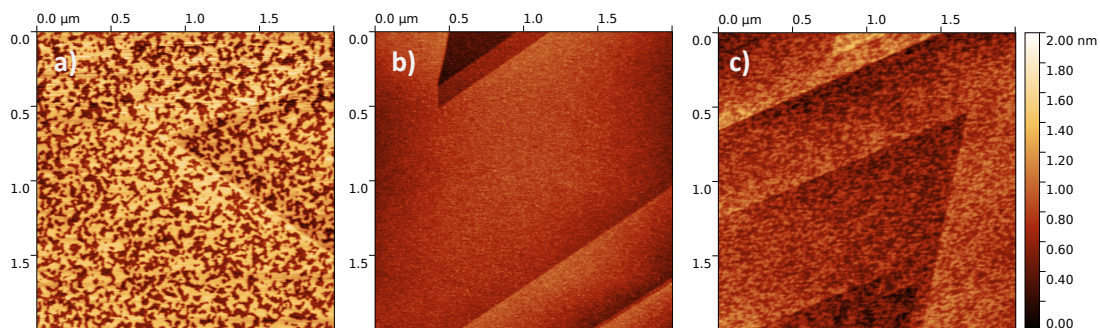


Figure 2.8: AFM images of CaF_2 , a) 4 days after cleaving, b) one hour after heating up to 350°C , c) two weeks after heating.

Furthermore, the influence of the heating temperature was studied (Figure 2.9). A covered CaF_2 platelet was heated to 250°C . After heating huge islands are visible on the surface (see Figure 2.9b). This structure is not stable, after one day it melted to lots of small defects. In the following all CaF_2 targets were heated to 400°C for at least 10 hours before irradiation. A temperature of 250°C is obviously not enough.

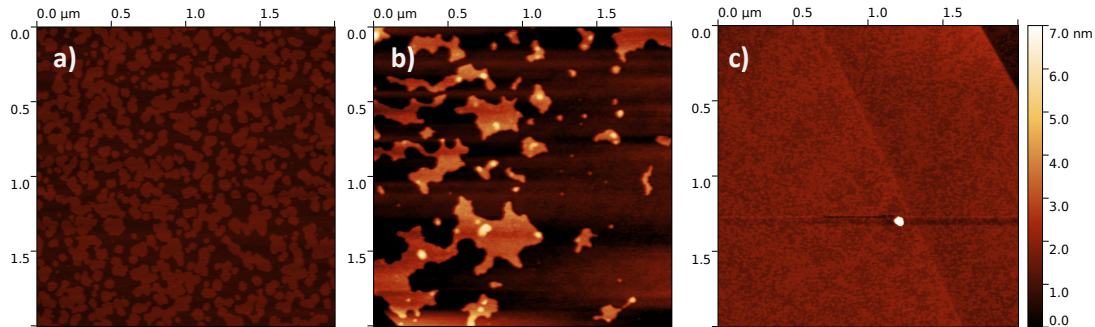


Figure 2.9: AFM images of CaF_2 , a) 36 hours after cleaving, b) freshly after heating up to 250°C , c) one day after heating.

2.3.4 Mica

Mica is a group of sheet silicates including materials with a similar sum formula with typical interlayer distances of 1 nm. It can be perfectly cleaved along the $\{001\}$ plane (see the AFM image in the right part of Figure 2.10 and shows a RMS roughness of 47 pm). The material composites of layers with a negative net charge and positive charged ions (e.g. K^+) in between to achieve charge neutrality [97]. An image of the atomic structure is shown in Figure 2.10 (left).

In the course of this thesis two different micas have been irradiated:

- Muscovite mica (Richard Jahre) with the sum formula $\text{KAl}_2[\text{AlSi}_3\text{O}_{10}(\text{OH})_2]$
- Fluorphlogopite mica (TaiYuan) with the sum formula $\text{KMg}_3[\text{AlSi}_3\text{O}_{10}]\text{F}_2$

In the following of this thesis muscovite mica is notated as mica-OH or only as mica, whereas fluorphlogopite mica is explicitly meant by mica-F.

To provide clean surfaces the top layers of the sample are removed by tape before irradiation.

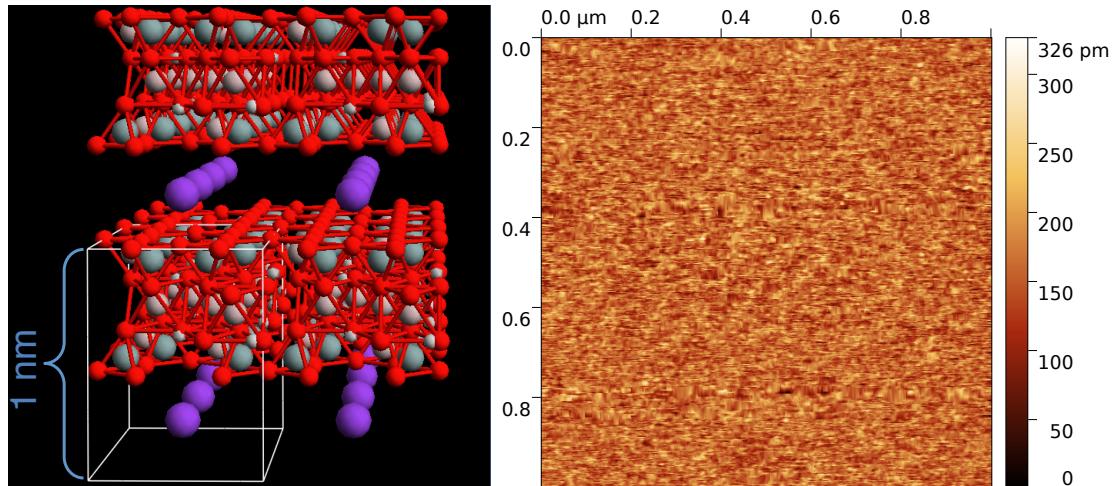


Figure 2.10: left: Crystalline structure of mica-OH: purple balls are K, grey-pink Al, grey-blue Si, grey H and red O. right: AFM tapping mode image of an unirradiated sample.

2.4 Energy loss calculations

The SRIM⁴ code [48, 55, 98] has been used for the calculation of the ions energy loss. Target density (see table 2.2), composition and the ion nucleus are the necessary inputs to compute the stopping power S (corresponds with the negative energy loss dE/dx) and the ion range in matter for arbitrary projectile energies. All the calculations are independent of the ions charge state.

Table 2.2: Overview of target densities used for the SRIM energy loss calculations.

target material	SrTiO ₃	TiO ₂	CaF ₂	mica (OH and F)
density [g/cm ³]	5.12	4.26	3.18	2.81

A typical energy loss curve is shown in Figure 2.11. Here muscovite mica is the target and ¹²⁹Xe ions are used as incident particles. As introduced in Chapter 1.4 the stopping power is composited of two parts, nuclear stopping S_{nucl} and electronic stopping S_{elec} . In the investigated energy range between 23 MeV and 100 MeV (highlighted by the yellow area) the electronic part is dominating. For further analysis the total energy loss $S_{tot} = S_{nucl} + S_{elec}$ has been used.

⁴SRIM is an acronym for Stopping and Range of Ions in Matter

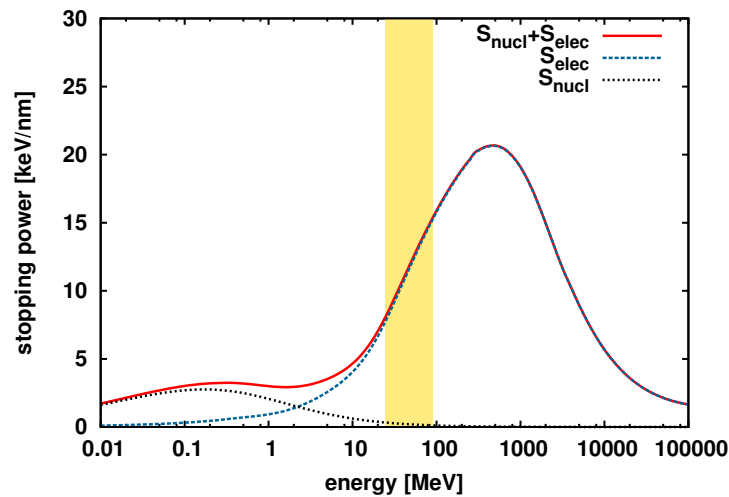


Figure 2.11: SRIM calculation of the energy loss of ^{129}Xe ions in muscovite mica. The yellow area represents the investigated energy range (23 MeV to 100 MeV).

Mica is the only material irradiated with different Xe and Pb ions. The energy loss of the used projectiles are compared in Figure 2.12. The two xenon isotopes show only small discrepancies, whereas the lead ions show a higher stopping power. Table 2.3 contains the resulting stopping power of all four investigated materials for all irradiation energies. In mica the energy loss of ^{129}Xe ions @ 92 MeV and ^{136}Xe @ 95 MeV is almost the same. So these two different irradiations are joined to one single data point with the average of both energy loss values.

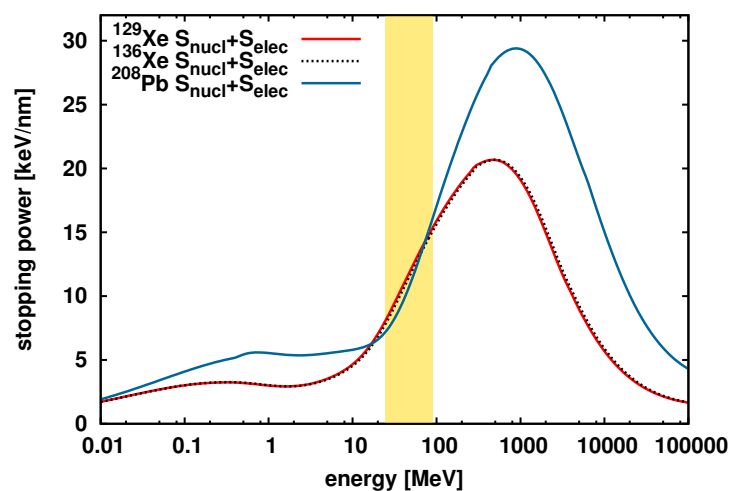


Figure 2.12: SRIM energy loss calculation of different ions on mica. The yellow area represents the investigated energy range (23 MeV to 100 MeV).

Table 2.3: SRIM calculated stopping power; for mica: ^mXe represents the average of ^{129}Xe @ 92 MeV and ^{136}Xe @ 95 MeV ions.

ions	energy	target	S_{elec} [keV/nm]	S_{nucl} [keV/nm]	S_{tot} [keV/nm]
^{129}Xe	53 MeV	TiO_2	17.050	0.246	17.296
^{129}Xe	53 MeV	SrTiO_3	16.830	0.268	17.098
^{136}Xe	95 MeV	CaF_2	16.400	0.126	16.526
^{208}Pb	100 MeV	CaF_2	17.590	0.360	17.750
^{129}Xe	23 MeV	mica	7.381	0.343	7.724
^{129}Xe	53 MeV	mica	12.530	0.177	12.707
^{129}Xe	72 MeV	mica	14.050	0.143	14.193
^{129}Xe	92 MeV	mica	15.360	0.118	15.478
^{136}Xe	95 MeV	mica	15.299	0.119	15.418
^mXe	≈ 92 MeV	mica	- - -	- - -	15.448
^{208}Pb	100 MeV	mica	16.580	0.336	16.916
^{129}Xe	92 MeV	mica-F	15.230	0.117	15.346

3 Experimental results and discussion

3.1 Experimental results I - SrTiO₃ and TiO₂

3.1.1 SrTiO₃

Due to the large data set available for SHI irradiation of SrTiO₃ under grazing angles (e.g. [15] and described in more detail in [Chapter 1.5.1](#)), SrTiO₃ was chosen as the test material of our investigations. Our first irradiations were performed with 92 MeV Xe ions and will be reported in the PhD-Thesis of E. Gruber [99]. To investigate the nanostructure creation for different projectile energies two additionally targets were irradiated with 53 MeV Xe ions under grazing angles of 0.9° and 2.0°, respectively, which are analysed in the next pages and compared with earlier studies performed at higher kinetic energies. The deceleration of the ions has been performed with a degrader foil (see also [Chapter 2.1](#)).

3.1.2 SrTiO₃ - Topography

The topography of a SrTiO₃ surface after SHI irradiation is shown in [Figure 3.1](#) and a 3d plot in [Figure 3.2](#). The AFM images show the creation of parallel arranged tracks with a length of several 100 nm, each induced by a single ion impact. Each of these nanostructures consists of a chain of single nanodots with heights up to 3 nm. This chain is followed by a fading protrusion. High resolution AFM images show the creation of a groove with a depth of a few tenths of nm in front of the track at the impact site of the projectile ion (see the marks in the right AFM image of [Figure 3.1](#)). By laying a slice along the ion direction through the middle of the track this groove is easier observable (see e.g. the height profile in [Figure 3.3](#)).

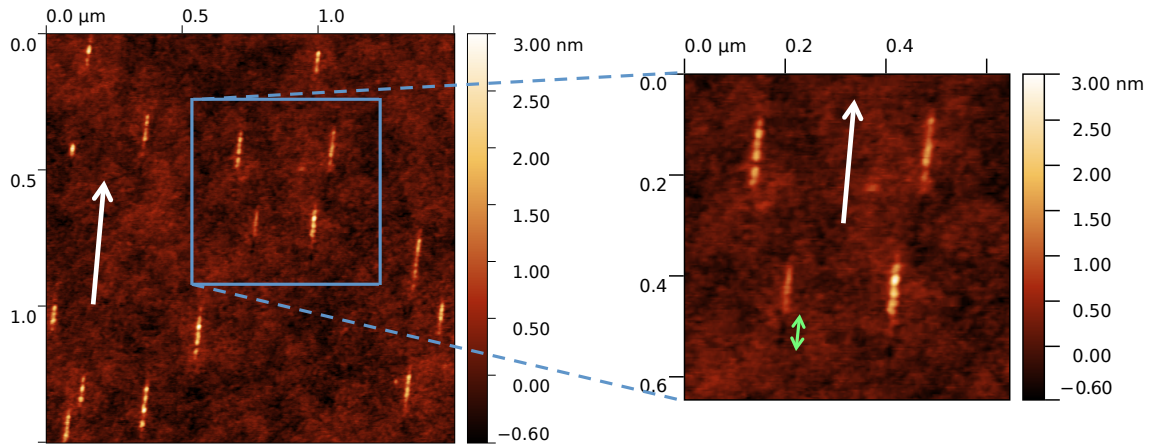


Figure 3.1: AFM images of SrTiO₃ irradiated under a grazing angle of 2.0°, white arrows indicate the ion direction. The green arrow in the right image highlights a groove in front of the track left to it.

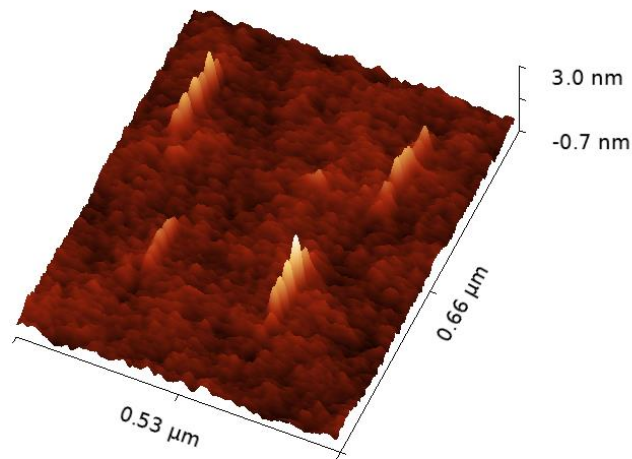


Figure 3.2: 3d plot AFM image of SrTiO₃.

3.1.3 SrTiO₃ - Analysis of the nanostructure

In the following two lengths of the nanostructure will be introduced. The long one l_L describes the complete length of the surface modification from the first visible modification, in the case of SrTiO₃ a groove, to the end of the tail. The short length l_S identifies the length of the hillock chain, more precisely the distance between the peak of the first and the last nanodot of a single chain. A height profile of a SrTiO₃

track including the two lengths is plotted in Figure 3.3.

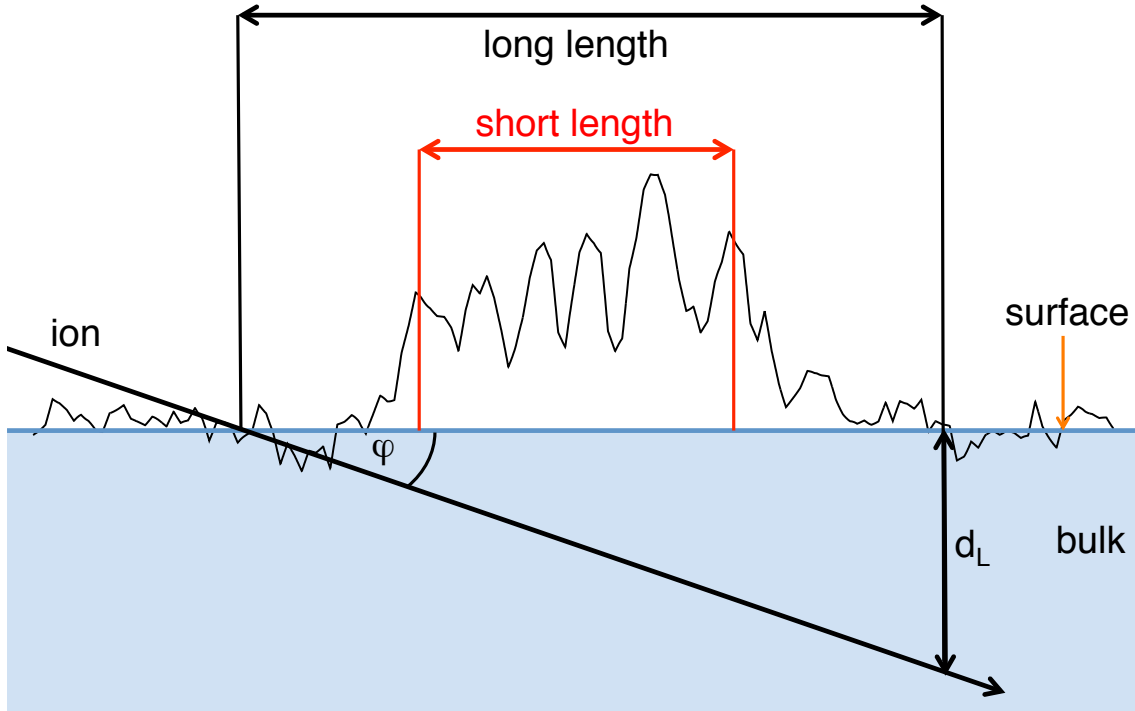


Figure 3.3: Height profile of an irradiated SrTiO₃ surface with a 600 nm long track, consisting of a chain of single nanodots (~ 2.2 nm high) and a shallow groove at the impact site. Short length (red line) and long length (black line) are plotted.

The depth d_L can be calculated by the geometric relation

$$d_L = \bar{l}_L \cdot \tan(\varphi), \quad (3.1)$$

where \bar{l}_L is the average long length. Akcöltekin *et al.* [15] postulated an angle independent depth, from which the ion induced damage can still be detected. By plotting the track length for different incident angles and fitting the data with the before given relation (equation (3.1)), the characteristic depth d can be evaluated.

Both investigated lengths of the two 53 MeV SrTiO₃ samples are plotted over the incidence angle in Figure 3.4. The shorter the angle of incidence the longer the track. In comparison with data of higher kinetic energies one can see that 53 MeV lengths are systematically shorter. Due to SRIM calculated track lengths of a few μm a discrepancy in the lengths between the different energies should not be observable. A possible explanation is that the lower energy loss of the 53 MeV projectiles induces nanostructures with a smaller height what makes them more difficult for AFM investigations. Consequently the fading ends of the tracks are not measured any

more.

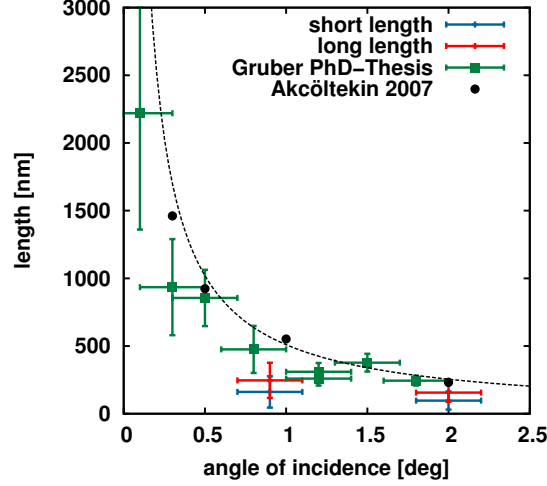


Figure 3.4: The short and long lengths of the two 53 MeV SrTiO₃ samples plotted over the angle of incidence. The data points are compared with data from Akcöltekin *et al.* [15] and of our group provided by E. Gruber [99] (unpublished).

To provide a better description of the nanostructure formation, further properties were analysed:

- First the height h of the hillocks was investigated. The mean value of the height of all hillocks is:

$$h_{0.9^\circ} = 2.0 \text{ nm} \pm 0.5 \text{ nm}$$

$$h_{2.0^\circ} = 2.2 \text{ nm} \pm 0.5 \text{ nm}$$

- N represents the number of hillocks of the tracks. A histogram with this property is shown in Figure 3.5. The average numbers of hillocks are:

$$N_{0.9^\circ} = 6.55 \pm 3.78$$

$$N_{2.0^\circ} = 4.73 \pm 2.32$$

As one can see in the figure the deviation of hillocks per chain is asymmetric. The plot of the 2.0° data shows a shifted deviation in relation to the 0.9° one, what corresponds with the lower mean value.

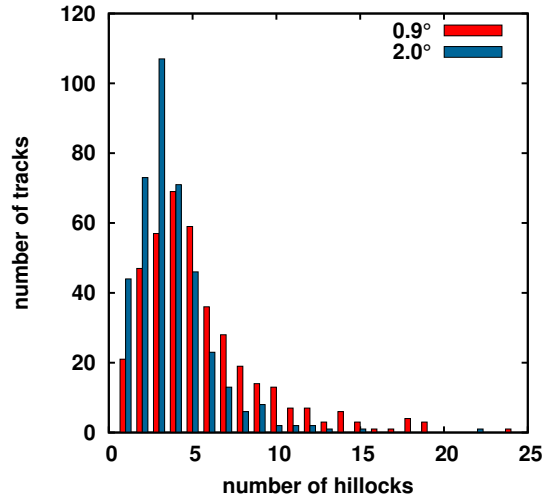


Figure 3.5: The histogram shows the number of tracks as a function of the number of hillocks. In total 400 tracks were analysed.

- The average spacing s between two neighboured periodically arranged hillocks has been defined as

$$s = l_S / (N - 1), \quad (3.2)$$

where l_S is the length of the hillock chain and N the number of nanodots of the investigated track.

$$s_{0.9^\circ} = 22.20 \text{ nm} \pm 5.70 \text{ nm}$$

$$s_{2.0^\circ} = 26.33 \text{ nm} \pm 5.83 \text{ nm}$$

- The most difficult parameter to evaluate is the depth of the groove at impact site. Since a groove formation could be seen only on a limited number of tracks, not all tracks could be analysed. In the following the average depth of the groove had been evaluated as follows:

for the 0.9° target: $0.27 \text{ nm} \pm 0.07 \text{ nm}$

and the 2.0° target: $0.27 \text{ nm} \pm 0.08 \text{ nm}$

One can see that the depth of the groove is roughly one fourth of a nanometer for both available targets.

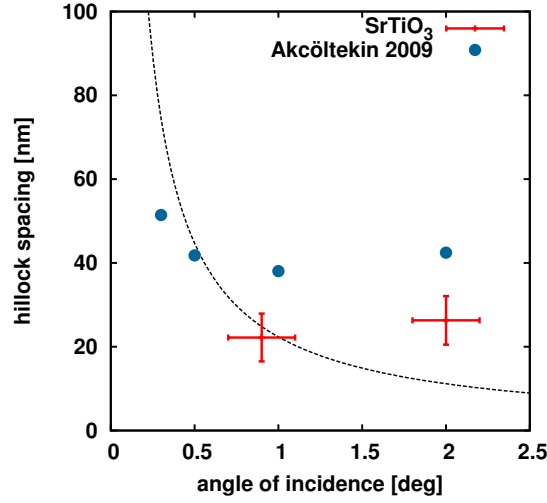


Figure 3.6: The average hillock spacing in dependence of the incidence angle. The data points of the 53 MeV SrTiO₃ targets are compared with measurements by Akcöltekin *et al.* [63]. The dashed line represents the $a/\tan(\varphi)$ fit (see [63]) with $a = 0.39$ nm being the lattice constant of SrTiO₃.

Length and angular distribution

The length and incident angle distribution of the SrTiO₃ tracks have been evaluated by using the total length and the length of the hillock chain respectively of 400 investigated tracks. The number of tracks $N(x)$ were summarised over a length interval of $\Delta x = 10$ nm. To provide a smoother distribution the values of two neighboured slots were averaged to

$$N(x) = \frac{N(x - \Delta x, x] + N(x, x + \Delta x]}{2}, \quad (3.3)$$

where

$$N(x - \Delta x, x] \quad (3.4)$$

is the number of tracks with a length in the interval $(x - \Delta x, x]$. These data were compared with Gaussian shapes, so the probability density $p(x)$ could be formed out of the $N(x)$ by

$$p(x) = \frac{N(x)}{N_{tot} \cdot \Delta x}. \quad (3.5)$$

Here N_{tot} represents the total number of analysed tracks. In the last step of this analysis the data points were fitted with Gaussian curves using *gnuplot* [100] (see Figure 3.7).

The angular distribution was calculated by

$$\varphi = \arctan(d_{S,L}/l_{S,L}) \quad (3.6)$$

that leads to the incidence angle of each single ion. The values for d were calculated again with

$$d_{S,L} = \bar{l}_{S,L} \cdot \tan(\varphi), \quad (3.7)$$

where \bar{l}_S is the average short and \bar{l}_L the average long length of the tracks of the investigated target, respectively (values taken from [Figure 3.4](#)). Adjusting the procedure for the $p(x)$, the probability densities of the angular distribution was calculated by using a step width of $\Delta\varphi = 0.1^\circ$. The final results of the SrTiO₃ targets are compared in [Figure 3.7](#) (length distribution) and [Figure 3.8](#) (angular distribution).

One can see the asymmetric distribution clearly, e.g. the number of tracks shorter than the mean value is always under the fit, where too many longer tracks are counted. The reason therefore is (in the case of a Gaussian angular distribution of the ion beam) the connection between length and incidence angle, given by

$$l = d/\tan(\varphi). \quad (3.8)$$

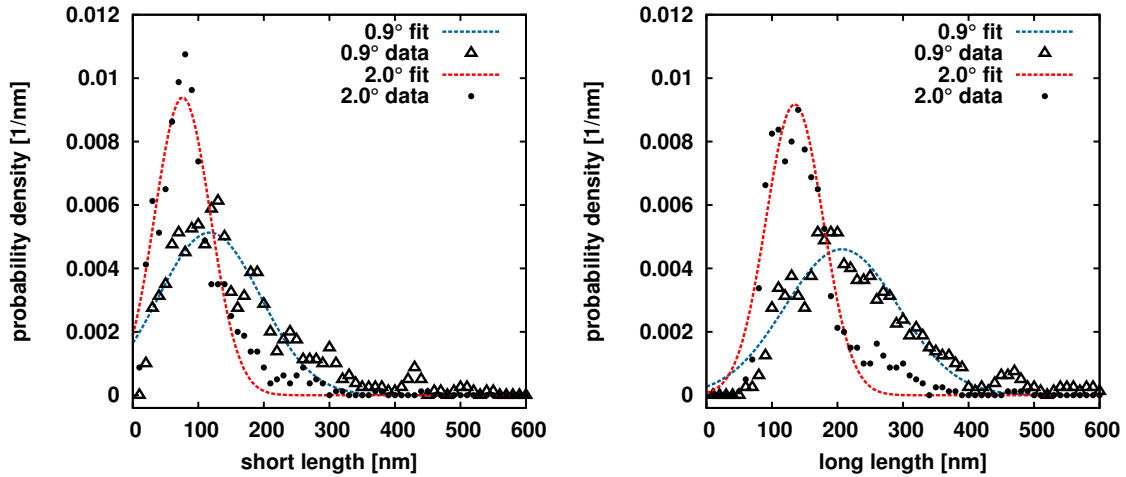


Figure 3.7: Length distribution of ion tracks on SrTiO₃, left short length, right long length (for definition see [Figure 3.3](#)).

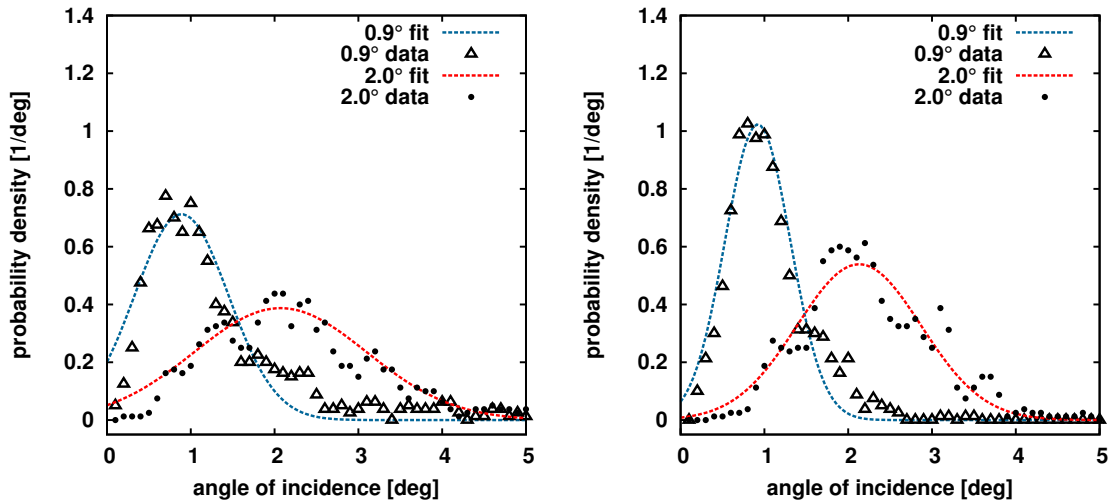


Figure 3.8: Angular distribution of ion tracks on SrTiO₃, left short length, right long length (for definition see Figure 3.3).

The Gaussian shapes of the angular distribution show that the mean value of the fitted angle is systematically larger than the calculated one. But for both targets the fitted angle is roughly the same for the distribution of the long and the short length. Similar to the length distributions the data points show here an asymmetric behaviour. In both distributions the widening of the beam is larger for the target with the larger angle of incidence.

3.1.4 TiO₂

To continue our measurements of the energy loss influence in nanostructure creation, we irradiated TiO₂ with different ion energies. Similar to SrTiO₃ two TiO₂ samples were irradiated with ¹²⁹Xe ions @ 53 MeV under incidence angles of $0.7^\circ \pm 0.2^\circ$ and $1.9^\circ \pm 0.2^\circ$, respectively. The previous investigations of TiO₂ with 92 MeV ions will be reported in the PhD-thesis of E. Gruber [99].

3.1.5 TiO₂ - Topography

The surface modification of TiO₂ is dominated by a chain of single hillocks, which is followed by a single protrusion. Until now no groove formation at the impact site of the ion could be observed (see Figure 3.9). A typical height profile of such a track is presented in Figure 3.10.

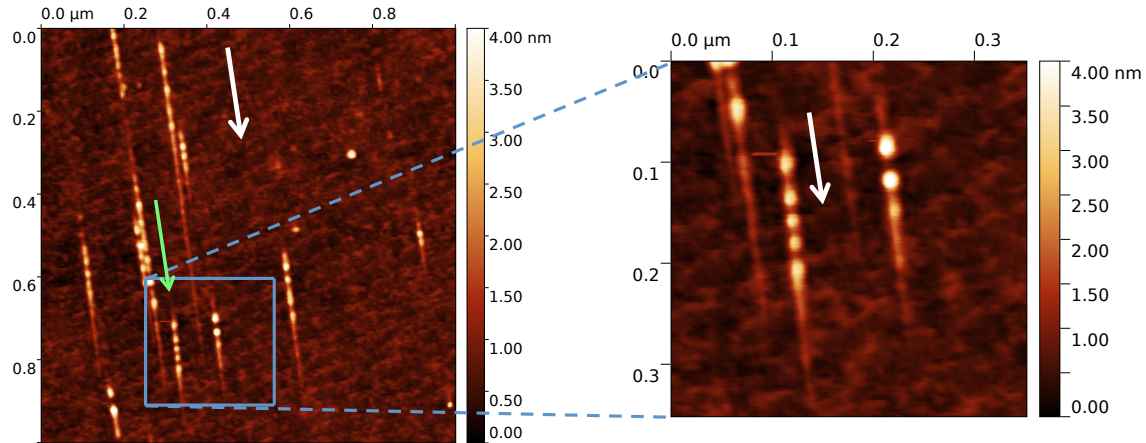


Figure 3.9: left: AFM image of TiO_2 irradiated with Xe ions @ 53 MeV ions under an angle of $\varphi = 0.75^\circ$. The white arrows indicate the projectile direction, the green arrow the position of the track profile shown in [Figure 3.10](#), right: a zoomed image of the nanostructure.

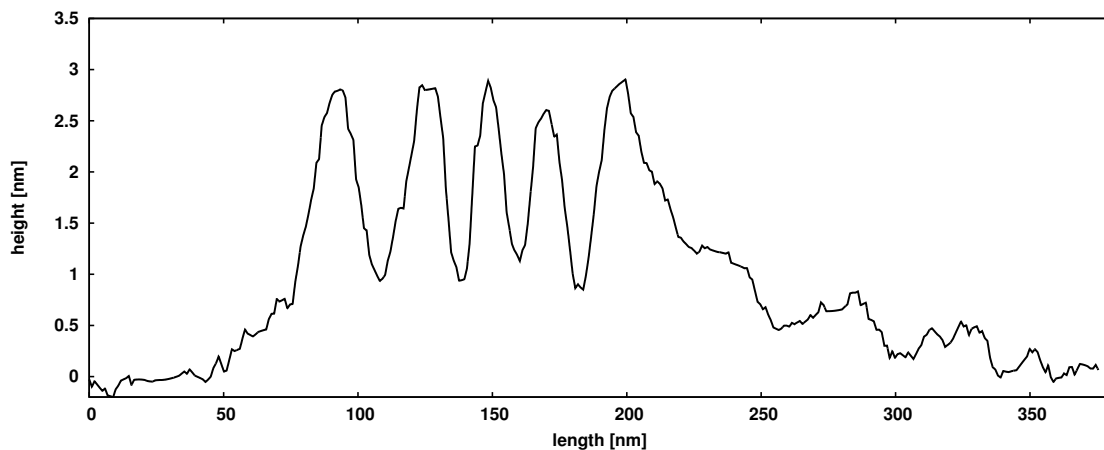


Figure 3.10: A profile of a track on TiO_2 after irradiation with 53 MeV Xe ions.

3.1.6 TiO_2 - Analysis of the nanostructure

The lengths of the TiO_2 tracks were defined and analysed in the same way as for SrTiO_3 (see again [Figure 3.3](#)). The lengths show the expected behaviour (the smaller incidence angle induces the longer track lengths). In [Figure 3.11](#) both lengths are plotted. In comparison to performed 92 MeV investigations [99], that are additionally included in the figure, the 53 MeV lengths are obviously shorter.

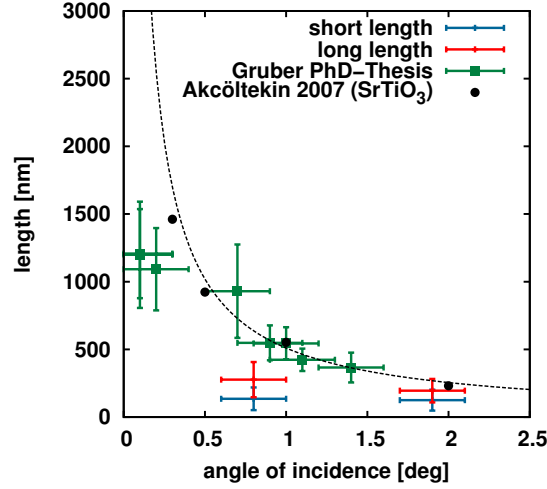


Figure 3.11: The short and long lengths of the two 53 MeV TiO₂ samples plotted over the angle of incidence. The data points are compared with measurements of our group at 92 MeV performed by E. Gruber [99]. For comparison SrTiO₃ values (black points) and the $9.8/\tan(\varphi)$ fit of Akcöltekin [15] are plotted.

Except the groove depth all properties introduced on page 32 were analysed for TiO₂ as well:

- The average height h of the hillocks:

$$h_{0.7^\circ} = 2.85 \text{ nm} \pm 0.75 \text{ nm}$$

$$h_{1.9^\circ} = 3.43 \text{ nm} \pm 1.18 \text{ nm}$$

- N , the number of hillocks of the tracks, shows due to the similar length of the hillock chains on both targets roughly the same values. Again a histogram with this property is shown in Figure 3.12. The average number of hillocks are:

$$N_{0.7^\circ} = 5.73 \pm 2.82$$

$$N_{1.9^\circ} = 5.56 \pm 2.97$$

Due to the small discrepancy in the average number of hillocks both deviations in the figure are very similar.

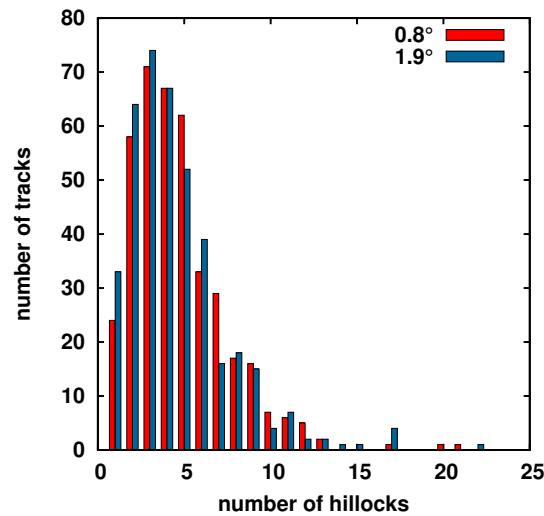


Figure 3.12: The histogram shows the number of tracks as a function of the number of hillocks. In total 400 tracks were analysed.

- The spacing s between two neighbored hillocks is defined as shown before for SrTiO₃ (page 33). That leads to:
 $s_{0.7^\circ} = 28.77 \text{ nm} \pm 7.01 \text{ nm}$
 $s_{1.9^\circ} = 28.87 \text{ nm} \pm 9.10 \text{ nm}$

Length and angular distribution

For the evaluation of the length and angular distribution of TiO₂ nanostructures, 400 tracks were analysed in the same way as described before for SrTiO₃ on page 34. In Figure 3.13 the length distribution and in Figure 3.14 the angular distribution of the two TiO₂ samples is plotted. Although the different incidence angles the fit of the hillock chain length is the same for both targets. Nevertheless the total lengths show the expected behaviour, the larger angle corresponds to the shorter length and vice versa. The angular distribution is closely the same for the short length and the long length. The fits of the shorter length are a little broader. Similar to SrTiO₃ all distributions are asymmetric.

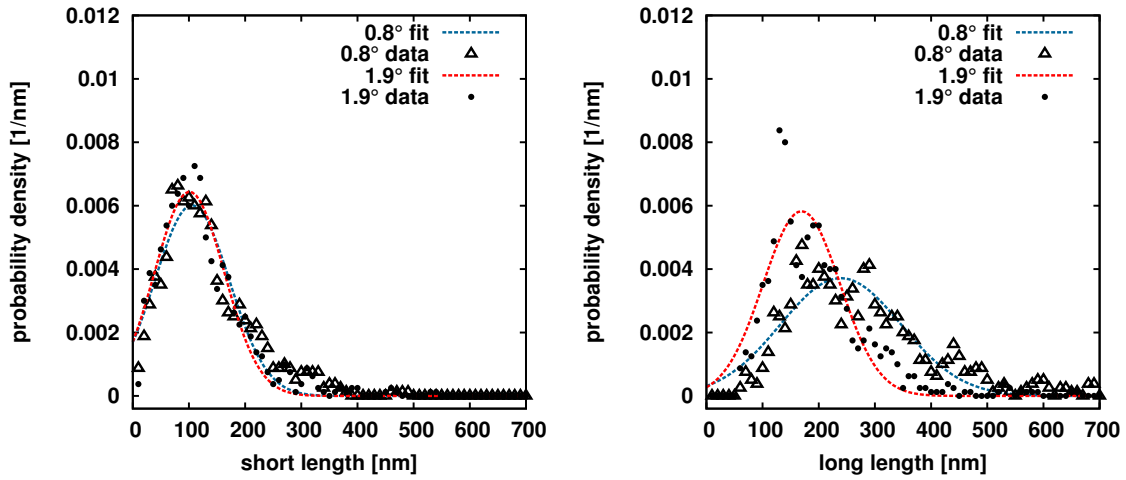


Figure 3.13: Length distribution of ion tracks on TiO₂, left: short length, right: long length (for definition see [Figure 3.3](#)).

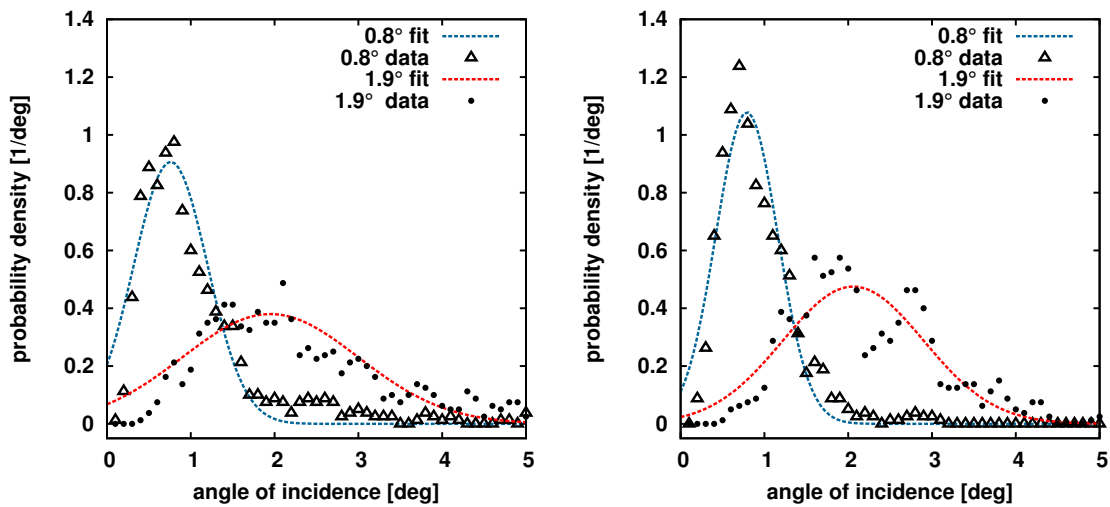


Figure 3.14: Angular distribution of ion tracks on TiO₂, left: short length, right: long length (for definition see [Figure 3.3](#)).

3.1.7 Discussion

The surface topology after swift heavy ion irradiation of both observed materials (SrTiO₃ and TiO₂) shows chains of single hillock formation as previously described in [Chapter 1.5](#). Our high resolution AFM images show additional features. In the case of SrTiO₃ a groove could be observed at the impact site of the projectile ion, a kind of

structure that was just recently reported by [101] for this material. Hillock chains on SrTiO₃ and TiO₂ surfaces are followed by a single protrusion with decaying height. In comparison to earlier studies the length of the ion tracks and the dimensions of the hillocks are smaller.

Up to now the already known nanostructures on SrTiO₃ and TiO₂ were presented. In the following section the more complex ones of CaF₂ and mica will be introduced.

3.2 Experimental results II - CaF₂ and mica

3.2.1 CaF₂

First results of CaF₂ nanostructures under glancing angles have been reported in [63]. Therein chains of single hillocks were observed. Due to better AFM images we could observe a more complex structure, which will be described in more detail in the following. Systematic measurements have been performed at different incidence angles between 0.3° and 2.1°. CaF₂ targets have been irradiated at room temperature and at 400 °C.

After the first measurement period a growing of adsorbate islands with time could be observed on the samples [99]. Heating the platelets up to 400 °C before irradiation might be a useful tool to avoid this kind of surface modification (the process of island growing on our samples is described in [Chapter 2.3.3](#)). In the second measurement period heated CaF₂ samples and untreated CaF₂ samples have been irradiated under the same conditions. In the following the pretreated targets will be analysed as well as all the targets which were heated to 400 °C during the irradiation. The evaluation of the untreated ones and of all the samples of earlier measurements will be reported in [99].

3.2.2 CaF₂ - Topography

The topography of a CaF₂ surface after irradiation with SHI under grazing angles is shown in [Figure 3.15](#). Each single ion induces a groove of several 100 nm length with a depth in the nm range, which is bordered on both sides by a chain of equally spaced hillocks. These two chains are in the following named double track. Some of the nanodots reach heights up to 4 nm. The double tracks end in one or more huge single hillocks with heights of more than 10 nm. The last part of the modification can be described as a long single decaying protrusion, with a length of several 100 nm, where single nanodots are not visible any-more.

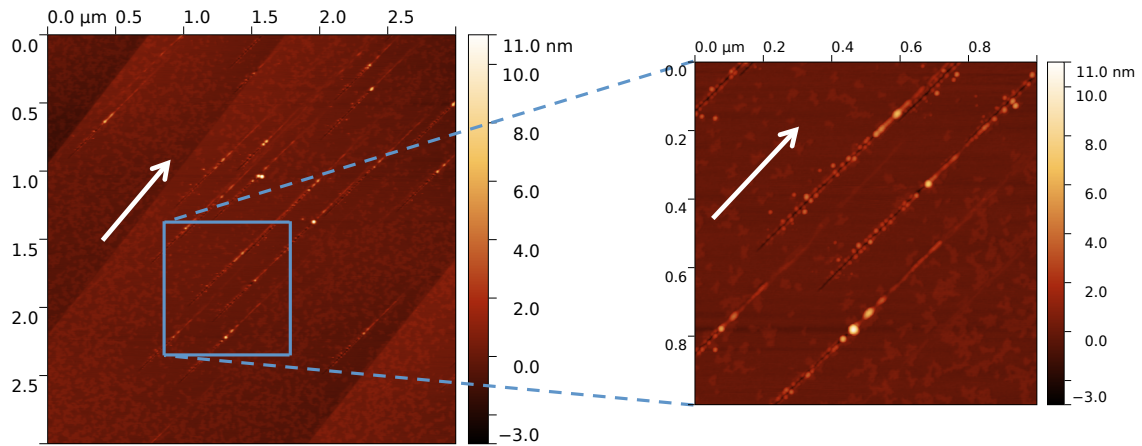


Figure 3.15: AFM images of a CaF₂ target irradiated with Xe ions @ 95 MeV under an incidence angle of 0.7°. The target was heated to 400 °C during irradiation. The white arrow marks the projectile direction. In the right zoomed image the groove and double tracks are shown.

3.2.3 CaF₂ - Analysis of the nanostructure

Length

In the analysis of CaF₂ two different lengths are distinguished. The short one l_S is the length of the double track, measured from the beginning of the groove to the first single hillock. The complete length of the track is described by the long length l_L . [Figure 3.16](#) shows the lengths highlighted on an AFM image. Height profiles of the nanostructures are plotted in [Figure 3.17](#).

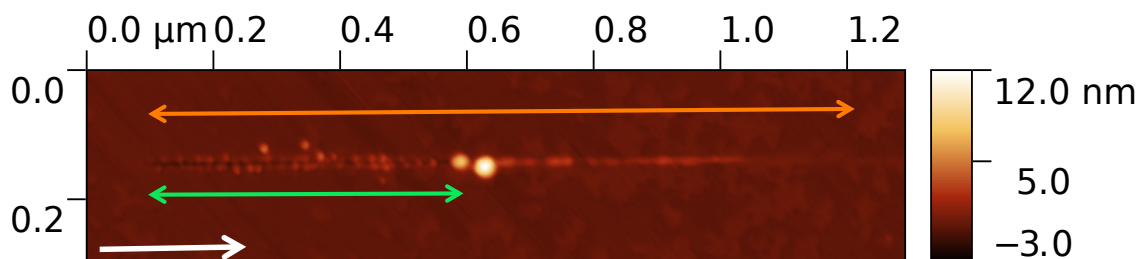


Figure 3.16: Definition of the short length (green arrow) and long length (orange arrow). The white arrow highlights the ion direction.

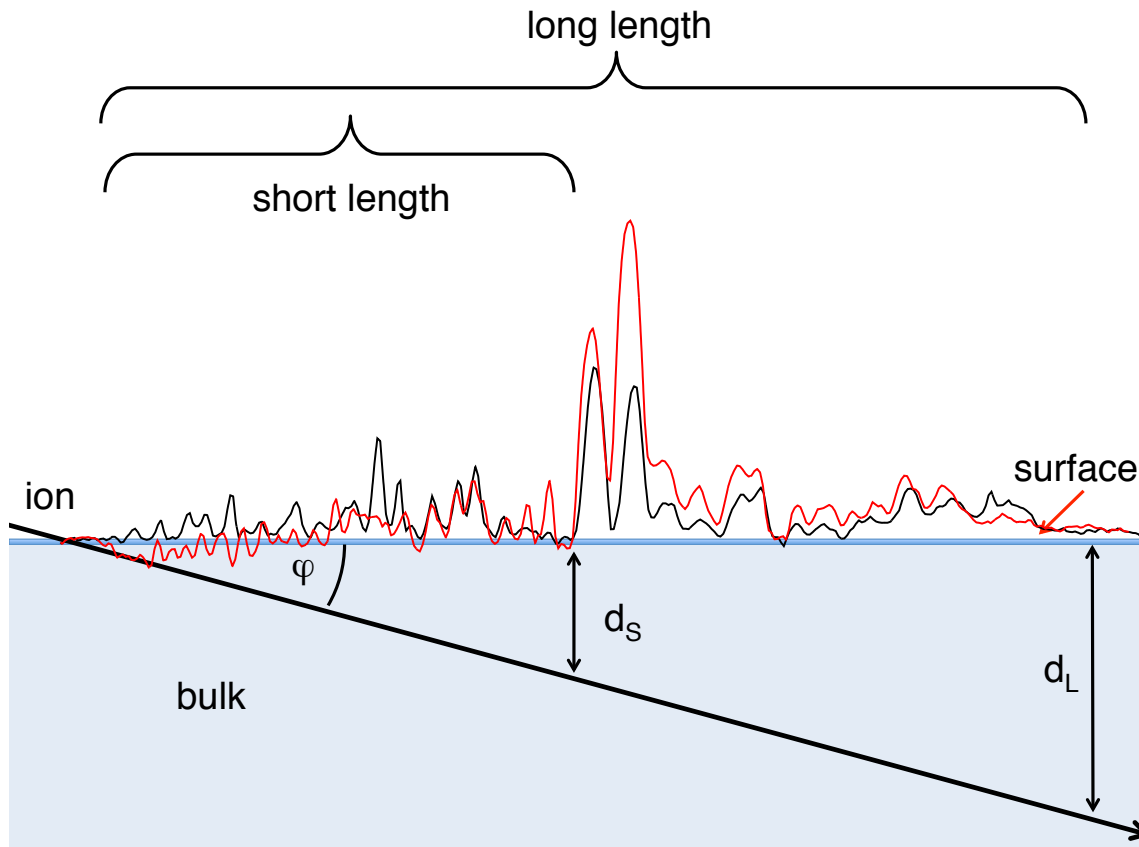


Figure 3.17: Height profiles of an $1.1 \mu\text{m}$ long ion track (an AFM image of the used nanostructure is shown in Figure 3.16). The red profile, which is a longitudinal slice through the center of the track, shows the formation of a groove with a depth of $\sim 2 \text{ nm}$, followed by two huge hillocks and a single fading protrusion. The second profile (black) is shifted from the center to a chain of the double track (the upper one of the track in Figure 3.16) and is presenting a series of single hillocks bordering the groove.

Both lengths are plotted as a function of the incidence angle in Figure 3.18. The dashed lines represent the $d_{S,L}/\tan(\varphi)$ fits as presented before for SrTiO_3 and TiO_2 . The property d_S represents the depth the projectile ion reached during the creation of the double track, d_L is the maximal depth from which an ion induced surface modification can still be observed (details see Figure 3.17). The fit finally leads to a short depth of $d_S = 4.6 \text{ nm}$ and a long one of $d_L = 11.5 \text{ nm}$. Additionally the lengths of the untreated targets (see [99]) are included.

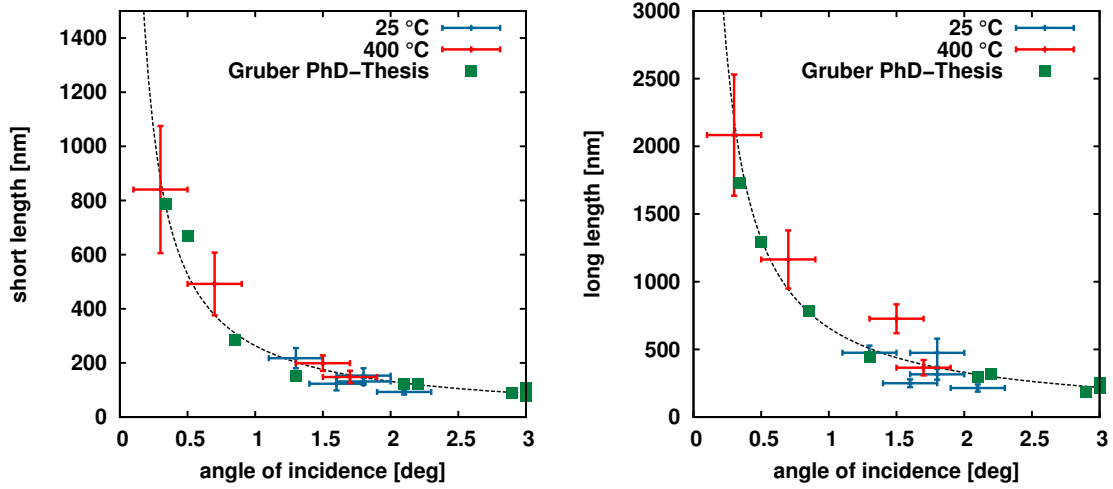


Figure 3.18: In the left image the short length of CaF_2 is plotted over the incidence angle, in the right one the complete length is shown. In both plots blue data points represent irradiations under room temperature conditions, red targets are heated to $400\text{ }^\circ\text{C}$ during irradiation. The dashed lines are the $d_{S,L}/\tan(\varphi)$ fits. Green points represent earlier measurements of our group, performed by E. Gruber [99].

Double tracks

For a characterisation of the double tracks four parameters are analysed. Due to imaging problems the full analysis could not be performed for all investigated targets.

- The first one is the height, describing the height of the tallest hillock of the double track. Typical values are $\approx 2\text{ nm}$. The calculated heights are collected in Figure 3.19 (left). Here the heights of all analysed samples irradiated under room temperature conditions are compared with the ones heated to $400\text{ }^\circ\text{C}$ during irradiation. In the investigated range of the irradiation angle, no dependence on the angle or the target temperature could be observed.
- The average distance of the hillocks in a chain of the double track is described by the property hillock spacing. The data points show roughly constant values (see Figure 3.19 right). The mean spacing has been calculated as $\approx 17\text{ nm}$, independent of irradiation temperature and angle.

In comparison with earlier studies performed on SrTiO_3 an $a/\tan(\varphi)$ dependence should be observed with a being the lattice constant of the target material [63]. All investigated targets irradiated under grazing angles of more than 1° with respect to the surface plane stay in good agreement with that fit. For

smaller angles the observed spacing is smaller than the fit suspects. In our CaF_2 paper (see publication list) the behaviour of the untreated samples is presented.

- Furthermore the distance between the two chains of the double track has been analysed. This property is roughly constant along the complete track. Similar to the properties above no dependence on the irradiation temperature and angle is observable (see the left plot in Figure 3.20). The mean value of the chain distance (13.9 nm) is in the range of the hillock spacing (17 nm, as mentioned above).
- The last point of the double track characterisation is the analysis of the groove depth. Irradiation under heated conditions leads to deeper grooves up to 2.6 nm. The deepest value for groove formation for irradiation at room temperature was found to be 1.4 nm. In this analysis high discrepancies between the different targets were observed, but no dependence on the irradiation parameters (sample temperature and angle of incidence) could be identified (see Figure 3.20 right).

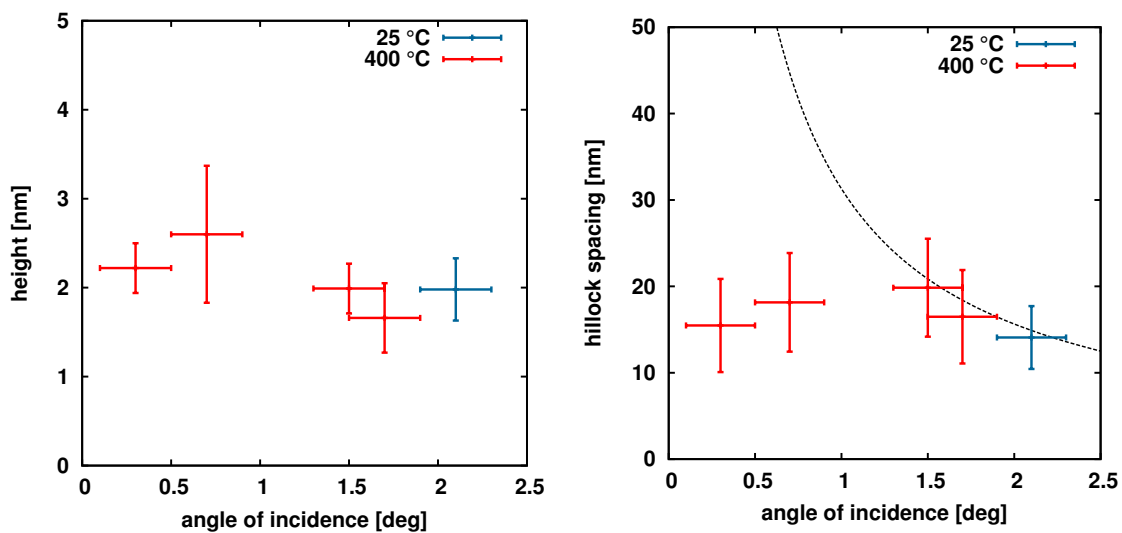


Figure 3.19: The height of the tallest hillock (left) and the average spacing between the nanodots of a chain of the double track (right) are plotted over the incidence angle. In both plots blue data points represent irradiations under room temperature conditions and red targets were heated to 400 °C during irradiation. The dashed line in the right plot is the $a/\tan(\varphi)$ fit with $a = 0.55$ nm being the lattice constant of CaF_2 .

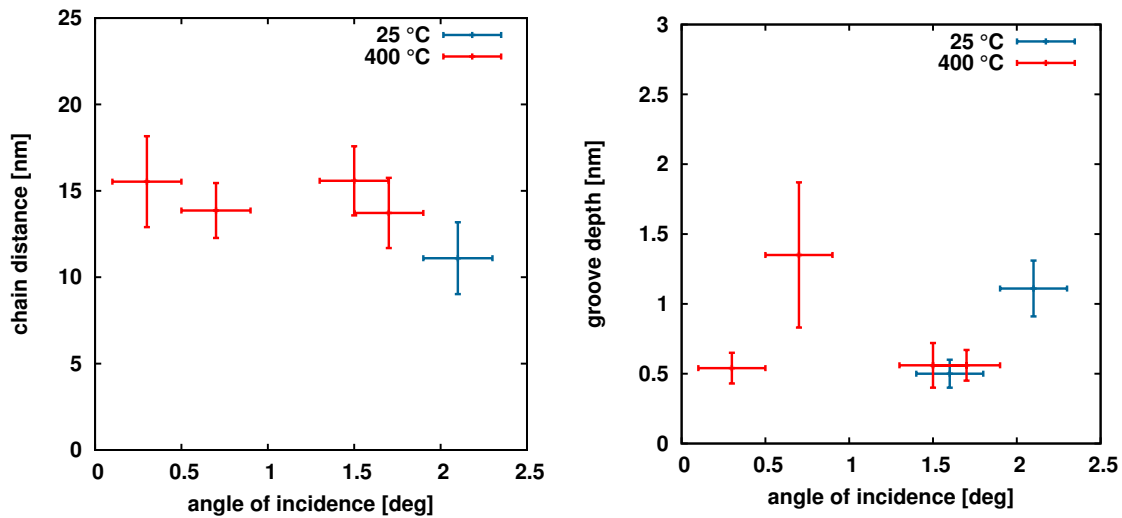


Figure 3.20: The distance between the two chains of the double track (left) and the depth of the groove between the double tracks (right) is plotted over the incidence angle. In both plots blue data points represent irradiations under room temperature conditions and red at 400 °C during irradiation.

Single hillocks

The most impressive part of the CaF_2 track is formed by a single huge hillock at the end of the groove. The maximum height of different targets was analysed and plotted over the angle of incidence in Figure 3.21. Heights up to 14 nm were observed, but since an independence of the irradiation temperature and the angle of the incoming ions could be identified, the angular uncertainties are neglected in the plot. The average height of such hillocks was determined to ~ 8.5 nm.

3.2.4 Mica

As introduced in Chapter 1.5.4 mica is a very prominent material that has been used for a lot of irradiation studies. However systematic studies under grazing incidence are still missing. So our targets of muscovite mica have been irradiated under glancing angles between 0.2° and 2.7° .

The influence of ion energy and target temperature is investigated in this section. As projectile ions different Xe isotopes and ^{208}Pb were used at kinetic energies between 23 MeV and 100 MeV. The targets have been heated to 200 °C and 400 °C, respectively, during irradiation with 100 MeV ^{208}Pb ions. Furthermore fluorphlogopite mica has been irradiated to investigate the differences between the two minerals (see page 66).

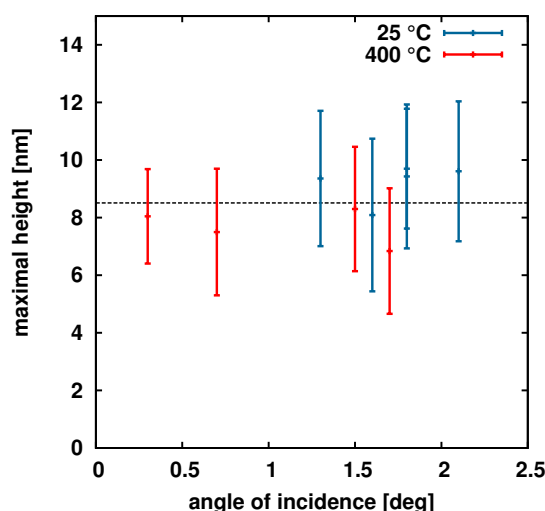


Figure 3.21: The maximum height of CaF_2 tracks single hillocks plotted over the incidence angle. Blue data points represent irradiations under room temperature conditions and red at $400\text{ }^\circ\text{C}$. The dashed line shows the average value of 8.5 nm .

3.2.5 Mica - Topography

The topography of mica after irradiation with SHI is presented in [Figure 3.22](#). The AFM image at the left side shows the creation of parallel arranged tracks with lengths of a few μm . First the height of the nanostructure is increasing then a long fading part is following. A more detailed AFM image (see [Figure 3.22](#) right) resolves the first part of the track, to be consisting of two parallel protrusions with an increasing height that merge into a single track in the region around the maximum height of the surface modification. The area between these two chains of the double track is partially below the level of the surface plane (see the height profiles shown in [Figure 3.23](#)), similar to the groove structure of CaF_2 . Typical lengths of the double track are several 100 nm .

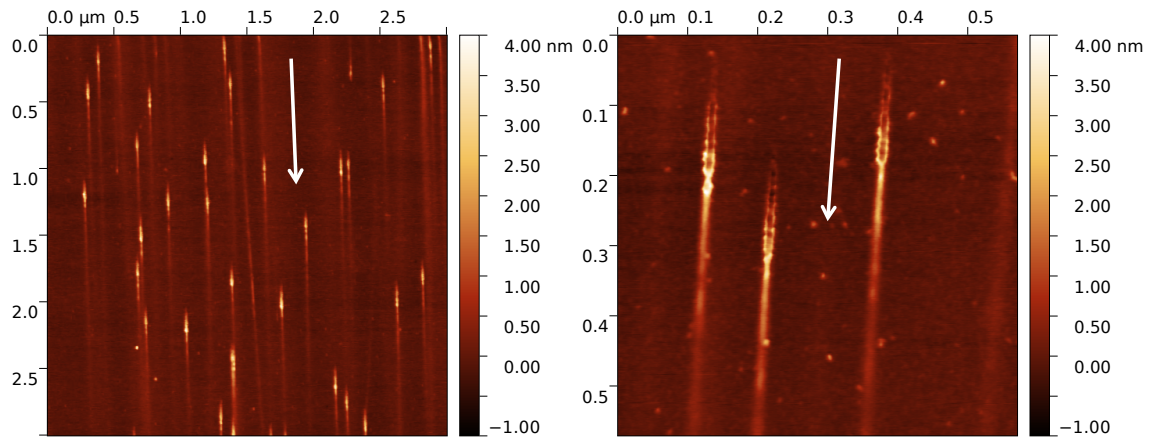


Figure 3.22: AFM images of mica irradiated with Xe ions @ 92 MeV under an angle of 1.0°. The white arrows mark the projectile direction. In the right zoomed AFM image the double track structure can nicely be seen.

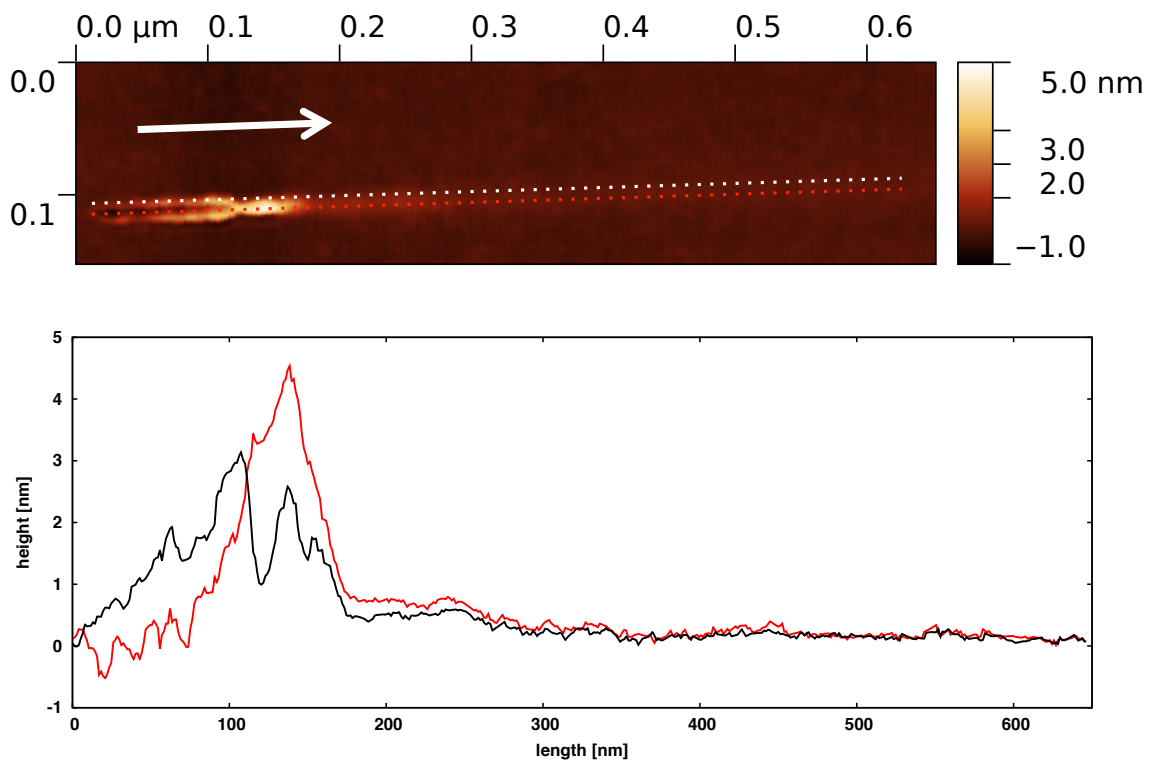


Figure 3.23: Two slices through a mica track (induced by Pb ions @ 100 MeV under an incidence angle of 2.0°, target was heated to 400 °C during irradiation) along the projectile direction are drawn to show the height development of the nanostructure. In the AFM image on top the two slice positions are marked. The red profile represents the slice between the chains of the double track and the black line (white line in the AFM image) shows the development of a double track chain. The white arrow represents again the projectile direction.

3.2.6 Mica - Analysis of the nanostructure

Length

In the case of mica again two different lengths are investigated, defined similar as done for CaF_2 . The short length l_S represents the length of the double track, the long one l_L contains the length of the complete surface modification. The two lengths are sketched on an AFM image in [Figure 3.24](#).

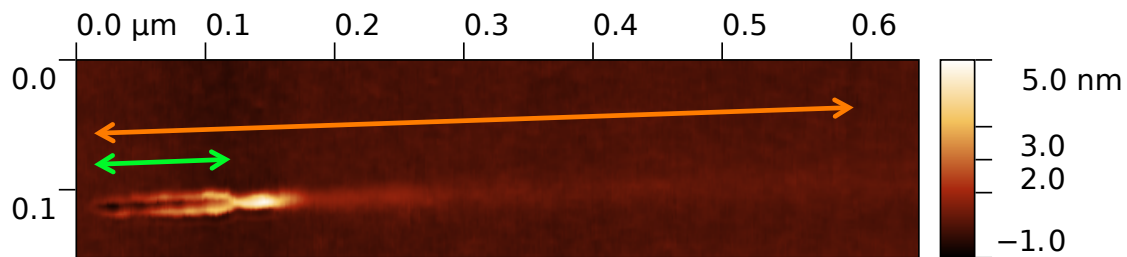


Figure 3.24: Definition of the short length l_S (green arrow) and long length l_L (orange arrow), projectile direction is from left to right.

In [Figure 3.25](#) the short and long lengths obtained for various irradiation energies are plotted over the angle of incidence. Both lengths show, like for the other investigated materials, the $1/\tan(\varphi)$ behaviour. The fit through the 92 MeV data points leads to a short depth of $d_S = 2.8 \text{ nm}$ and a long one of $d_L = 16.4 \text{ nm}$. For definition of d_S and d_L see [Figure 3.17](#).

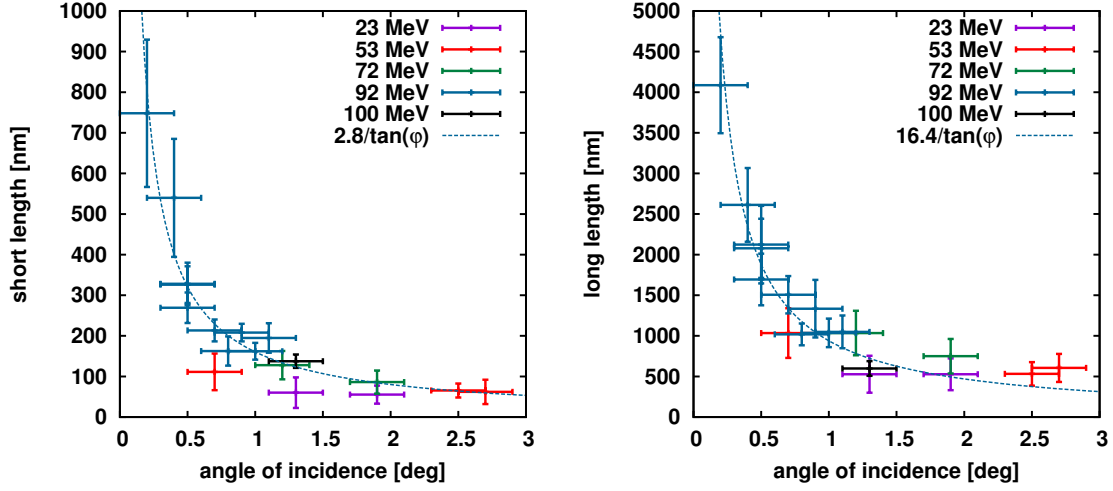


Figure 3.25: Lengths of mica tracks plotted over the incidence angle, different energies correspond to different color. Left the short tracks, right the long ones. Blue dashed line represents the $d/\tan(\varphi)$ fit with $d_S = 2.8$ nm and $d_L = 16.4$ nm, respectively.

While the 23 MeV, 53 MeV and 72 MeV length lay below the fit, the 100 MeV target is above the fit (see Figure 3.25 left). So it is possible that the length of the double tracks depends on the projectile energy. Since the number of observed tracks is quite small, further investigations are necessary. The long mica lengths do not show this behaviour (see Figure 3.25 right). Here the highest energy is close to the smallest one and e.g. the 72 MeV lengths are explicitly longer.

To investigate the energy loss dependency of the track lengths each single short and long length has been multiplied with a factor⁵ $\tan(\varphi_c)/\tan(1^\circ)$ to move the length along the $d/\tan(\varphi)$ fit, where φ_c is the calculated incidence angle of each sample. Now the lengths are rescaled to an incidence angle of 1° . So the mean values and standard deviations of all lengths have been calculated for the different energies. A constant number of tracks per target have been analysed, so that each sample influences the analysis the same.

Simulations of swift heavy ion induced defect creation on silicon carbide (SiC) surfaces performed by Ochedowski *et al.* [14] show that the length of the resulting

⁵For a constant depth d follows out of

$$d = l_1 \cdot \tan(1^\circ) = l_c \cdot \tan(\varphi_c), \quad (3.9)$$

that

$$l_1 = l_c \cdot \tan(\varphi_c)/\tan(1^\circ). \quad (3.10)$$

nanostructure (here a long ditch without a tail of material) is at a constant irradiation angle increasing with the projectile energy. These simulations have been done for an incidence angle $\varphi = 1.9^\circ$. So these lengths were multiplied with a factor $\tan(1.9^\circ)/\tan(1^\circ)$ to compare them with the present investigations of mica. The ditch structure of SiC is quite similar to the grooves between the mica double tracks.

In [Figure 3.26](#) the simulations of Ochedowski are compared with the measurements of mica tracks. In the simulations a threshold of ~ 7 keV/nm has been found. For mucovite mica the threshold is 4.8 keV/nm for normal incidence irradiation [81]. The short lengths of mica are roughly half as long as the SiC simulated ones. For both properties the energy loss dependence is roughly the same. Above a certain threshold the lengths are increasing with the energy loss. Therefore the mica short lengths were fitted with the function

$$f(S) = a \cdot \sqrt{S - S_{th}}, \quad (3.11)$$

where S represents stopping power and S_{th} the threshold of this property for nanostructure creation. The factor a is necessary for the stretching. From the fit the parameter a can be determined to $a = 50.64 \text{ nm}^{3/2} \text{ keV}^{-1/2}$ and the threshold $S_{th} = 4.6 \text{ keV/nm}$ that is close under the Thibaudau value of 4.8 keV/nm [81]. This behaviour of lower threshold values under grazing angles has also been reported by Karlusić [46] for SrTiO₃ (see also [Chapter 1.5.1](#)). The simulation in [Figure 3.26](#) has been fitted with the same function, but since the threshold value is here included, only the property a has been fitted as $a = 92.41 \text{ nm}^{3/2} \text{ keV}^{-1/2}$. A possible reason for this behaviour is that for double track creation more energy is necessary than for the further nanostructure creation. For CaF₂ track diameters were also fitted with the square root of the stopping power [73].

The energy loss dependence of the complete lengths is shown in [Figure 3.27](#). Here no systematics can be seen. All long lengths are in the same range. The SRIM code [55] simulates additionally to the energy loss the ion range in the target material. For mica the projected range is 4.8 μm for ¹²⁹Xe ions @ 23 MeV, which is much longer than the measured length. So an energy dependence would be surprising. Otherwise the track diameter of mica is increasing with the ions energy loss [83], inducing a longer visible track in the used irradiation geometry.

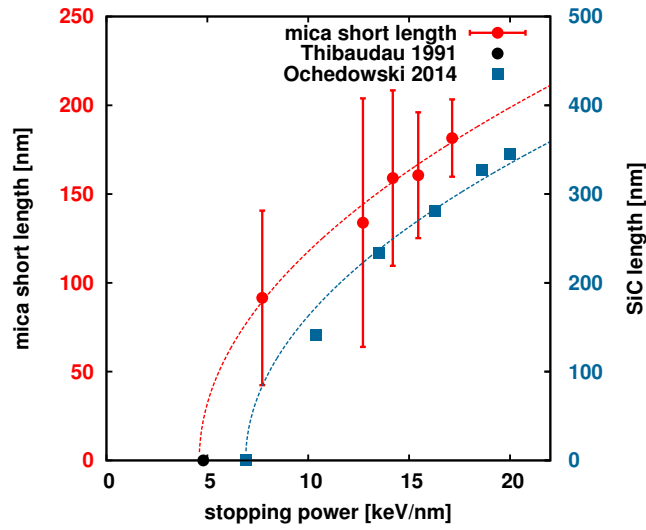


Figure 3.26: Short lengths of muscovite mica plotted over the energy loss. Blue data points represent simulations of silicon carbide performed by Orchedowski *et al.* [14]. The incidence angle of measured and simulated lengths is shifted to 1°, the black mica threshold is taken from Thibaudau [81], dashed lines represent fits (see text above). Mind the different y-axes.

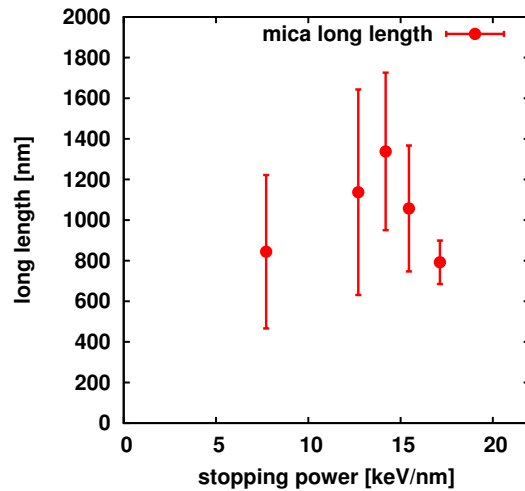


Figure 3.27: Long lengths of mica plotted over energy loss. The lengths are given for an incidence angle $\varphi = 1^\circ$.

Double tracks

The double tracks are the first part of the surface modification of mica. Their height is increasing along the length of the track (see Figure 3.23). Cuts perpendicular to the

projectile ion direction through this nanostructure show typically a non-symmetric behaviour of the two tracks (see e.g. the height profile in [Figure 3.30](#)). A 3d plot of the double tracks describing the structure is shown in [Figure 3.28](#). The double tracks are more than 3 nm high.

Some targets show an additional effect, namely non continuous double tracks, where the two chains are partially recombined to a single track. This type of double track is only visible under the smallest angles of the investigated range e.g. the nanostructures of the 0.4° sample are combined for several times (see the right AFM image in [Figure 3.29](#)).

For a good description of the double track structure four characteristic parameters are evaluated. Between 10 and 25 tracks per angle and projectile energy have been analysed to calculate mean values and their uncertainties.

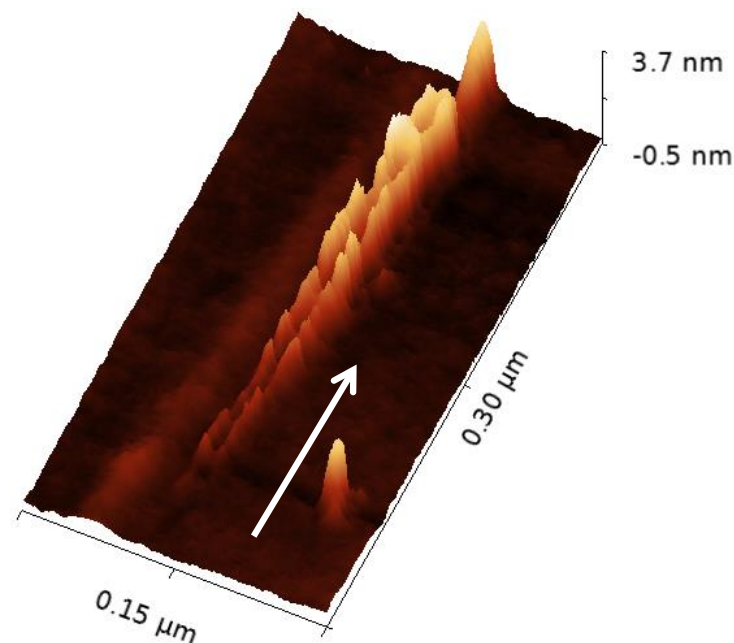


Figure 3.28: A 3d plot of the mica double track. The projectile ion (Xe @ 95 MeV, incidence angle 0.9°) is injected from the bottom left of the image (white arrow).

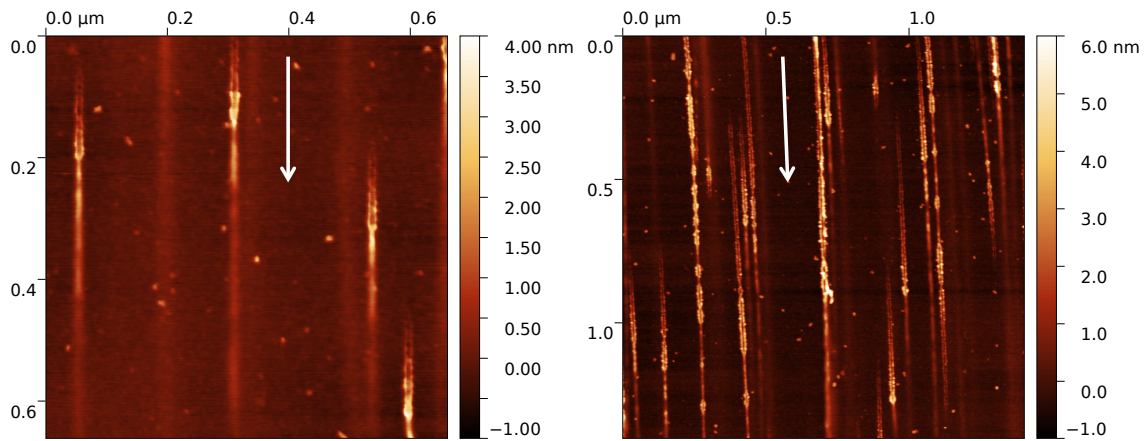


Figure 3.29: Comparison of mica double tracks consisting of one continuous double track in the left (incidence angle 1.0°) and with more sections (right, incidence angle 0.4°). In both AFM images the ion direction is indicated by the white arrow.

- The maximum average height of the two double tracks is described by the property h , calculated as the average of h_1 and h_2 , where h_1 is the height of the left track without background of the profile and h_2 the right one. A typical profile of a double track including the different heights (h_1 and h_2) is shown in [Figure 3.30a](#).

In [Figure 3.31](#) the calculated heights are summarised. Here one can see that this property is independent of the irradiation angle. So the angle uncertainties are neglected in this and the following plots. The dashed lines show the fitted mean values for each projectile energy, which depend on the ion's energy loss. A larger energy loss corresponds to a larger height (see also [Figure 3.32](#)). Therefore the average of all tracks heights, independent of the incidence angle of each energy has been calculated.

- The horizontal distance between the maxima of the tracks height is described by the parameter d . Although this property is (instead of h) independent of the position of the slice through the track, the values were taken from the same position. So d is constant along the complete double track.

The angle independence of d is shown in [Figure 3.31](#). Similar to the height the distance between the two chains is increasing with the stopping power. The energy loss behaviour of this parameter is plotted in [Figure 3.32](#) together with the height's one.

- The third parameter is the average width w of the double tracks hillocks, given

by $w = (w_1 + w_2)/2$, where w_1 represents the width of the left and w_2 of the right track. Again the same slice position with the maximum height h is analysed. Following [Figure 3.30b](#) each w is defined as the full width of tracks minimum. For the calculation two times the distance between the maximum and the outer minimum was used.

The data is plotted in [Figure 3.33](#) (left). Here the uncertainties are too large to give a representative statement of the energy loss dependence. Nevertheless the width is independent of the angle of incidence. Maybe tip convolution effects influence the analysis of this parameter, so that the measured width is wider than in reality (see [Figure 3.33](#) right).

- As the fourth property of the double tracks the maximum depth of the groove has been investigated. In the case of muscovite mica this analysis is very complex, because of the low depth, that is in most tracks less than 0.3 nm. So a very high quality of AFM images is necessary for that evaluation. Not all images fulfil the resolution to measure that property, so that in the following only tracks with an doubtless identifiable groove have been analysed. That requirements even made the evaluation of a complete sample (^{129}Xe ions @ 55 MeV, $\varphi = 1^\circ$) impossible. A further problem is that the surface roughness is also in a range of 0.1 nm, what makes it difficult to distinguish the ion induced grooves from ordinary surfaces. So a slice through the clearly identifiable part of the double track is done and then moved perpendicular to the ion direction to the starting point of the interaction. Only if there is a groove in the position between the tracks the modification is ion induced, otherwise it is just an ordinary surface unevenness. In the case of mica-OH the groove is not a real ditch for all tracks, sometimes the immersion is just a dot like pit.

In [Figure 3.34](#) (left) the data is collected for the different projectile energies. One can see the maximum depth is approximately 0.1 nm below the level of the surface plane for all investigated energies and incidence angles. Here the only exception is the sample irradiated with ^{208}Pb ions. This one shows grooves that are in average twice as deep as on all other samples. That target is further the only one where all immersions are clearly identifiable as ditches.

The maximal measurable groove depth is limited by the tip target geometry. In reality the tips have an entire small radius, so that the tip is possibly thicker than the distance between the chains (see [Figure 3.34](#) right).

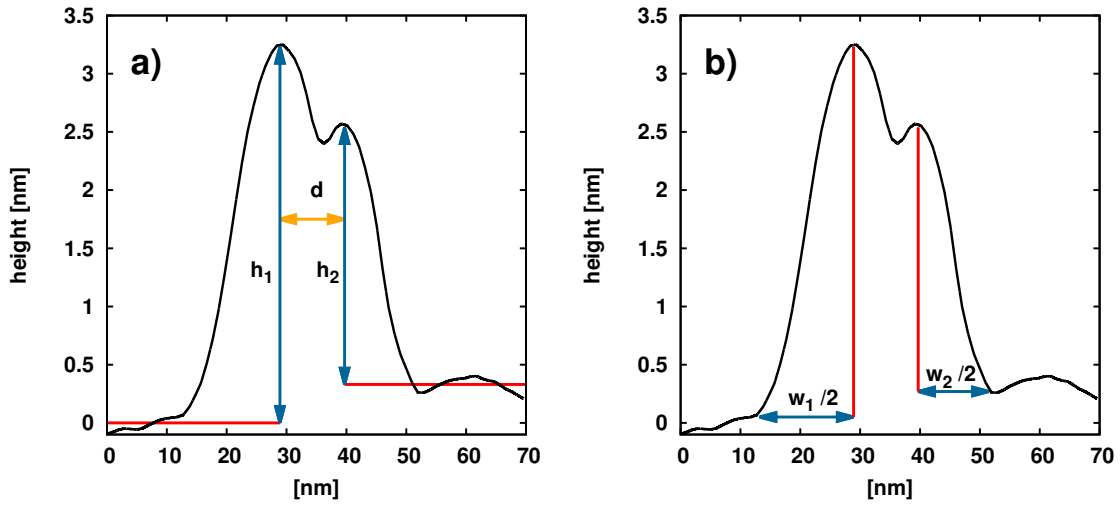


Figure 3.30: Definition of the double track properties height h as the average of h_1 and h_2 , distance d in (a) and width w in (b). In the left picture the red horizontal lines represent the background.

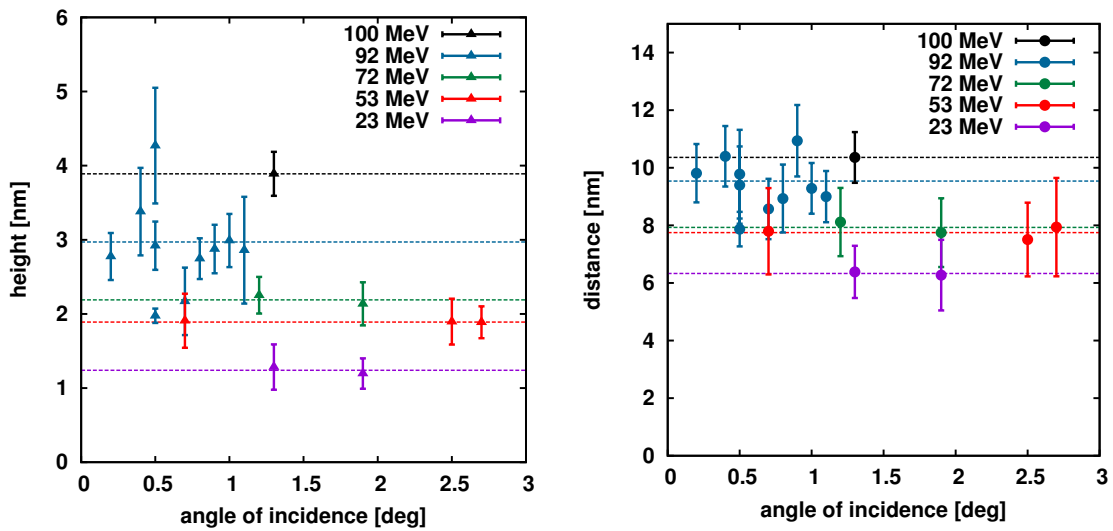


Figure 3.31: Mica double track height h in the left and the distance d between the tracks (right) plotted over the irradiation angle. The dashed lines represent the mean value of the various ion energies.

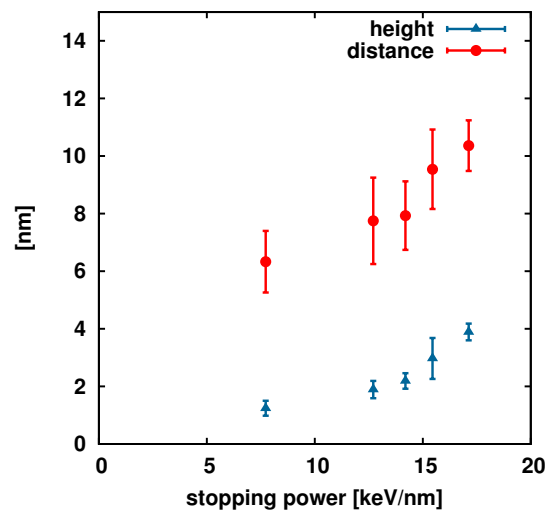


Figure 3.32: Energy loss dependence of the double track parameters height h and distance d .

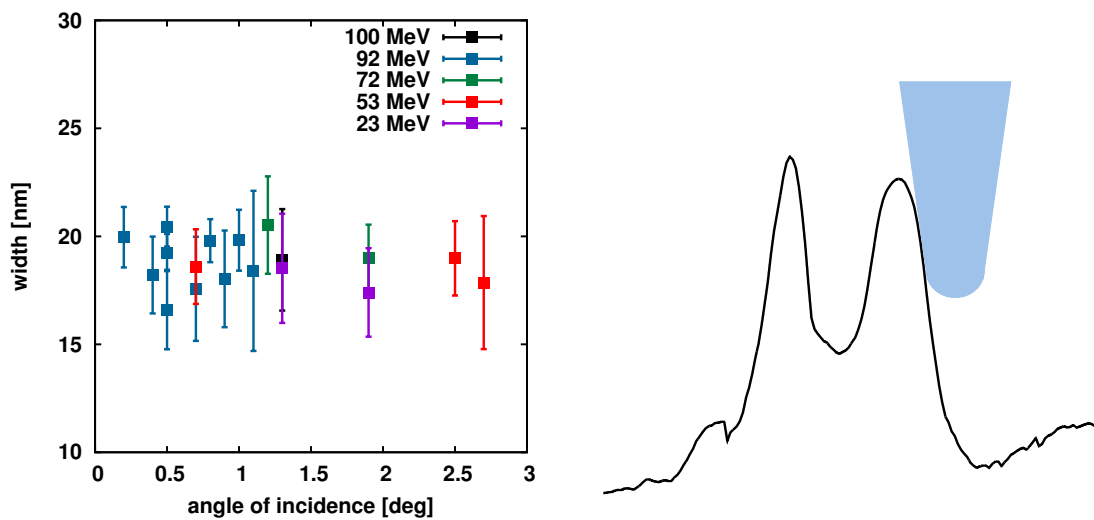


Figure 3.33: The width w of the double tracks plotted over the incidence angle in the left and a sketch of tip artefacts in the right.

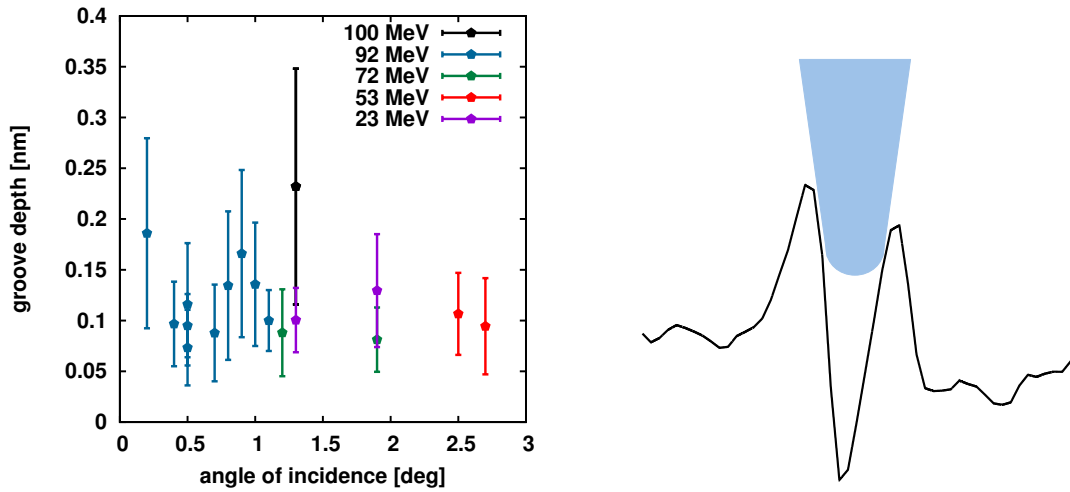


Figure 3.34: The groove depths between the double tracks plotted over the angle of incidence in the left and a sketch of tip artefacts in the right.

Maximal height of the tracks

In the area where the two chains of the double track join together to a single one the nanostructure shows its maximal height H_{max} (see e.g. the AFM images in [Figure 3.22](#)). Similar to the double tracks height h the total height is angle independent, but increased with the energy loss (see [Figure 3.35](#)). Typically H_{max} is roughly 1.4 times larger than the height of the double tracks. [Table 3.1](#) summarises this relation for various ion energies.

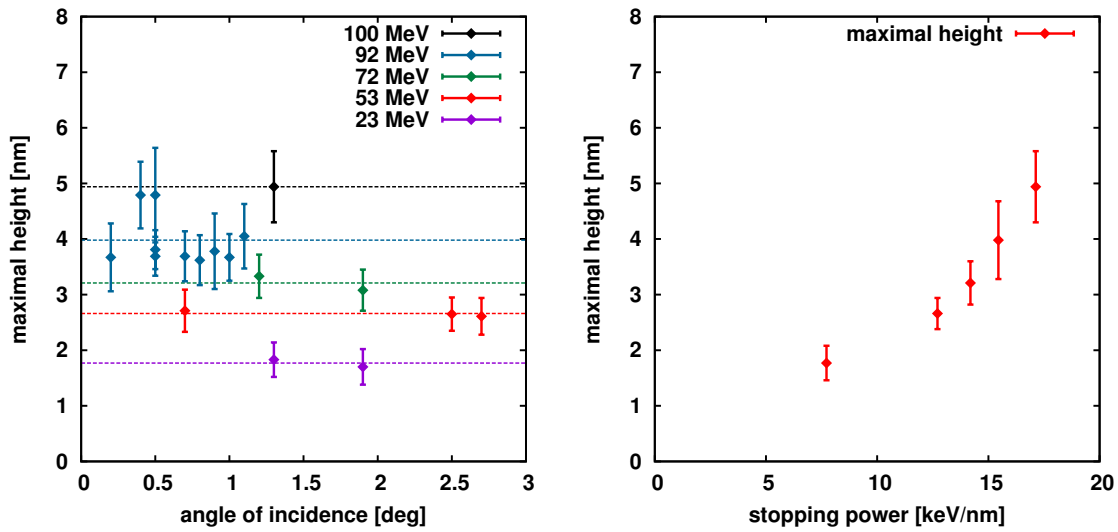


Figure 3.35: left: the maximum of the track height is plotted over the angle of incidence. The dashed lines represent the average values of the different energies; right: the energy loss dependence of the same property is evaluated.

Table 3.1: The relation maximal height/double track height calculated for the different ion energies.

energy	H_{max}/h
23 MeV	1.43 ± 0.19
53 MeV	1.41 ± 0.11
72 MeV	1.47 ± 0.12
92 MeV	1.34 ± 0.06
100 MeV	1.27 ± 0.16

Temperature dependence

Mica platelets have been heated up to 200 °C and 400 °C during the irradiation with ^{208}Pb ions at a kinetic energy of 100 MeV. The nominal irradiation angle is 2° for both targets, the calculated angles are $\varphi_{200^\circ\text{C}} = 1.8^\circ$ and $\varphi_{400^\circ\text{C}} = 2.0^\circ$, respectively. Here again the self-constructed heater [88] has been used. As previously shown, mica surface nanostructures are energy loss dependent, so that these two heated targets are only comparable with the third one irradiated with the same ions under room temperature conditions. A dehydroxylation process is starting at 650 °C that modifies the mica structure so that a weight loss is induced [102]. So higher temperatures are not possible without starting a structural modification.

Lengths

The lengths of the heated targets have been investigated in the same way as for all other mica samples irradiated under room temperature conditions. In the plots (see [Figure 3.36](#)) 92 MeV targets are shown additionally to 100 MeV ones to provide a better comparability with the $1/\tan(\varphi)$ proportionality.

For short and long lengths the values of the heated samples lie above the $d/\tan(\varphi)$ fit of the 92 MeV irradiations. The 200 °C sample shows the longest short lengths of the three 100 MeV targets and the hottest one the shortest. But here the different irradiation angles have not been taken into account, otherwise each length must get multiplied with a factor $\tan(\varphi)/\tan(1^\circ)$ to rescale them along the $d/\tan(\varphi)$ fit to an angle of 1° (see [page 50](#)). In the case of the long length the room temperature target has the shortest length although the shorter incidence angle should induce the longest lengths.

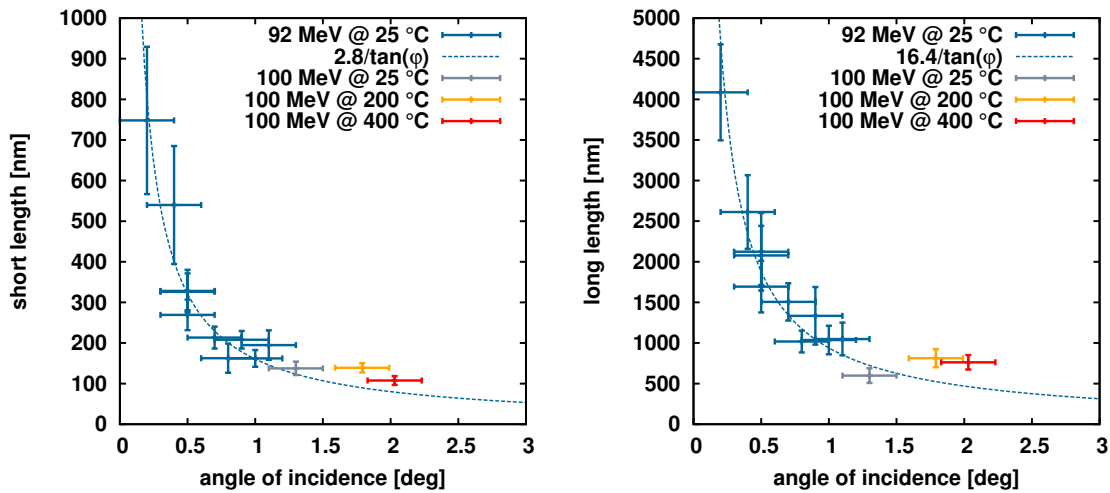


Figure 3.36: Short (left) and long lengths (right) of heated mica in comparison to irradiation under room temperature.

Double tracks

The three parameters h , d and w are analysed in [Figure 3.37](#) in the same way as described before for the room temperature targets (see [page 52](#)). Here one can see the temperature independence of the width, as well as a similar behaviour between heights and distances. Since the measurement uncertainties and that there is only one irradiated sample per temperature further statements of the temperature dependence of these three properties are not possible.

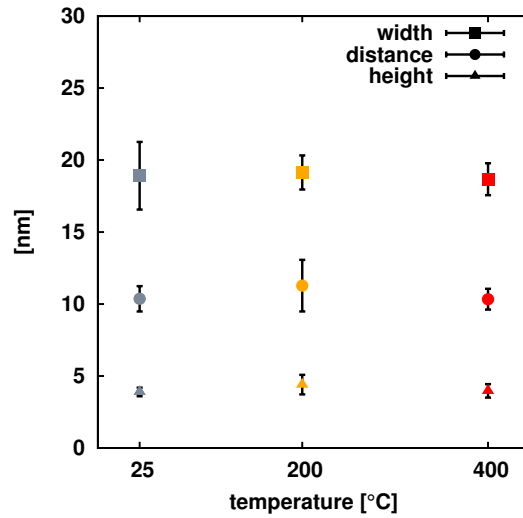


Figure 3.37: Temperature dependence of mica double track properties h , d and w . Only the three samples irradiated with 100 MeV Pb ions are shown.

The most interesting difference of the heated samples is the modification of the groove nanostructure at higher temperatures. As shown in [Figure 3.38](#) the ditch structure between the double tracks depends on the surface temperature. At lower kinetic energies the grooves are only partially real ditches, otherwise dotlike immersions can be observed. The target irradiated at room temperature with 100 MeV ions (highest energy loss of all) shows in all tracks a real ditch doubtless. Our 200 °C sample shows a structure similar to the behaviour of the one irradiated at room temperature. At a surface temperature of 400 °C all tracks have a much deeper ditch, which is now up to 1.5 nm below the level of the surface plane.

All previous analysis of the double tracks shows angle independence, so the depth of the grooves are compared in [Table 3.2](#). Summarised, the ditch is getting deeper with a higher target temperature. Here again the heating temperature is limited by the target properties [102].

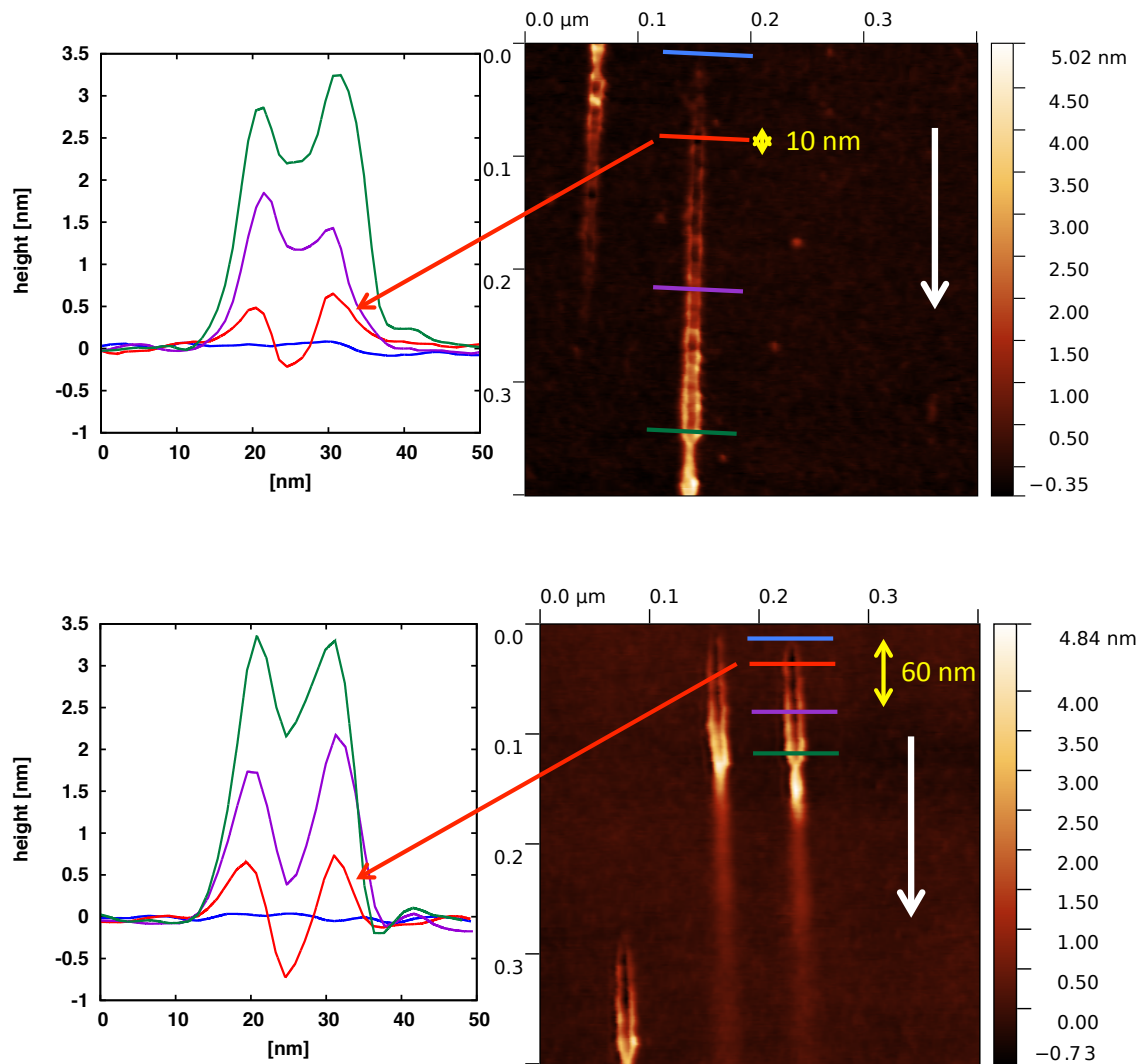


Figure 3.38: Comparison of different types of mica grooves: on top a track under 0.5° irradiation angle (room temperature) is analysed, the lower case represents the 400°C target (irradiation angle 2.0°). For both targets four profiles show the various formation of the double track. The first (blue) slice represents the natural surface (the height level of the surface plane), the second one (red) the position with the deepest ditch and the last two profiles show the further development of the surface modification. The most significant difference between these nanostructures is the depth and especially the relative length of the groove, which is symbolised by the yellow arrow. On the room temperature sample the ditch below the level of the surface plane is much shorter although the complete track is much longer than the one of the heated target. White arrows indicate the projectile direction.

Table 3.2: Analysis of the depth of the groove (ditch) between the double tracks of mica irradiated at different target temperatures with Pb ions at 100 MeV.

temperature	angle	groove depth
25 °C	1.3°	0.23 nm ± 0.12 nm
200 °C	1.8°	0.24 nm ± 0.16 nm
400 °C	2.0°	0.63 nm ± 0.35 nm

The maximum height H_{max} of the tracks of all the three 100 MeV targets is compared in [Table 3.3](#). Further the relation H_{max}/h is summarised in this table. Noticeable differences between the various target temperatures are not identifiable. The values of this relation are in the range of all room temperature targets irradiated at different projectile energies (compare with [Table 3.1](#)).

Table 3.3: Analysis of the maximal height of mica tracks irradiated at different target temperatures with Pb ions at 100 MeV.

temperature	H_{max}	H_{max}/h
25 °C	4.94 nm ± 0.64 nm	1.27 ± 0.16
200 °C	5.25 nm ± 0.67 nm	1.19 ± 0.15
400 °C	4.90 nm ± 0.54 nm	1.23 ± 0.14

Length and angular distribution

For the calculation of the length and angular distribution (used algorithm introduced for SrTiO₃ on [page 34](#)) 400 long and 150 short track lengths have been analysed. [Figure 3.39](#) shows the results of two mica targets irradiated under different kinetic energies and angles (1.0° @ 92 MeV and 1.9° @ 23 MeV) for the distribution of the short and long lengths.

The data of the short lengths fits better with the shape because the smaller number of necessary intervals (therefore more tracks are in each of the slots), although the asymmetry is still visible.

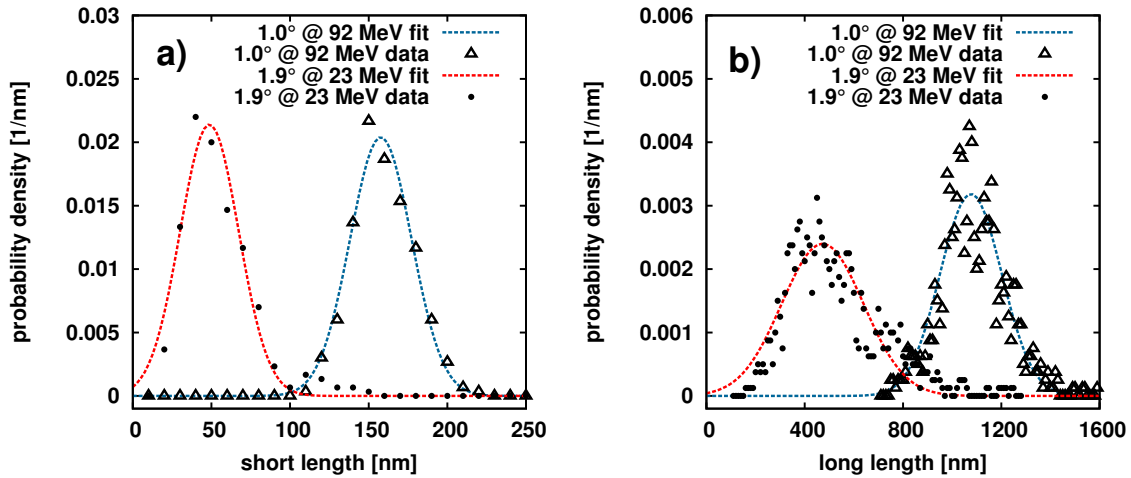


Figure 3.39: The length distribution of two targets is shown, the short length in a) and the long ones of the same targets in b).

The angular distributions of the mica targets fit better with the Gaussian shape, but here again the symmetry is not perfectly given, as shown in Figure 3.40 (to provide a good comparability, the same targets of the previous figure are analysed).

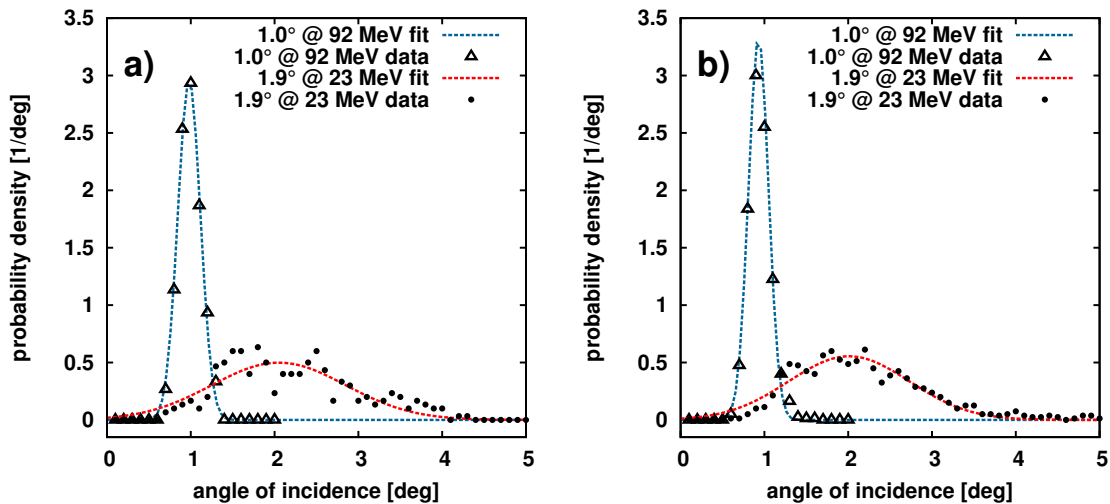


Figure 3.40: For two samples the angular distribution has been performed and compared with a Gaussian curve. In a) the short lengths and in b) the long lengths are the starting point of the analysis.

In the length distribution (Figure 3.39) both compared targets show a similar width of the Gaussian fit. Now for the angles the discrepancies between the two investigated

targets are larger, but for each target the distribution of the long length is similar to the corresponding short one (see Figure 3.40). Both lengths of the 92 MeV target are fitted by the Gaussian curve very well, for the 23 MeV the data of the long distribution show smaller discrepancies from the fit, presumably because of the larger number of evaluated tracks.

A systematic in the widening (σ_φ) of the ion beam is identifiable, σ_φ , that is also the standard value of the Gaussian shape, is a function of the irradiation angle and the beam energy. It is important that not the energy itself but the scattering effects in the degrader foil (see Chapter 2.1) influences the tracks. In Figure 3.41 (left) the influence of three different beam energies at a constant incidence angle is compared. The degrader foil widens the beam, so that the sample with the highest energy (no degrader) has the smallest σ_φ and the decelerated 23 MeV target shows a larger widening. Figure 3.41 (right) shows the dependence on the irradiation angle. For both energies the target with the larger incidence angle shows a larger σ_φ . To summarise, the widening is increasing with the thickness of the degrader foil and the irradiation angle.

Using this method of angular uncertainty analysis makes it possible to calculate the standard value of the irradiation angle for each single target.

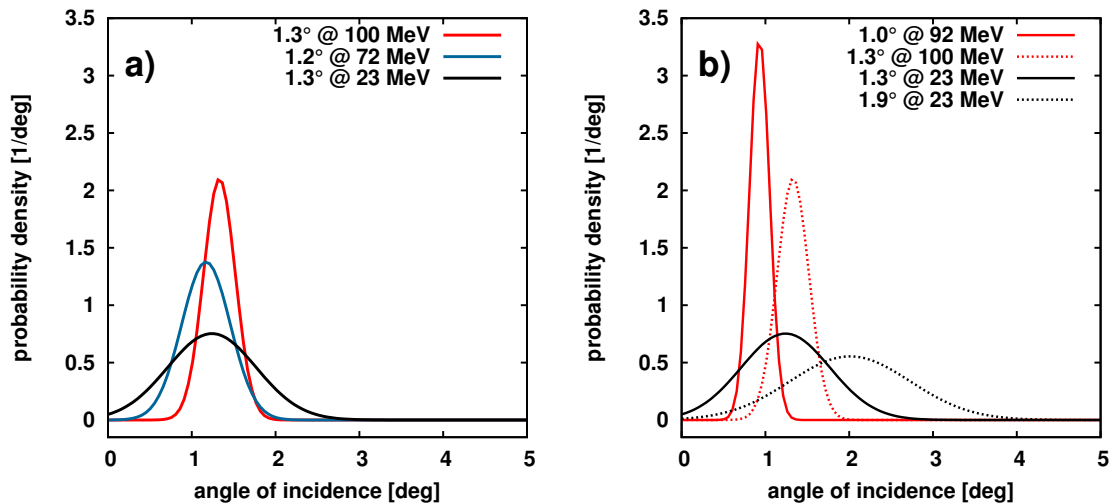


Figure 3.41: Comparison of Gaussian fits of different targets, in a) the influence of the degrader foil at a constant angle of incidence is shown, in b) two angles of incidence with (black) and without degrader (red) are compared. In both cases the target with the larger incidence angle (dashed lines) shows the larger standard deviation.

Fluorphlogopite mica

All the results previously shown in this section are from investigations of muscovite mica (mica-OH). Now the nanostructures of three irradiated fluorphlogopite mica (mica-F) targets (all irradiated with 92 MeV Xe under incidence angles between 0.2° and 1.4°) are analysed and compared with the mica-OH surface modifications. Therefore lengths and double tracks of this material are evaluated in the same way.

A comparison of AFM images presenting the different surface topography of the different mica types is shown in Figure 3.42. On both materials parallel arranged tracks are identified. The induced surface modification is similar, but with some differences. Both nanostructures show the formation of a double track bordering a groove at the impact site of the ion, which is ending in a long fading protrusion. The first visible difference between the nanostructures of the two micas are the well-marked grooves of the mica-F tracks. Here a long ditch is the first modification of the surface followed by the double track that is not as notable as the one of the mica-OH tracks. Maybe this is also the reason for the longer groove formation. Similar to the previous mica results the double track joins later to a single track and a long decaying protrusion is the last part of the ion-induced structure.

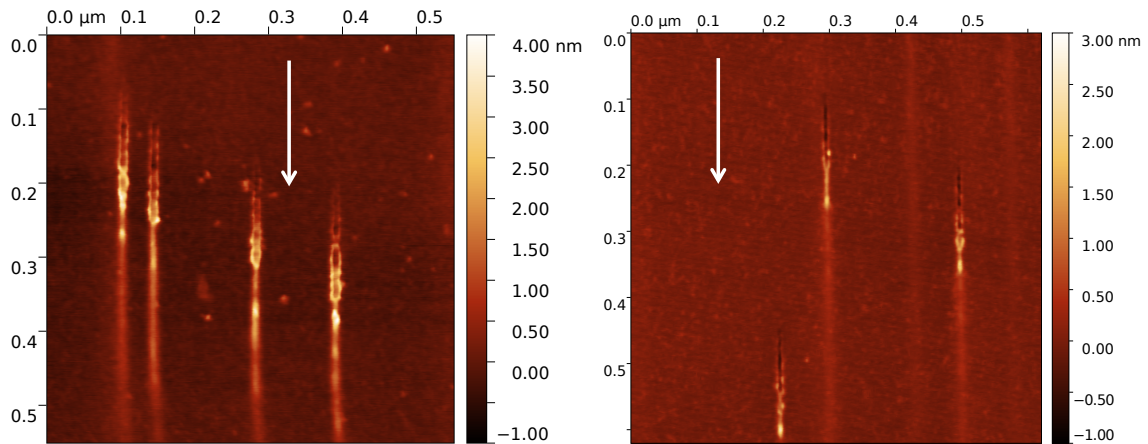


Figure 3.42: Comparison of AFM images of mica-OH (left, irradiation angle 1.0°) and mica-F (right, irradiation angle 1.4°). Both targets are irradiated with ^{129}Xe ions @ 92 MeV. White arrows indicate the projectile direction.

Furthermore the span of mica-F tracks has been investigated. Again the short length l_S represents the distance between the first visible modification (ditch) and the end of the double track, whereas the long one l_L is the complete length of the nanostructure. In the case of the short lengths there is no clear difference between the two micas. All three data points are in the range of the mica-OH $d_S/\tan(\varphi)$ -fit. The

long lengths show a discrepancy, two targets are much longer than the fit suspects, the third one lies close to the fit. In Figure 3.43 all short and long lengths of both micas (irradiated with 92 MeV ions) are plotted and compared.

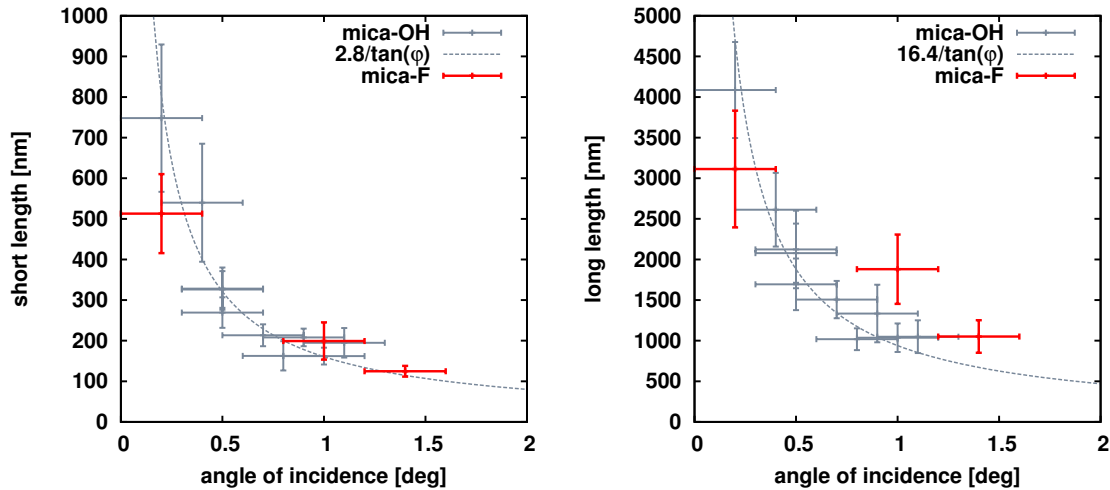


Figure 3.43: Short and long lengths of the three mica-F samples (red) plotted over the incidence angle in comparison to mica-OH targets irradiated under the same conditions.

Mica-F double tracks consist typically of two chains of single hillocks with irregular distances between two neighbored nanodots. Some other double tracks have the same behaviour like mica-OH, where each chain looks like overlapping hillocks. The first nanodot appears much later in the modification, because of the long ditch before. The double tracks are analysed in the same way as the mica-OH targets (page 52). In Figure 3.44 the evaluation of the parameters h , d and w is presented as well as the groove depth. All these properties are independent of the irradiation angle. The height of the double tracks is with an average value of 0.89 nm roughly one third of 92 MeV mica-OH (2.97 nm), the distance between the two chains is also smaller, but the width is in the same range. On mica-F surfaces the groove is better visible, because of the longer and especially deeper (0.36 nm to \approx 0.1 nm) shaping.

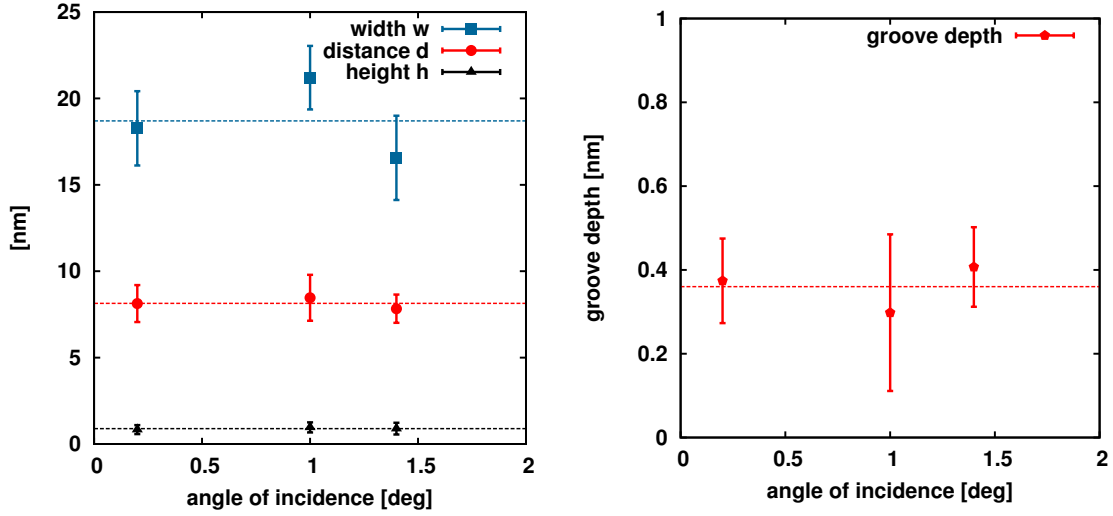


Figure 3.44: Analysis of mica-F double track properties h , d and w in the left and of the groove depth in the right.

The last point of the evaluation was the analysis of the maximum height H_{max} of the surface modification. Similar to the double track height h the maximum height of mica-F tracks (1.7 nm) is approximately 2.3 times smaller than the mica-OH value (3.98 nm). This leads finally to $H_{max}/h = 1.92 \pm 0.20$ in comparison to 1.34 ± 0.06 in the case of the 92 MeV mica-OH tracks.

Additionally the volume of two arbitrary clearly visible ditches has been calculated. One of the 1.0° sample and the second of the 1.4° one. For the calculation 17 and 18 equidistant slices through the ditch perpendicular to the ion direction have been performed to calculate the cross sectional area at each slice position. The area is approached by a triangle (see the sketch in Figure 3.45). Slice 1 is the impact site of the ion, so that the area of this position $A_1 = 0$, the area at the last slice is $A_N = 0$ as well with N being the number of slices. The volume between two positions i and $i + 1$ is approximated by a truncated pyramid (Figure 3.45) and can be calculated by using⁶ [103]

$$V_i = \frac{\Delta h}{3} \cdot (A_i + \sqrt{A_i \cdot A_{i+1}} + A_{i+1}) \quad (3.12)$$

with Δh as the distance between two neighboured slice positions, that is calculated as

$$\Delta h = \frac{l_D}{N - 1} \quad (3.13)$$

with l_D being the length of the investigated ditch and A_i the area at position i . The

⁶The formula assumes that all triangles are similar to each other. This condition is neglected.

total volume V of the ditch is now the sum of all V_i with $i = 1, 2, \dots, N - 1$ and has been calculated as 223 nm^3 for 1.0° sample and as 119 nm^3 for the 1.4° one. Further analysis of the two ditches is summarised in [Table 3.4](#).

Table 3.4: Analysis of two ditches of mica-F. \bar{A} represents the average cross sectional area of the ditch ($\bar{A} = V/l_D$).

angle	1.0°	1.4°
N	17	18
l_D	235 nm	108 nm
Δh	13.8 nm	6 nm
V	223 nm^3	119 nm^3
\bar{A}	1.05 nm^2	1.14 nm^2

In the next step the number of sputtered atoms has been estimated. The particle density n_{at} has been taken from simulations with the SRIM code [55] of mica-F as $n_{at} \approx 9 \cdot 10^{22} \text{ atoms/cm}^3 = 90 \text{ atoms/nm}^3$. The number of atoms sputtered out of the material resulting the ditch is calculated as $N_{at} = V \cdot n_{at}$.

- Track 1.0° : $N_{at} = 223 \text{ nm}^3 \cdot 90 \text{ atoms/nm}^3 \approx 20000 \text{ atoms}$, this corresponds with $\sim 90 \text{ atoms per nm ditch length}$.
- Track 1.4° : $N_{at} = 119 \text{ nm}^3 \cdot 90 \text{ atoms/nm}^3 \approx 10000 \text{ atoms}$, this corresponds again with $\sim 90 \text{ atoms per nm ditch length}$.

Both ditches show approximately the same number of sputtered atoms per nm track, which is possible induced because of the same energy loss.

To confirm if the energy loss of the projectile ion is large enough to cut the bonding of the atoms the following estimation has been performed. The SRIM calculated stopping power of the used Xe ions is 15.3 keV/nm (see [Table 2.3](#)). Dividing this value by the number of sputtered atoms per nm, which is approximately 90 atoms/nm as estimated above leads to a binding energy of $\approx 170 \text{ eV}$. This is far above typical values for chemical bonds (see [104]), so that $90 \text{ sputtered atom per nm groove length}$ seem to be a possible value.

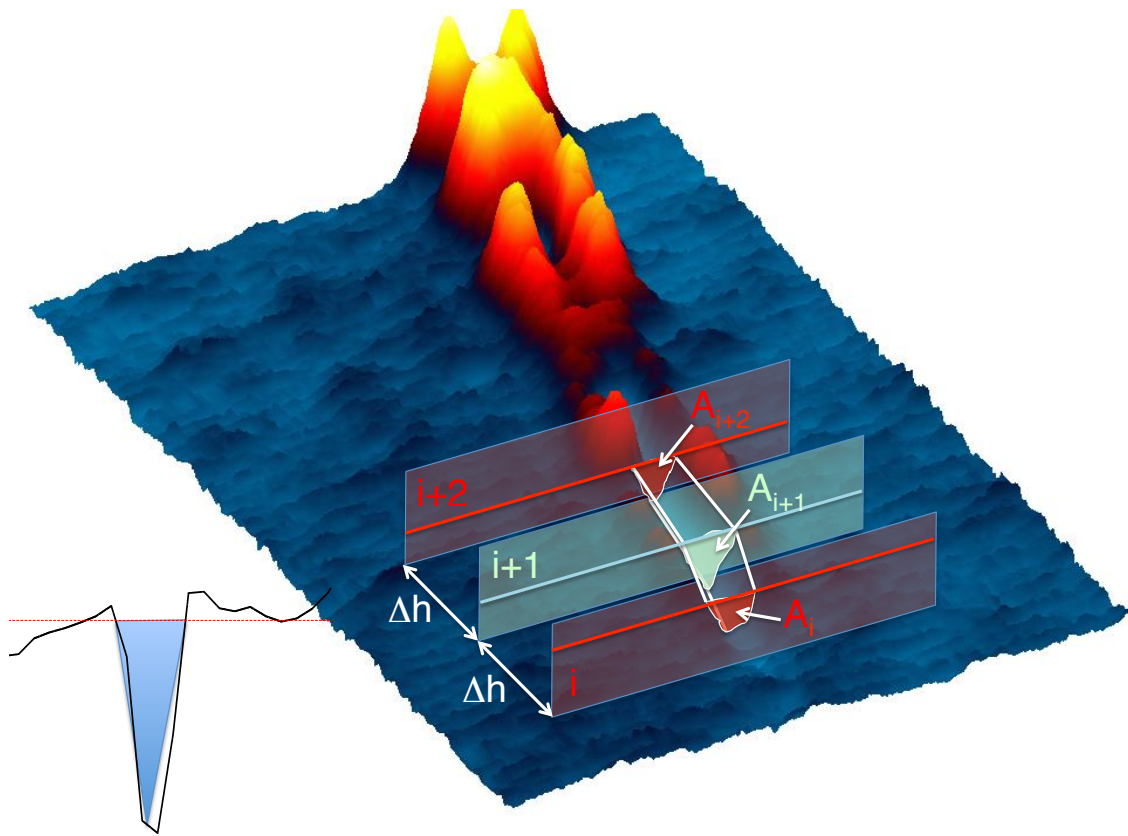


Figure 3.45: 3d plot of the ditch structure of a mica-F track. Here three slice positions (i , $i + 1$ and $i + 2$) are sketched, including their areas. The horizontal lines represent the surface level at different slice positions. In the left corner the approximation of the area as a triangle is sketched.

3.2.7 Discussion

The track structure of CaF_2 and mica described in this section differs from the materials presented in the first part of this Chapter (SrTiO_3 and TiO_2). AFM images show the creation of a groove bordered by two parallel chains of target material along the direction of the projectile ion, which are in the following named double tracks. Later these two tracks merge to a single decaying protrusion.

To find a model describing the creation of the double tracks, simulations basing on a three dimensional version of the thermal spike model have been performed in collaboration with Universität Duisburg-Essen. A first manuscript concluding these ideas for CaF_2 has recently been submitted to *New Journal of Physics*. The following ideas are taken from this paper. By comparing the data of CaF_2 with the simulations one can see that the length of the track is in agreement with the area where the projectile energy loss heats the target material above its melting temperature. The

measured lengths of the double tracks are always shorter than the simulated lengths of the surface region, where the sublimation temperature is surpassed. Nevertheless sublimation is considered responsible for the observed groove structure. Maybe the groove is partially filled with molten material again after the ion passes deeper layers of the target and the remaining groove is therefore shorter in the experiment than in the simulations (see [Figure 3.46](#)). Following these results the sublimation point must be surpassed for double track creation. The distance between the two hillock chains is in the range of the simulated width of the molten region (≈ 15 nm), which is surrounding the sublimated area and visible on the AFM images as the two chains bordering the groove.

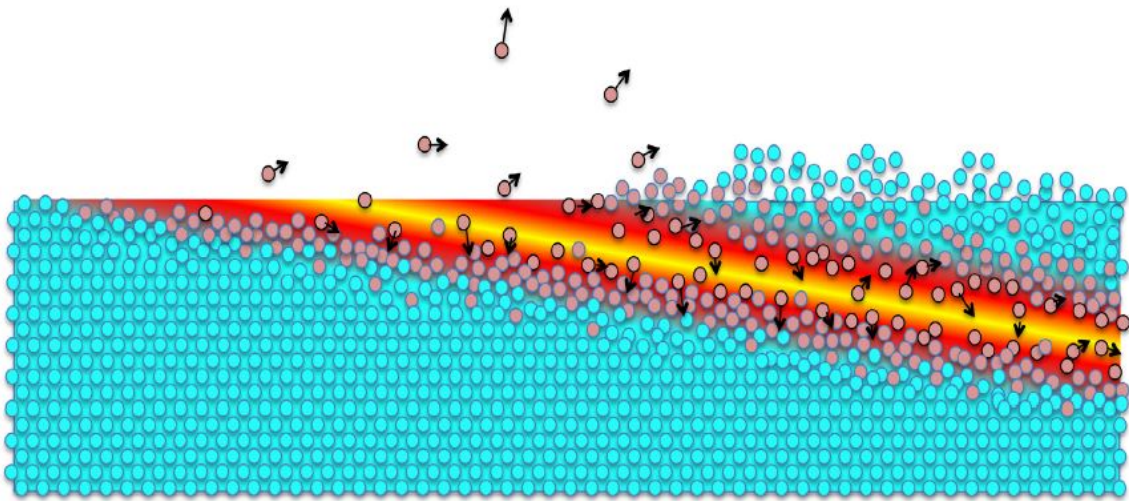


Figure 3.46: Illustration of the irradiation process.

The double tracks of CaF_2 consist of a series of equally spaced hillocks, which can be connected to the electronic structure of the target material [15]. Mica shows a different kind of double track that can be interpreted as hillocks which are so close to each other that neighbored nanodots are overlapping. A possible description is the more complex electronic structure of this material in comparison to CaF_2 (see [Figures 2.10](#) and [2.6](#)).

A comparison of the sublimation temperatures of the investigated materials show that the ones of SrTiO_3 and TiO_2 are higher than the ones of CaF_2 and mica. So less energy is necessary to surpass the sublimation point of CaF_2 and mica what makes the creation of grooves possible. If this model has a global validity it should be possible to see the groove formation also on TiO_2 surfaces by increasing the energy of the incident ions. Consequently the grooves should no longer be visible on CaF_2 and mica when decreasing the energy of the incident ions below a certain value.

4 Summary and outlook

4.1 Summary

In the course of this thesis nanostructures on surfaces, induced by swift heavy ions, were observed by using high resolution atomic force microscopy (AFM). The irradiations have been performed using different projectile ions at kinetic energies between 23 MeV and 100 MeV under grazing incidence angles between 0.2° and 2° with respect to the surface plane of the target material. As target materials SrTiO_3 , TiO_2 , CaF_2 and mica were chosen. The irradiations have been performed at the IRRSUD beam line at GANIL, Caen.

The special irradiation geometry forces the formation of tracks near the surface of the target. The dimensions of such tracks are connected with the irradiation parameters (e.g. incidence angle, ions energy loss, ...). On different target materials different types of surface modification can be observed.

The first investigated materials were SrTiO_3 and TiO_2 , that were chosen as test materials for further studies. Due to the large number of studies on SrTiO_3 performed under grazing angles our results can be compared with the available data. The resulting track structure is for both materials a chain of single nanodots, the so called hillocks, with a typical height of 2 nm - 5 nm and track lengths of a few hundreds of nm, what is in agreement with earlier observations. Additionally a groove structure could be imaged on SrTiO_3 that was just recently reported [101].

A major part was the investigation of CaF_2 and mica, where a more complex track structure could be identified. The observed tracks consist of a groove of some 100 nm length at the impact site of the projectile ion, which is bordered by two walls of target material. In the case of CaF_2 these walls consist of equally spaced hillocks with typical heights of ~ 2 nm. On mica surfaces these parallel arranged chains seem to be hillocks which are overlapping with the neighbouring nanodots. Both materials show that this "double track" has an increasing height and that the two chains merge later to a single track. At CaF_2 surfaces this part of the ion track is dominated by a single hillock with a height of ~ 9 nm. A long fading protrusion is following.

For mica, tracks with a total length of some μm were observed. Extensive analysis was performed to evaluate the influence of the different irradiation parameters like incidence angles and energies on the ion tracks. Whereas the height of the tracks is

only depending on the energy loss of the projectiles, the length l is linked with the incidence angle φ by

$$l \sim 1/\tan(\varphi) \quad (4.1)$$

in agreement with [15]. The induced nanostructures of two micas (muscovite mica and fluorphlogopite mica) were investigated and compared, e.g. fluorphlogopite mica shows a deeper groove structure at the impact site.

4.2 Outlook

As mentioned in the introduction of this thesis previous studies (see the references in [Chapter 1.5](#)) show that imaging with different AFM modes can lead to different nanostructure dimensions of the track. So it would be interesting to observe the tracks of the investigated materials additionally under various conditions e.g. imaging in ultra high vacuum (UHV). Additionally different tips/ cantilevers can influence the measurement of the samples.

For mica first investigations using different projectile energies were performed. As previously shown in [Figure 2.11](#) only a small energy loss range was observed. Here irradiations could be performed at higher and lower kinetic energies to find maxima in the dimensions of the track and threshold values for nanostructure creation. In the course of this thesis kinetic energies correspond to an energy loss below the stopping power maximum, so additional studies could be performed at higher projectile energies where the same stopping power is reached (but above the stopping power maximum).

Another irradiation parameter that can be modified is the sample temperature. In [Chapter 3.2](#) CaF_2 and mica targets that have been heated to 200°C and 400°C during SHI irradiation were analysed. Simulations (e.g. ours of CaF_2) using a two temperature model, based on the thermal spike concept (introduced in [Chapter 1.3.2](#)) show that the projectile ions due to their energy loss heat a region around their path through the target material. Surface nanostructures correspond with regions where the melting temperature is reached. If the target is already heated, a smaller energy loss of the projectile ions should be necessary to surpass the temperature necessary for nanostructure creation. Heating the targets might therefore have the same effect as a higher stopping power of the projectile ions.

The groove structure that has been observed on SrTiO_3 , CaF_2 and mica was reported previously also for other materials like SiC [14], but not for TiO_2 . So this material should be investigated in more detail to give a description why groove struc-

tures of tracks are not observed on TiO_2 surfaces. Was it because of a too low AFM image quality or because these tracks do not show this modification in real or only at a higher energy deposition? Maybe using different AFM imaging modes can answer this. Following the model introduced for CaF_2 (see [Chapter 3.2.7](#)) the sublimation temperature has to be surpassed for groove creation. Possibly projectile ions with higher stopping powers or heating the targets during irradiation might be a way to form this kind of nanostructure also on the surfaces of TiO_2 .

A Irradiation Data

Table A.1: Irradiation data of SrTiO₃.

date of irradiation	ions	energy	nominal angle [°]	calculated angle [°]	dose [10 ¹⁰ ions/cm ²]
Jun 15	¹²⁹ Xe ²³⁺	53 MeV	1	0.9	2.86
Jun 15	¹²⁹ Xe ²³⁺	53 MeV	2	2.0	1.43

Table A.2: Irradiation data of TiO₂.

date of irradiation	ions	energy	nominal angle [°]	calculated angle [°]	dose [10 ¹⁰ ions/cm ²]
Jun 15	¹²⁹ Xe ²³⁺	53 MeV	1	0.8	2.86
Jun 15	¹²⁹ Xe ²³⁺	53 MeV	2	1.9	1.43

Table A.3: Irradiation data of CaF₂.

date of irradiation	ions	energy	nominal angle [°]	calculated angle [°]	dose [10 ¹⁰ ions/cm ²]
Dec 14	²⁰⁸ Pb ²⁹⁺	100 MeV	1.5	0.3	1.91 [400 °C]
Dec 14	²⁰⁸ Pb ²⁹⁺	100 MeV	1.5	1.5	1.91 [400 °C]
Apr 15	¹³⁶ Xe ²³⁺	95 MeV	0.3	1.3	5.74
Apr 15	¹³⁶ Xe ²³⁺	95 MeV	0.5	1.6	3.44
Apr 15	¹³⁶ Xe ²³⁺	95 MeV	0.7	1.8	4.09
Apr 15	¹³⁶ Xe ²³⁺	95 MeV	1	1.8	2.86
Apr 15	¹³⁶ Xe ²³⁺	95 MeV	1.5	- - -	1.91
Apr 15	¹³⁶ Xe ²³⁺	95 MeV	2	2.1	1.43
Apr 15	¹³⁶ Xe ²³⁺	95 MeV	2	0.7	1.43 [400 °C]
Apr 15	¹³⁶ Xe ²³⁺	95 MeV	2	1.7	1.43 [400 °C]

Table A.4: Irradiation data of mica-OH.

date of irradiation	ions	energy	nominal angle [°]	calculated angle [°]	dose [10 ¹⁰ ions/cm ²]
Nov 13	¹³⁶ Xe ²³⁺	95 MeV	0.2	0.4	5.73
Nov 13	¹³⁶ Xe ²³⁺	95 MeV	0.4	0.5	2.86
Nov 13	¹³⁶ Xe ²³⁺	95 MeV	0.7	0.9	4.09
Nov 13	¹³⁶ Xe ²³⁺	95 MeV	1	1.1	2.86
Oct 14	¹²⁹ Xe ²³⁺	55 MeV	1	0.7	2.86
Oct 14	¹²⁹ Xe ²³⁺	92 MeV	0.2	0.2	5.73
Oct 14	¹²⁹ Xe ²³⁺	92 MeV	0.5	0.5	2.20
Oct 14	¹²⁹ Xe ²³⁺	92 MeV	0.6	0.5	2.86
Oct 14	¹²⁹ Xe ²³⁺	92 MeV	0.9	0.7	3.18
Oct 14	¹²⁹ Xe ²³⁺	92 MeV	1.2	0.8	2.39
Oct 14	¹²⁹ Xe ²³⁺	92 MeV	1.5	1.0	1.91
Dec 14	²⁰⁸ Pb ²⁹⁺	100 MeV	2	1.3	2.29
Dec 14	²⁰⁸ Pb ²⁹⁺	100 MeV	2	1.8	2.29 [200 °C]
Dec 14	²⁰⁸ Pb ²⁹⁺	100 MeV	2	2.0	2.29 [400 °C]
Jun 15	¹²⁹ Xe ²³⁺	23 MeV	1	1.3	2.86
Jun 15	¹²⁹ Xe ²³⁺	23 MeV	2	1.9	1.43
Jun 15	¹²⁹ Xe ²³⁺	53 MeV	1	2.5	2.86
Jun 15	¹²⁹ Xe ²³⁺	53 MeV	2	2.7	1.43
Jun 15	¹²⁹ Xe ²³⁺	72 MeV	1	1.2	2.86
Jun 15	¹²⁹ Xe ²³⁺	72 MeV	2	1.9	1.43

Table A.5: Irradiation data of mica-F.

date of irradiation	ions	energy	nominal angle [°]	calculated angle [°]	dose [10 ¹⁰ ions/cm ²]
Oct 14	¹²⁹ Xe ²³⁺	92 MeV	0.2	0.2	5.73
Oct 14	¹²⁹ Xe ²³⁺	92 MeV	0.5	1.0	2.20
Oct 14	¹²⁹ Xe ²³⁺	92 MeV	1.5	1.4	1.91

List of Figures

1.1	SRIM calculated energy loss curves of electronic stopping in dependence on the penetration depth.	10
1.2	SRIM calculated energy loss curves of electronic stopping and nuclear stopping of ^{129}Xe ions in TiO_2	11
1.3	AFM image of SrTiO_3 after SHI irradiation and the length of SrTiO_3 chains plotted over the angle of incidence compared with the $9.8/\tan(\varphi)$ fit.	13
1.4	Efficiency of nanostructure creation on CaF_2 surfaces in dependence on the stopping power.	15
2.1	Pictures of the AFM.	18
2.2	The working principle of an atomic force microscope.	19
2.3	AFM images of SrTiO_3 performed in tapping mode: height image, amplitude image and phase image.	21
2.4	Crystalline structure of SrTiO_3 and AFM tapping mode image of an unirradiated sample.	22
2.5	Crystalline structure of TiO_2 and AFM tapping mode image of an unirradiated sample.	23
2.6	Crystalline structure of CaF_2 and AFM tapping mode image of an unirradiated sample.	23
2.7	AFM images of a CaF_2 surface one hour after cleaving and 28 hours after cleaving (same crystal).	24
2.8	AFM images of CaF_2 4 days after cleaving, one our after heating up to 350°C , and two weeks after heating.	24
2.9	AFM images of CaF_2 36 hours after cleaving, freshly after heating up to 250°C and one day after heating.	25
2.10	Crystalline structure of mica-OH and AFM tapping mode image of an unirradiated sample.	26
2.11	SRIM calculation of the energy loss of ^{129}Xe ions in muscovite mica.	27
2.12	SRIM energy loss calculation of different ions on mica.	27
3.1	AFM images of SrTiO_3 irradiated under a grazing angle of 2.0°	30
3.2	3d plot AFM image of SrTiO_3	30

3.3	Height profile of an irradiated SrTiO ₃ surface with a 600 nm long track, consisting of a chain of single nanodots and a shallow groove at the impact site.	31
3.4	The short and long lengths of the two 53 MeV SrTiO ₃ samples plotted over the angle of incidence.	32
3.5	The histogram shows the number of tracks as a function of the number of hillocks.	33
3.6	The average hillock spacing in dependence of the incidence angle. The data points of the 53 MeV SrTiO ₃ targets are compared with measurements by Akcöltekin <i>et al.</i> [63].	34
3.7	Length distribution of ion tracks on SrTiO ₃	35
3.8	Angular distribution of ion tracks on SrTiO ₃	36
3.9	AFM image of TiO ₂ irradiated with Xe ions @ 53 MeV ions under an angle of $\varphi = 0.75^\circ$	37
3.10	A profile of a track on TiO ₂ after irradiation with 53 MeV Xe ions. . .	37
3.11	The short and long lengths of the two 53 MeV TiO ₂ samples plotted over the angle of incidence.	38
3.12	The histogram shows the number of tracks as a function of the number of hillocks.	39
3.13	Length distribution of ion tracks on TiO ₂	40
3.14	Angular distribution of ion tracks on TiO ₂	40
3.15	AFM images of a CaF ₂ target irradiated with Xe ions @ 95 MeV under an incidence angle of 0.7°. The target was heated to 400 °C during irradiation.	42
3.16	Definition of the short length and long length.	42
3.17	Height profiles of an 1.1 μm long ion track.	43
3.18	In the left image the short length of CaF ₂ is plotted over the incidence angle, in the right one the complete length is shown.	44
3.19	The height of the tallest hillock (left) and the average spacing between the nanodots of a chain of the double track (right) are plotted over the incidence angle.	45
3.20	The distance between the two chains of the double track and the depth of the groove between the double tracks is plotted over the incidence angle.	46
3.21	The maximum height of CaF ₂ tracks single hillocks plotted over the incidence angle.	47

3.22	AFM images of mica irradiated with Xe ions @ 92 MeV under an angle of 1.0°	48
3.23	Two slices through a mica track along the projectile direction are drawn to show the height development of the nanostructure.	48
3.24	Definition of the short length l_S and long length l_L	49
3.25	Lengths of mica tracks plotted over the incidence angle, different energies correspond to different color.	50
3.26	Short lengths of muscovite mica plotted over the energy loss. The lengths are given for an incidence angle $\varphi = 1^\circ$	52
3.27	Long lengths of mica plotted over energy loss. The lengths are given for an incidence angle $\varphi = 1^\circ$	52
3.28	A 3d plot of the mica double track.	53
3.29	Comparison of mica double tracks consisting of one continuous double track and with more sections.	54
3.30	Definition of the double track properties height h , distance d in (a) and width w in (b).	56
3.31	Mica double track height h and the distance d between the tracks plotted over the irradiation angle.	56
3.32	Energy loss dependence of the double track parameters height h and distance d	57
3.33	The width w of the double tracks plotted over the incidence angle in the left and a sketch of tip artefacts in the right.	57
3.34	The groove depths between the double tracks plotted over the angle of incidence in the left and a sketch of tip artefacts in the right.	58
3.35	The maximum of the track height is plotted over the angle of incidence and the energy loss dependence of the same property is evaluated.	59
3.36	Short (left) and long lengths (right) of heated mica in comparison to irradiation under room temperature.	60
3.37	Temperature dependence of mica double track properties h , d and w . Only the three samples irradiated with 100 MeV Pb ions are shown.	61
3.38	Comparison of different types of mica grooves (irradiated under room temperature and heated to 400°C).	62
3.39	The length distribution of two targets is shown, the short length in a) and the long ones of the same targets in b).	64
3.40	For two samples the angular distribution has been performed and compared with a Gaussian curve. In a) the short lengths and in b) the long lengths are the starting point of the analysis.	64

3.41	Comparison of Gaussian fits of different targets, in a) the influence of the degrader foil at a constant angle of incidence is shown, in b) two angles of incidence with and without degrader are compared.	65
3.42	Comparison of AFM images of mica-OH and mica-F.	66
3.43	Short and long lengths of the three mica-F samples plotted over the incidence angle in comparison to mica-OH targets irradiated under the same conditions.	67
3.44	Analysis of mica-F double track properties h , d and w in the left and of the groove depth in the right.	68
3.45	3d plot of the ditch structure of a mica-F track.	70
3.46	Illustration of the irradiation process.	71

List of Tables

2.1	Kinetic energy of the incoming ions by using a degrader in front of the target as calculated using TRIM [55].	18
2.2	Overview of target densities used for the SRIM energy loss calculations.	26
2.3	SRIM calculated stopping power.	28
3.1	The relation maximal height/double track height calculated for the different ion energies.	59
3.2	Analysis of the depth of the groove (ditch) between the double tracks of mica irradiated at different target temperatures with Pb ions at 100 MeV.	63
3.3	Analysis of the maximal height of mica tracks irradiated at different target temperatures with Pb ions at 100 MeV.	63
3.4	Analysis of two ditches of mica-F.	69
A.1	Irradiation data of SrTiO ₃	77
A.2	Irradiation data of TiO ₂	77
A.3	Irradiation data of CaF ₂	77
A.4	Irradiation data of mica-OH.	78
A.5	Irradiation data of mica-F.	78

Bibliography

- [1] R. Fleischer, P. Price, and R. Walker. *Ion explosion spike mechanism for formation of charged-particle tracks in solids*. Journal of applied Physics **36**, 3645 (1965).
- [2] J. Coburn, H. F. Winters, and T. Chuang. *Ion-surface interactions in plasma etching*. Journal of Applied Physics **48**, 3532 (1977).
- [3] L. Hanley and S. B. Sinnott. *The growth and modification of materials via ion-surface processing*. Surface Science **500**, 500 (2002).
- [4] B. Gologan, J. R. Green, J. Alvarez, J. Laskin, and R. G. Cooks. *Ion/surface reactions and ion soft-landing*. Physical Chemistry Chemical Physics **7**, 1490 (2005).
- [5] S. Brezinsek, S. Wiesen, D. Harting, C. Guillemaut, A. Webster, K. Heinola, A. Meigs, M. Rack, Y. Gao, G. Sergienko *et al.* *Characterisation of the deuterium recycling at the W divertor target plates in JET during steady-state plasma conditions and ELMs*. Physica scripta **2016**, 014076 (2016).
- [6] A. Benninghoven, F. Rudenauer, and H. W. Werner. *Secondary ion mass spectrometry: basic concepts, instrumental aspects, applications and trends*. John Wiley and Sons, New York, NY (1987).
- [7] A. M. Belu, D. J. Graham, and D. G. Castner. *Time-of-flight secondary ion mass spectrometry: techniques and applications for the characterization of bio-material surfaces*. Biomaterials **24**, 3635 (2003).
- [8] Y. Gao. *A new secondary ion mass spectrometry technique for III-V semiconductor compounds using the molecular ions CsM+*. Journal of applied physics **64**, 3760 (1988).
- [9] M. Aono, C. Oshima, S. Zaima, S. Otani, and Y. Ishizawa. *Quantitative surface atomic geometry and two-dimensional surface electron distribution analysis by a new technique in low-energy ion scattering*. Japanese Journal of Applied Physics **20**, L829 (1981).

- [10] H. Niehus, W. Heiland, and E. Taglauer. *Low-energy ion scattering at surfaces*. Surface Science Reports **17**, 213 (1993).
- [11] M. Aono, Y. Hou, C. Oshima, and Y. Ishizawa. *Low-energy ion scattering from the Si (001) surface*. Physical Review Letters **49**, 567 (1982).
- [12] K. Kimura, K. Ohshima, and M.-h. Mannami. *Monolayer analysis in Rutherford backscattering spectroscopy*. Applied physics letters **64**, 2232 (1994).
- [13] F. Aumayr, S. Facsko, A. S. El-Said, C. Trautmann, and M. Schleberger. *Single ion induced surface nanostructures: a comparison between slow highly charged and swift heavy ions*. Journal of Physics: Condensed Matter **23**, 393001 (2011).
- [14] O. Ochedowski, O. Osmani, M. Schade, B. K. Bussmann, B. Ban-d'Etat, H. Lebius, and M. Schleberger. *Graphitic nanostripes in silicon carbide surfaces created by swift heavy ion irradiation*. Nature communications **5** (2014).
- [15] E. Akcöltekin, T. Peters, R. Meyer, A. Duvenbeck, M. Klusmann, I. Monnet, H. Lebius, and M. Schleberger. *Creation of multiple nanodots by single ions*. Nature Nanotechnology **2**, 290 (2007).
- [16] R. Ritter, G. Kowarik, W. Meissl, L. Süß, L. Maunoury, H. Lebius, C. Dufour, M. Toulemonde, and F. Aumayr. *Nano-structure formation due to impact of highly charged ions on HOPG*. Nuclear Instruments and Methods in Physics Research Section B: Beam Interactions with Materials and Atoms **268**, 2897 (2010).
- [17] A. El-Said, R. Heller, W. Meissl, R. Ritter, S. Facsko, C. Lemell, B. Solleder, I. C. Gebeshuber, G. Betz, M. Toulemonde *et al.* *Creation of nanohillocks on CaF₂ surfaces by single slow highly charged ions*. Physical review letters **100**, 237601 (2008).
- [18] C. Lemell, A. El-Said, W. Meissl, I. C. Gebeshuber, C. Trautmann, M. Toulemonde, J. Burgdörfer, and F. Aumayr. *On the nano-hillock formation induced by slow highly charged ions on insulator surfaces*. Solid-State Electronics **51**, 1398 (2007).
- [19] Y. Baba, K. Nagata, S. Takahashi, N. Nakamura, N. Yoshiyasu, M. Sakurai, C. Yamada, S. Ohtani, and M. Tona. *Surface modification on highly oriented pyrolytic graphite by slow highly charged ions*. Surface science **599**, 248 (2005).

- [20] F. Aumayr and H. Winter. *Slow Highly Charged Ions-A New Tool For Surface Nanostructuring?*. e-Journal of Surface Science and Nanotechnology **1**, 171 (2003).
- [21] F. Aumayr, A. El-Said, and W. Meissl. *Nano-sized surface modifications induced by the impact of slow highly charged ions-A first review*. Nuclear Instruments and Methods in Physics Research Section B: Beam Interactions with Materials and Atoms **266**, 2729 (2008).
- [22] R. Ritter, G. Kowarik, W. Meissl, A. El-Said, L. Maunoury, H. Lebius, C. Dufour, M. Toulemonde, and F. Aumayr. *Nanostructure formation due to impact of highly charged ions on mica*. Vacuum **84**, 1062 (2010).
- [23] R. Ritter, R. Wilhelm, R. Ginzl, G. Kowarik, R. Heller, A. El-Said, R. Papaléo, W. Rupp, J. C. López-Urrutia, J. Ullrich *et al.* *Pit formation on poly (methyl methacrylate) due to ablation induced by individual slow highly charged ion impact*. EPL (Europhysics Letters) **97**, 13001 (2012).
- [24] R. Ritter, R. A. Wilhelm, M. Stöger-Pollach, R. Heller, A. Mücklich, U. Werner, H. Vieker, A. Beyer, S. Facsko, A. Gözlhäuser *et al.* *Fabrication of nanopores in 1 nm thick carbon nanomembranes with slow highly charged ions*. Applied Physics Letters **102**, 063112 (2013).
- [25] E. Goldstein. *Über eine noch nicht untersuchte Strahlungsform an der Kathode induzierter Entladungen*. Sitzungsberichte der königlichen Akademie der Wissenschaften zu Berlin p. 691 (1886).
- [26] W. Wien. *Handbuch der Experimentalphysik*, vol. 14. Springer (1927).
- [27] C. Wilson. *Cloud-chamber technique*. In *Proc. Roy Soc*, vol. 85, p. 285 (1911).
- [28] C. T. R. Wilson. *On an expansion apparatus for making visible the tracks of ionising particles in gases and some results obtained by its use*. Proceedings of the Royal Society of London. Series A, Containing Papers of a Mathematical and Physical Character **87**, 277 (1912).
- [29] D. Young. *Etching of radiation damage in lithium fluoride*. Nature **182** (1958).
- [30] E. Silk and R. Barnes. *Examination of fission fragment tracks with an electron microscope*. Philosophical Magazine **4**, 970 (1959).

- [31] F. Aumayr and H. Winter. *Potential sputtering*. Philosophical Transactions of the Royal Society of London A: Mathematical, Physical and Engineering Sciences **362**, 77 (2004).
- [32] N. Bohr. *Velocity-range relation for fission fragments*. Physical Review **59**, 270 (1941).
- [33] Y. N. Yavlinskii. *Coulomb repulsion of lattice ions under swift heavy ion irradiation*. Nuclear Instruments and Methods in Physics Research Section B: Beam Interactions with Materials and Atoms **245**, 114 (2006).
- [34] M. Toulemonde, C. Dufour, A. Meftah, and E. Paumier. *Transient thermal processes in heavy ion irradiation of crystalline inorganic insulators*. Nuclear Instruments and Methods in Physics Research Section B: Beam Interactions with Materials and Atoms **166**, 903 (2000).
- [35] W. Bolse, B. Schattat, and A. Feyh. *Modification of thin-layer systems by swift heavy ions*. Applied Physics A **77**, 11 (2003).
- [36] G. Schiwietz, K. Czerski, M. Roth, F. Staufenbiel, and P. Grande. *Femtosecond dynamics—snapshots of the early ion-track evolution*. Nuclear Instruments and Methods in Physics Research Section B: Beam Interactions with Materials and Atoms **225**, 4 (2004).
- [37] S. Klaumünzer, M.-d. Hou, and G. Schumacher. *Coulomb explosions in a metallic glass due to the passage of fast heavy ions?* Physical review letters **57**, 850 (1986).
- [38] C. Dufour, A. Audouard, F. Beuneu, J. Dural, J. Girard, A. Hairie, M. Levalois, E. Paumier, and M. Toulemonde. *A high-resistivity phase induced by swift heavy-ion irradiation of Bi: a probe for thermal spike damage?* Journal of Physics: Condensed Matter **5**, 4573 (1993).
- [39] Z. Wang, C. Dufour, E. Paumier, and M. Toulemonde. *The Se sensitivity of metals under swift-heavy-ion irradiation: a transient thermal process*. Journal of Physics: Condensed Matter **6**, 6733 (1994).
- [40] H. Mieskes, W. Assmann, F. Grüner, H. Kucal, Z. Wang, and M. Toulemonde. *Electronic and nuclear thermal spike effects in sputtering of metals with energetic heavy ions*. Physical Review B **67**, 155414 (2003).

- [41] M. Waligorski, R. Hamm, and R. Katz. *The radial distribution of dose around the path of a heavy ion in liquid water*. International Journal of Radiation Applications and Instrumentation. Part D. Nuclear Tracks and Radiation Measurements **11**, 309 (1986).
- [42] M. Toulemonde, J. Costantini, C. Dufour, A. Meftah, E. Paumier, and F. Studer. *Track creation in SiO_2 and $\text{BaFe}_{12}\text{O}_{19}$ by swift heavy ions: a thermal spike description*. Nuclear Instruments and Methods in Physics Research Section B: Beam Interactions with Materials and Atoms **116**, 37 (1996).
- [43] A. Meftah, F. Brisard, J. Costantini, E. Dooryhee, M. Hage-Ali, M. Hervieu, J. Stoquert, F. Studer, and M. Toulemonde. *Track formation in SiO_2 quartz and the thermal-spike mechanism*. Physical Review B **49**, 12457 (1994).
- [44] C. Trautmann, M. Toulemonde, K. Schwartz, J. Costantini, and A. Müller. *Damage structure in the ionic crystal LiF irradiated with swift heavy ions*. Nuclear Instruments and Methods in Physics Research Section B: Beam Interactions with Materials and Atoms **164**, 365 (2000).
- [45] M. Toulemonde, C. Dufour, and E. Paumier. *The ion-matter interaction with swift heavy ions in the light of inelastic thermal spike model*. ACTA PHYSICA POLONICA SERIES A **109**, 311 (2006).
- [46] M. Karlusić, S. Akcöltekin, O. Osmani, I. Monnet, H. Lebius, M. Jaksić, and M. Schleberger. *Energy threshold for the creation of nanodots on SrTiO_3 by swift heavy ions*. New Journal of Physics **12**, 043009 (2010).
- [47] W. Demtröder. *Experimentalphysik 4*. Springer-Verlag Berlin Heidelberg (2010).
- [48] J. F. Ziegler, J. P. Biersack, and M. D. Ziegler. *SRIM, the stopping and range of ions in matter* (2008).
- [49] W. Demtröder. *Experimentalphysik 3*. Springer-Verlag Berlin Heidelberg (2010).
- [50] O. Firsov. *Calculation of atomic interaction potentials*. Zh. Eksp. Teor. Fiz **33**, 696 (1957).
- [51] F. Bloch. *Zur bremsung rasch bewegter teilchen beim durchgang durch materie*. Annalen der Physik **408**, 285 (1933).

- [52] B. Weaver and A. Westphal. *Energy loss of relativistic heavy ions in matter*. Nuclear Instruments and Methods in Physics Research Section B: Beam Interactions with Materials and Atoms **187**, 285 (2002).
- [53] H. Andersen, H. Sørensen, and P. Vadja. *Excitation Potentials and Shell Corrections for the Elements $Z_2=20$ to $Z_2=30$* . Physical Review **180**, 373 (1969).
- [54] J. R. Sabin and J. Oddershede. *Shell corrections to electronic stopping powers from orbital mean excitation energies*. Physical Review A **26**, 3209 (1982).
- [55] Z. J. F. *SRIM*. www.SRIM.org. Accessed: 2015-11-07.
- [56] V. Altapova, O. V. Bogdanov, and Y. L. Pivovarov. *Cherenkov radiation from relativistic heavy ions taking account of their slowing down in radiator*. Nuclear Instruments and Methods in Physics Research Section B: Beam Interactions with Materials and Atoms **267**, 896 (2009).
- [57] J. D. Jackson. *Klassische Elektrodynamik*. Walter de Gruyter (2006).
- [58] S. Datz, H. Krause, and C. Vane. *Crystal assisted processes in ion channeling*. Nuclear Instruments and Methods in Physics Research Section B: Beam Interactions with Materials and Atoms **115**, 363 (1996).
- [59] S. Datz, C. Vane, P. Dittner, J. Giese, J. G. Del Campo, N. Jones, H. Krause, P. Miller, M. Schulz, H. Schöne *et al.* *Resonant dielectronic and direct excitation in crystal channels*. Physical review letters **63**, 742 (1989).
- [60] G. Piercy, F. Brown, J. Davies, and M. McCargo. *Experimental evidence for the increase of heavy ion ranges by channeling in crystalline structure*. Physical Review Letters **10**, 399 (1963).
- [61] N. Bohr. *The penetration of atomic particles through matter*, vol. 18. I kommission hos E. Munksgaard (1948).
- [62] H.-D. Betz. *Charge states and charge-changing cross sections of fast heavy ions penetrating through gaseous and solid media*. Reviews of Modern Physics **44**, 465 (1972).
- [63] S. Akcöltekin, E. Akcöltekin, T. Roll, H. Lebius, and M. Schleberger. *Patterning of insulating surfaces by electronic excitation*. Nuclear Instruments and Methods in Physics Research Section B: Beam Interactions with Materials and Atoms **267**, 1386 (2009).

- [64] S. Akcöltekin, E. Akcöltekin, M. Schleberger, and H. Lebius. *Scanning probe microscopy investigation of nanostructured surfaces induced by swift heavy ions*. Journal of Vacuum Science & Technology B **27**, 944 (2009).
- [65] E. Akcöltekin, S. Akcöltekin, O. Osmani, A. Duvenbeck, H. Lebius, and M. Schleberger. *Swift heavy ion irradiation of SrTiO₃ under grazing incidence*. New Journal of Physics **10**, 053007 (2008).
- [66] S. Akcöltekin, H. Bukowska, T. Peters, O. Osmani, I. Monnet, I. Alzaher, B. B. d'Etat, H. Lebius, and M. Schleberger. *Unzipping and folding of graphene by swift heavy ions*. Applied Physics Letters **98**, 103103 (2011).
- [67] M. Tona, Y. Fujita, C. Yamada, and S. Ohtani. *Electronic interaction of individual slow highly charged ions with TiO₂ (110)*. Physical Review B **77**, 155427 (2008).
- [68] V. Popok, J. Jensen, S. Vučković, A. Mackova, and C. Trautmann. *Formation of surface nanostructures on rutile (TiO₂): comparative study of low-energy cluster ion and high-energy monoatomic ion impact*. Journal of Physics D: Applied Physics **42**, 205303 (2009).
- [69] K. Awazu, X. Wang, M. Fujimaki, T. Komatsubara, T. Ikeda, and Y. Ohki. *Structure of latent tracks in rutile single crystal of titanium dioxide induced by swift heavy ions*. Journal of applied physics **100**, 044308 (2006).
- [70] M. Thakurdesai, I. Sulania, A. Narsale, D. Kanjilal, and V. Bhattacharyya. *Formation of TiO₂ Nanorings Due to Rapid Thermal Annealing of Swift Heavy Ion Irradiated Films*. Journal of nanoscience and nanotechnology **8**, 4387 (2008).
- [71] M. Thakurdesai, T. Mohanty, D. Kanjilal, P. Raychaudhuri, and V. Bhattacharyya. *Formation of nanocrystalline TiO₂ by 100MeV Au⁸⁺*. Applied Surface Science **255**, 8935 (2009).
- [72] H. Rath, P. Dash, T. Som, P. Satyam, U. Singh, P. Kulriya, D. Kanjilal, D. Avasthi, and N. Mishra. *Structural evolution of TiO₂ nanocrystalline thin films by thermal annealing and swift heavy ion irradiation*. Journal of Applied Physics **105**, 74311 (2009).
- [73] C. Müller, M. Cranney, A. El-Said, N. Ishikawa, A. Iwase, M. Lang, and R. Neumann. *Ion tracks on LiF and CaF₂ single crystals characterized by scanning force microscopy*. Nuclear Instruments and Methods in Physics Research Section B: Beam Interactions with Materials and Atoms **191**, 246 (2002).

- [74] N. Khalfaoui, C. Rotaru, S. Bouffard, M. Toulemonde, J. Stoquert, F. Haas, C. Trautmann, J. Jensen, and A. Dunlop. *Characterization of swift heavy ion tracks in CaF₂ by scanning force and transmission electron microscopy*. Nuclear Instruments and Methods in Physics Research Section B: Beam Interactions with Materials and Atoms **240**, 819 (2005).
- [75] N. Khalfaoui, M. Görlich, C. Müller, M. Schleberger, and H. Lebius. *Latent tracks in CaF₂ studied with atomic force microscopy in air and in vacuum*. Nuclear Instruments and Methods in Physics Research Section B: Beam Interactions with Materials and Atoms **245**, 246 (2006).
- [76] Y. Wang, C. Grygiel, C. Dufour, J. Sun, Z. Wang, Y. Zhao, G. Xiao, R. Cheng, X. Zhou, J. Ren *et al.* *Energy deposition by heavy ions: Additivity of kinetic and potential energy contributions in hillock formation on CaF₂*. Scientific reports **4** (2014).
- [77] T. Roll, M. Meier, S. Akcöltekin, M. Klusmann, H. Lebius, and M. Schleberger. *Conductive nanodots on the surface of irradiated CaF₂*. physica status solidi (RRL)-Rapid Research Letters **2**, 209 (2008).
- [78] J. Jensen, A. Dunlop, S. Della-Negra, and M. Toulemonde. *A comparison between tracks created by high energy mono-atomic and cluster ions in Y₃Fe₅O₁₂*. Nuclear Instruments and Methods in Physics Research Section B: Beam Interactions with Materials and Atoms **146**, 412 (1998).
- [79] C. Trautmann, M. Boccanfuso, A. Benyagoub, S. Klaumünzer, K. Schwartz, and M. Toulemonde. *Swelling of insulators induced by swift heavy ions*. Nuclear Instruments and Methods in Physics Research Section B: Beam Interactions with Materials and Atoms **191**, 144 (2002).
- [80] M. Boccanfuso, A. Benyagoub, K. Schwartz, C. Trautmann, and M. Toulemonde. *Study of the damage produced in CaF₂ by swift heavy ion irradiation*. Nuclear Instruments and Methods in Physics Research Section B: Beam Interactions with Materials and Atoms **191**, 301 (2002).
- [81] F. Thibaudau, J. Cousty, E. Balanzat, and S. Bouffard. *Atomic-force-microscopy observations of tracks induced by swift Kr ions in mica*. Physical review letters **67**, 1582 (1991).
- [82] D. B. Daya, A. Hallén, P. Håkansson, B. Sundqvist, and C. Reimann. *Scanning force microscopy study of surface tracks induced in mica by 78.2-MeV ¹²⁷I*

- ions*. Nuclear Instruments and Methods in Physics Research Section B: Beam Interactions with Materials and Atoms **103**, 454 (1995).
- [83] J. Ackermann, N. Angert, R. Neumann, C. Trautmann, M. Dischner, T. Hagen, and M. Sedlacek. *Ion track diameters in mica studied with scanning force microscopy*. Nuclear Instruments and Methods in Physics Research Section B: Beam Interactions with Materials and Atoms **107**, 181 (1996).
- [84] J. Ackermann, A. Müller, R. Neumann, and Y. Wang. *Scanning force microscopy on heavy-ion tracks in muscovite mica: track diameter versus energy loss and loading force*. Applied Physics A: Materials Science & Processing **66**, 1151 (1998).
- [85] M. Lang, U. Glasmacher, B. Moine, R. Neumann, and G. Wagner. *Etch-pit morphology of tracks caused by swift heavy ions in natural dark mica*. Nuclear Instruments and Methods in Physics Research Section B: Beam Interactions with Materials and Atoms **218**, 466 (2004).
- [86] D. B. Daya, C. Reimann, P. Håkansson, B. Sundqvist, A. Brunelle, S. Della-Nagra, and Y. Le Beyec. *Crater formation due to grazing incidence C_{60} cluster ion impacts on mica: a tapping-mode scanning force microscopy study*. Nuclear Instruments and Methods in Physics Research Section B: Beam Interactions with Materials and Atoms **124**, 484 (1997).
- [87] D. B. Daya, C. Reimann, A. Hallén, B. Sundqvist, and P. Håkansson. *Latent (sub-surface) tracks in mica studied by tapping mode scanning force microscopy*. Nuclear Instruments and Methods in Physics Research Section B: Beam Interactions with Materials and Atoms **111**, 87 (1996).
- [88] L. Bergen. *Atomic force microscope imaging of ion induced nanostructures on mica surfaces*. Projektarbeit, TU Wien (2015).
- [89] G. Binnig, C. F. Quate, and C. Gerber. *Atomic force microscope*. Physical review letters **56**, 930 (1986).
- [90] *Avogadro: an open-source molecular builder and visualization tool. Version 2.0*. <http://avogadro.openmolecules.net/>. Accessed: 2015-11-10.
- [91] M. D. Hanwell, D. E. Curtis, D. C. Lonie, T. Vandermeersch, E. Zurek, and G. R. Hutchison. *Avogadro: An advanced semantic chemical editor, visualization, and analysis platform*. J. Cheminformatics **4**, 17 (2012).

- [92] *Gwyddion-Free S 2000 Data analysis software*. www.gwyddion.net.
- [93] I. Horcas, R. Fernández, J. Gomez-Rodriguez, J. Colchero, J. Gómez-Herrero, and A. Baro. *WSXM: a software for scanning probe microscopy and a tool for nanotechnology*. Review of Scientific Instruments **78**, 013705 (2007).
- [94] S. Akcöltekin, T. Roll, E. Akcöltekin, M. Klusmann, H. Lebius, and M. Schleberger. *Enhanced susceptibility of CaF_2 (111) to adsorption due to ion irradiation*. Nuclear Instruments and Methods in Physics Research Section B: Beam Interactions with Materials and Atoms **267**, 683 (2009).
- [95] K. Miura, T. Yamada, M. Ishikawa, and S. Okita. *Apparent contrast of molecularly thin films of water at ionic crystal surfaces*. Applied surface science **140**, 415 (1999).
- [96] T. Morimoto, T. Kadota, and Y. Kuroda. *Adsorption of water on CaF_2 : Two-dimensional condensation of water*. Journal of colloid and interface science **106**, 104 (1985).
- [97] L. Pauling. *The structure of the micas and related minerals*. Proceedings of the National Academy of Sciences **16**, 123 (1930).
- [98] J. F. Ziegler, M. D. Ziegler, and J. P. Biersack. *SRIM—The stopping and range of ions in matter (2010)*. Nuclear Instruments and Methods in Physics Research Section B: Beam Interactions with Materials and Atoms **268**, 1818 (2010).
- [99] E. Gruber. PhD-Thesis, TU Wien, unpublished .
- [100] gnuplot - An Interactive Plotting Program (Version 4.2 - Documentation) http://gnuplot.sourceforge.net/docs_4.2/node82.html, accessed 2015-05-11.
- [101] F. Meinerzhagen, L. Breuer, H. Bukowska, M. Bender, D. Severin, M. Herder, H. Lebius, M. Schleberger, and A. Wucher. *A new setup for the investigation of swift heavy ion induced particle emission and surface modifications*. Review of Scientific Instruments **87**, 013903 (2016).
- [102] L. A. Pérez-Maqueda, J. M. Blanes, J. Pascual, and J. L. Pérez-Rodríguez. *The influence of sonication on the thermal behavior of muscovite and biotite*. Journal of the European Ceramic Society **24**, 2793 (2004).
- [103] Kraft, Bürger, Unfried, and Götz. *Mathematische Formelsammlung*. ÖBV (2007).

-
- [104] J. E. Huheey, E. A. Keiter, and R. L. Keiter. *Anorganische Chemie*, vol. 4. DE GRUYTER (2012).

Danksagung

Zum Abschluss meiner Diplomarbeit möchte ich mich bei allen bedanken, ohne deren Unterstützung ich dieses Projekt nie zu Ende gebracht hätte.

Allen voran gilt mein großer Dank meinem Betreuer Prof. Friedrich Aumayr, dass ich meine Diplomarbeit in seiner Atom- und Plasmaphysikgruppe schreiben durfte. Was deine Herangehensweise an das Lösen physikalischer Problemstellungen betrifft, bist du immer ein Vorbild für mich. Trotz deiner neuen Aufgaben als Institutsvorstand hast du deine Gruppe nicht aus den Augen verloren und nimmst dir immer die Zeit, um dich um unsere Anliegen zu kümmern. Mit dem Konferenzaufenthalt in Darmstadt hast du mir einen Einblick in eine für mich neue Welt geboten und ich werde die Erfahrungen, die ich dabei machen durfte, nie vergessen.

Ein großes Dankeschön geht auch an meine Betreuerin Elisabeth Gruber. Ich wurde von dir mit großer Geduld betreut und konnte viel von deiner Arbeitsweise und deinem Wissen lernen. Leider wurde mir erst in den letzten Wochen, als ich selbst zwei Bachelorarbeiten betreute, wirklich klar, wie viel Zeit ich dir in den ersten Wochen gekostet habe. Umso mehr schätze ich, dass ich immer mit meinen Problemen während der Messungen am AFM zu dir kommen konnte und du mir stets mit Rat und Tat zur Seite gestanden bist. Danke für die schöne Zeit, ich bin wirklich froh, dass du meine Diplomarbeitsbetreuerin warst.

YuYu, danke für die Ratschläge die du mir für die Messungen am AFM gegeben hast. Durch deine offene Art hast du unseren gemeinsamen Konferenzbesuch unvergesslich gemacht. (PS: Ich weiß, du kannst das lesen.)

Danke auch an alle anderen Kollegen und Kolleginnen aus meiner Arbeitsgruppe. Zu einigen möchte ich noch kurz etwas Persönliches schreiben.

Janine, du warst über die letzten Monate meine Leidensgenossin. Es hat mir immer wieder neue Motivation gegeben, zu sehen, dass ich nicht der einzige bin, der sich gerade so beim Schreiben der Diplomarbeit quält. Du warst mir die ganze Zeit über eine große Unterstützung und ein Vorbild wie man sich durch den großen Stress durchbeißen kann.

Paul, dir möchte ich danken, dass du immer wieder aufs Neue versucht hast mich zum Schreiben dieser Arbeit zu motivieren und immer ein offenes Ohr für mich hattest, wenn ich nach stundenlanger Isolation im AFM Kammerl jemanden zum

Tratschen brauchte.

Auch bei Valerie bedanke ich mich für die vielen Gespräche, die wir vor allem in der Anfangszeit meiner Diplomarbeit geführt haben, als ich neu in die Gruppe gekommen bin, sowie für die Hilfe während der Laborübungen.

All meinen anderen Bürokollegen (Christian, Dominic, Laurids und Sebastian) danke ich für die schöne Zeit und unsere vielen gemeinsamen Kaffeepausen. Bernhard und Reinhard möchte ich für die Unterstützung während meiner Arbeiten im Augustin-Labor danken, Florian für seine (vor allem designmäßigen) Verbesserungsvorschläge meiner Projektarbeit.

In den letzten Monaten durfte ich zwei Bachelorarbeiten betreuen, jene von Jacqueline Keintzel und Daniel Mayer. Ich danke euch beiden für die angenehme Zusammenarbeit und hoffe, dass ich euch ein guter Betreuer war und ihr die Zeit in der Arbeitsgruppe in positiver Erinnerung behalten werdet. So möchte ich euch noch viel Erfolg bei der Fertigstellung eurer Arbeiten wünschen.

Zu guter Letzt möchte ich mich bei meiner Familie, insbesondere bei meinen Eltern und meiner Schwester für die Unterstützung in den letzten Jahren bedanken. Ihr habt mir dieses Studium erst ermöglicht und seid immer hinter all meinen Entscheidungen gestanden. Ohne euch hätte ich es nicht bis hierher geschafft.

DANKE